T 172

50604

DENSITY FUNCTIONAL STUDIES ON STRUCTURAL AND ELECTRONIC PROPERTIES OF BARE AND SUPPORTED GOLD NANOCLUSTERS

A THESIS SUBMITTED IN PARTIAL FULFILLMENT OF
THE REQUIREMENTS FOR THE DEGREE OF

DOCTOR OF PHILOSOPHY

By

Ajanta Deka

Registration No: 029 of 2009

Department of Physics
School of Science and Technology
Tezpur University
Napaam, Tezpur-784 028
Assam, INDIA

January 2011

Dedicated to

My Parents,

My Husband

&

Little Mayukh

DECLARATION

I hereby declare that the thesis entitled "*Density Functional Studies on Structural and Electronic Properties of Bare and Supported Gold Nanoclusters*" being submitted to the Department of Physics, Tezpur University, is a record of original research work carried out by me. Any text, figures, results or designs that are not of own devising are appropriately referenced in order to give credit to the original author(s). All sources of assistance have been assigned due acknowledgement. I also declare that neither this work as a whole nor a part of it has been submitted to any other university or institute for any other degree, diploma or award.

Date: 18·01. 2011

Place: Tezpur

(*Ajanta Deka*)

तेजपुर विश्वविद्यालय
(केंद्रीय विश्वविद्यालय)

नपाम, तेजपुर – 784 028, असम, भारत

TEZPUR UNIVERSITY
(A Central University)

Napaam, Tezpur - 784 028, Assam, India

Certificate

This is to certify that the thesis entitled ***Density Functional Studies on Structural and Electronic Properties of Bare and Supported Gold Nanoclusters*** submitted to the School of Science and Technology, Tezpur University in part fulfillment for the award of the degree of Doctor of Philosophy in Physics is a record of research work carried out by Ms Ajanta Deka under my supervision and guidance. Chapter 3 of the thesis titled "Density Functional Studies on Gas Phase Nanoclusters of Gold" was done under the guidance of Dr. Ashwini K. Phukan, Department of Chemical Sciences, Tezpur University. Further, chapter 7 titled "TDDFT Optical Absorption Spectra of Coinage Metal Dimers Suppported on $MgO(001)$" involves work done by Ms. Deka under the guidance of Prof. Notker Rösch, Director, Catalysis Research Center, Technische Universität München, Germany during her visit to his research group from May to November, 2007. She has been duly registered and the thesis presented is worthy of being considered for the Ph. D. degree. All help received by her from various sources have been duly acknowledged. No part of this thesis has been submitted elsewhere for award of any other degree.

Date: 18.1.11

Place: TEZPUR UNIVERSITY

(Prof.A.Choudhury)

Department of Physics

Tezpur University

Acknowledgements

As I start expressing my gratitude to the all the people who have helped me directly or indirectly in accomplishing my Ph.D. work, I feel nostalgic. It has been a long journey of about five and a half years, from August, 2005 to December, 2010. During this period I received help and support from several people. I take this opportunity to thank all of them.

At the outset, I would like to thank my research supervisor Prof. Amarjyoti Choudhury for his able guidance and support and for offering a helping hand at the juncture when it was much needed. He has always been open to discussions and has constantly encouraged me in my work. I shall remain ever indebted to him.

I am also grateful to Prof. Notker Rösch, Director of Catalysis Research Center, Technical University of Munich (TUM), Germany for initiating me into research in the field of computational material science. I thank him for allowing me to work in his research group in two stints, September, 2003 to October, 2004 and again from May to November, 2007. I have learnt a lot from regular discussions and the classes that he conducted. My stay at TUM has helped me to learn invaluable lessons on professionalism.

I would like to express my sincere gratitude to Prof. Mihir Kanti Chaudhuri, Vice-Chancellor, Tezpur University for his help, support and encouragement.

Thanks are also due to Dr. Ashwini K. Phukan, Department of Chemical Sciences for allowing me to work in his group in the initial period of my research. I would also like to thank all the faculty members and staff of the departments of Physics and Chemical Sciences for helping me at different stages of my work.

My labmates Pubalee, Paritosh, Kalyan, Kusum, Nabanita and Subhi at Tezpur University and Lyudmila, Miquel, Alexei, Sergei, Lim and Sun at TUM deserve special mention. I would also like to thank other research scholars and friends from the departments of Physics and Chemical Sciences for making my stay here at Tezpur University a pleasant one and for providing a lively atmosphere for research. I am also thankful to the persons manning the Computer Centre at Tezpur University for urgently attending to all computer related problems which enabled me to carry out my calculations without any hassle.

I am also indebted to the authority of GIMT, the institute where I work, for allowing me to come to Tezpur for my research work wherever necessary, in the course of the last two and a half years. I owe my gratitude to my colleagues at GIMT, who have been very encouraging and supportive regarding my research work. I gratefully acknowledge the funding that I received from North Eastern Council during the first year of my Ph.D. research and subsequently from Tezpur University.

It is a pleasure to thank Dr. Suvendu Kumar Ray, Department of MBBT, Tezpur University and Mama, his wife and my dear friend for constant encouragement and support and for allowing me to give vent to my frustrations during the course of my Ph.D. journey. I would also like to thank my friend Madhumita for being by my side whenever I needed ever since my college days.

The journey of life cannot be complete without the family. I am extremely lucky to have very supportive parents who are ready to walk many extra miles to see me shine in life. It was only for them that I could visit TUM, Germany for six months in 2007 inspite of having a minor son, all of one year and five months. They took all the pains to look after our son Mayukh while I was working in far off Germany. I thank my parents from the deepest core of my heart. I am grateful to my brother Hemanta for constant encouragement. I also thank my parents-in-law for their support and blessings. Our little son Mayukh has been extremely understanding of his age. In fact, it is he who sometimes propels me to work till late in the night when I am tired. Without his understanding and patience, it would not have been possible for me to complete my thesis work. I feel very happy and proud to be his mother.

At this juncture I cannot find words enough to express my love and gratitude to my dear husband Ramesh for being my strongest pillar ever since I got married to him. But for him, I would not have been in the field of research today. It was from his work that I got motivated to take up academics and research as a career. I thank him for making himself available for unending discussions both academic and otherwise, inspite of his busy schedule and for being ever patient and understanding.

Department of Physics,

Tezpur University

Date: 18.01.2011

Ajanta Deka

DENSITY FUNCTIONAL STUDIES ON STRUCTURAL AND ELECTRONIC PROPERTIES OF BARE AND SUPPORTED GOLD NANOCLUSTERS

ABSTRACT

The goal of the present thesis is to investigate the structure, stability and reactivity of small gold nanoclusters both in the gas phase and on metal oxide supports by using density functional methods. The structure and stability of several isomeric cationic, neutral and anionic Au_n (n = 2-13) clusters have been determined by performing calculations based on all electron scalar relativistic density functional theory (DFT). The reactivity at different sites within these clusters has been studied by using DFT based local reactivity descriptors. These studies enable us to predict the response of various sites within the cluster towards impending nucleophilic and electrophilic attacks. These predictions for the highly stable triangular Au_6 cluster in cationic, neutral and anionic forms, have been verified by using CO as a probe molecule. We have also explored O_2 adsorption and co-adsorption of CO and O_2 on these clusters which serve as a first step towards CO oxidation. CO adsorption has also been studied on the gold monomer in various oxidation states in the gas phase and on a metal oxide support, namely, faujasite zeolite. This investigation enables us to examine the roles of the support and oxidation state of gold on CO adsorption. The process of reverse hydrogen spillover from bridging OH groups of the faujasite zeolite to gold monomer and Au_6 cluster has been studied. In addition, we demonstrate the applicability of a Natural Transition Orbital (NTO)-Fragment Molecular Orbital (FMO) method to analyze optical spectra of interacting systems by performing time-dependent density functional theory (TDDFT) calculations on coinage metal dimers M_2 (M = Cu, Ag, Au) adsorbed at regular sites as well as neutral and charged oxygen vacancies of the MgO(001) surface. The contents of the thesis have been organized as follows.

Chapter 1 gives a brief introduction to metal clusters. The chapter emphasizes the fact that their properties are significantly different from bulk materials as well as single atoms. It describes important properties of metal clusters like very high surface-to-volume ratio, shell structure, size sensitivity etc. along with some applications related to such properties. Next we dwell on transition metal clusters including coinage metals. We discuss the significance of unfilled d shells which opens up the possibility of tuning their electronic structure and hence their properties. An overview of experimental methods for production of metal nanoclusters is also provided. We also present a brief discussion on properties of gold nanoclusters. Thus special properties like aurophilicity and very strong relativistic effects which bestow them an identity different from other coinage metals are highlighted. The presence of several oxidation states in gold nanoclusters is also discussed. We present applications of gold nanoclusters in various fields including the burgeoning area of heterogeneous catalysis. This introductory chapter also includes a brief account of theoretical studies on gas phase and supported gold nanoclusters. Finally we present the objectives of the present investigation.

Chapter 2 highlights the growing importance of theoretical methods in material science and gives a brief account of electronic structure methods including density functional theory (DFT). The fundamentals of DFT are discussed. We describe different kinds of basis sets and exchange correlation functionals used in DFT. We also discuss the hybrid Quantum Mechanics (QM)/Molecular Mechanics (MM) method used for the treatment of large systems. In addition, the basic formalism of TDDFT used for describing electronic excitations, is presented.

Chapter 3 describes all electron scalar relativistic calculations that have been performed to investigate the electronic structures of neutral gold clusters (Au_n, n = 2–13) in the gas phase using density functional theory with the generalized gradient approximation. Full unconstrained geometry optimizations of topologically different clusters and clusters belonging to different symmetry groups have been carried out by using the program $DMol^3$. We have used the double numerical basis set with polarization (DNP) in combination with the exchange-correlation functional BLYP for our calculations. Binding energies, ionization potentials, electron affinities and

chemical hardness values are calculated and they are found to be comparable with the available experimental and theoretical results. The most stable structure of each cluster has a two dimensional planar configuration. A three dimensional distorted Y shaped structure for Au_4, a tri-capped triangle, a chair, and a see-saw structure for Au_6, an eclipsed sandwich structure for Au_7, a condensed trigonal bipyramid and a boat shaped structure for Au_9, a staggered sandwich and an eclipsed sandwich structure for Au_{11}, a ladderane structure for Au_{12}, and a staggered and a distorted sandwich structure for Au_{13} have been characterized for the first time in this work. The study is further extended to include several isomers of singly charged cationic and anionic clusters in the same size range. Their structural and electronic properties are investigated.

In **Chapter 4**, reactivity studies elucidating the response of various sites of the minimum energy cationic, neutral and anionic $Au_n(n = 2\text{-}13)$ clusters towards impending electrophilic and nucleophilic attacks has been determined using DFT based local reactivity descriptors, namely, Fukui function for nucleophilic attack f^+, Fukui function for electrophilic attack f^-, relative nucleophilicity f^-/f^+ and relative electrophilicity f^+/f^-. Based on these parameters different types of unique atoms have been identified for each cluster. In addition, reactivity parameters at different sites of the isomers of Au_6 cluster in neutral, cationic and anionic states have been determined. From the relative reactivity indices it is predicted that in case of the minimum energy triangular Au_6 cluster, the apex atom is prone to attack by a nucleophile like CO, while an electrophile like O_2 prefers the mid site.

Chapter 5 reports the interaction of adsorbates with gas phase gold nanoclusters and faujasite (FAU) zeolite supported gold monomers. The adsorption of the nucleophilic molecule CO and the electrophilic molecule O_2 on the neutral, cationic and anionic triangular Au_6 cluster has been investigated in order to verify predictions regarding the reactivity of various sites of these clusters obtained from DFT based reactivity descriptors. Adsorption of CO has been studied in the "on-top" mode at two sites, namely, the vertex of the outer triangle, which we designate as the apex site, and the vertex of the inner triangle, which we designate as the mid site. It is

observed that irrespective of the charge state of the cluster, adsorption of CO is stronger at the apex site. Adsorption of O_2 has been investigated at three sites, the apex site, the mid site and a bridge site in between the apex and the mid sites. It is found that O_2 prefers the mid site for adsorption. CO adsorbs more strongly on the cationic cluster compared to the neutral and anionic clusters. The co-adsorption of CO and O_2 on these clusters has also been studied with one of the reactants at the apex site and the other at the mid or bridge site. For the most stable co-adsorption complex, CO adsorbs at the apex site and O_2 at the bridge site in agreement with Fukui function values.

In order to understand the influence of a metal oxide support on the adsorption properties of CO, at first we investigate the gas phase adsorption of CO on the gold monomer in three oxidation states, 0, +1 and +3. Then the calculations are repeated with the gold atom anchored to an acidic form of faujasite zeolite. The support is represented by a 9T (T = tetrahedral unit of zeolite) cluster containing the six-member ring and three other Si atoms of the wall of the supercage of faujasite structure. For a more realistic representation of the support, we extend our study to an embedded cluster method where the zeolite support is modelled by a 60T cluster. The calculations have been performed by using the two layered ONIOM (Our-own-N-layered Integrated molecular Orbital + molecular Mechanics) method, as implemented in the program package *Gaussian 03*. An analysis of our results reveal that increasing the size of the support leads to a significant improvement in the CO adsorption energy in case of Au^+ (1.34 eV compared to 1.15 eV for the 9T cluster).

Chapter 6 discusses the phenomenon of reverse hydrogen spillover of acidic protons from H-FAU zeolite to Au^0, Au^+ and Au_6 clusters. Structure and energetics of these supported clusters have also been studied. The zeolite support has been modelled by the same 9T cluster mentioned above. The results of our study reveal that the binding of the gold monomer to the zeolite support is stronger in the oxidation state +1 than in the oxidation state 0. In the gas phase Au_6 minimizes to a triangular structure while on zeolite support it has a three dimensional structure with three apical centers bending towards the support. In all cases, except for Au^+H/H-FAU cluster, the hydrogenated clusters Au_nH/2H-FAU, Au_nH_2/H-FAU and Au_nH_3/FAU generated by stepwise reverse hydrogen spillover from bridging OH

groups of zeolite are energetically preferred over the $Au_n/3H$-FAU structures. Reverse hydrogen spillover of all the three acidic protons from the zeolite to the Au monomer is not energetically favourable.

Chapter 7 illustrates the advantages of a strategy for interpreting optical spectra of interacting systems on the basis of linear-response time-dependent density functional theory (TDDFT) calculations. We apply it to assign and characterize optical transitions of coinage metal dimers M_2 (M = Cu, Ag, Au) adsorbed at ideal oxygen sites of MgO(001) as well as at oxygen vacancies, F_s and F_s^+. The method is based on a combined natural transition orbitals (NTO) and fragment molecular orbital (FMO) analysis. The TDDFT calculations have been carried out at the generalized-gradient level on structures that had been obtained with cluster models embedded in an elastic polarizable environment. The combined NTO and FMO results allow us to analyze the spectra both qualitatively and quantitatively.

Chapter 8 summarizes the salient features emerging out of the present thesis and enunciates scope of future development in this direction.

In **Appendix A**, structures of minimum energy cationic and anionic gold clusters along with their Fukui functions are presented.

TABLE OF CONTENTS

Chapter 2: Background of Electronic Structure Methods

Chapter 3: Density Functional Studies on Gas Phase Nanoclusters of Gold

Chapter 4: Reactivity of Gold Nanoclusters from Conceptual

Density Functional Studies

Chapter 5: Adsorption of CO and O_2 on Gas Phase and Zeolite

Supported Gold Clusters

Chapter 6: Energetics of Reverse Hydrogen Spillover from Zeolite Support to Gold Clusters

Chapter 7: TDDFT Optical Absorption Spectra of Coinage Metal Dimers Supported on MgO(001)

LIST OF ABBREVIATIONS

AER	All Electron Relativistic
B3LYP	Becke three-parameter Lee-Yang-Parr
BLYP	Becke-Lee-Yang-Parr
BP	Becke Perdew
CASSCF	Complete Active Space Self Consistent Field
CC	Coupled Cluster
CCSD(T)	Coupled Cluster with Single and Double and Perturbative Triple excitations
CHARMM	Chemistry at HARvard Macromolecular Mechanics
CI	Configuration Interaction
CT	Charge Transfer
DFT	Density Functional Theory
DNP	Double Numerical with Polarization
DZ	Double Zeta
ECP	Effective Core Potential
EPE	Elastic Polarizable Environment
EXAFS	Extended X-ray Absorption Fine Structure
FAU	Faujasite
FMO	Fragment Molecular Orbital
GGA	Generalised Gradient Approximation
GTO	Gaussian Type Orbital
HF	Hartree Fock
HK	Hohenberg-Kohn
HMO	Hückel Molecular Orbital
HOMO	Highest Occupied Molecular Orbital
HPA	Hirshfeld Population Analysis
INDO	Intermediate Neglect of Differential Overlap
KS	Kohn-Sham
LCGTO-FF-DF	Linear combination of Gaussian-type orbitals

	fitting-functions density-functional
LDA	Local Density Approximation
LSDA	Local Spin Density Approximation
LUMO	Lowest Unoccupied Molecular Orbital
MBPT	Many Body Perturbation Theory
MCSCF	Multi-configurational self-consistent field
MINDO/1	Modified Intermediate Neglect of Differential Overlap
MM	Molecular Mechanics
MO	Molecular Orbital
MP2	Møller Plesset
MPA	Mulliken Population Analysis
NDDO	Neglect of Diatomic Differential Overlap
NTDM	Natural Transition Density Matrix
NTO	Natural Transition Orbital
ONIOM	Our-own-N-layered Integrated molecular Orbital + molecular Mechanics
PBE	Perdew-Burke-Ernzerhof
PES	Potential Energy Surface
PW	Perdew Wang
QM	Quantum Mechanics
QM/MM	Quantum Mechanics/Molecular Mechanics
QZ	Quadruple Zeta
SCF	Self Consistent Field
STO	Slater Type Orbital
TDDFT	Time Dependent Density Functional Theory
TDM	Transition Density Matrix
TZ	Triple Zeta
UFF	Universal Force Field
VWN	Vosko Wilk Nussair
ZORA	Zero Order Regular Approximation

LIST OF FIGURES

LIST OF TABLES

CHAPTER 1

Introduction

In the famous talk titled "There's plenty of room at the bottom" delivered in December, 1959, at the California Institute of Technology, Richard Feynman remarked

> I can hardly doubt that when we have some control of the arrangements of things on a small scale we will get an enormously greater range of possible properties that substances can have and, of different things that we can do.

Feynman's anticipation proved right when it was discovered only a few years later that assemblies of two to thousands of atoms exhibit properties that are completely different from what is known from solid state aggregates on one hand and single atoms on the other, and that the properties can be tailored by changing the size of the system atom by atom.

1.1 Metal Clusters

The term "cluster" was coined by F. A. Cotton in early 1960s. Metal clusters are aggregates of metal atoms which are linked by metal-metal bonds. In addition, ligands can also be present. The number of atoms in a cluster range from two to several hundreds of thousands. They constitute an intermediate form of matter where molecular properties begin to vanish whereas the features of a bulk metal are not yet established. Thus clusters form a sort of bridge between the atomic and bulk size regimes. One important characteristic of clusters is that it is possible to modify their physical and chemical properties by changing the size of the system, one atom

at a time, thus facilitating the design of materials for specific applications. This makes the study of clusters particularly interesting.

Clusters can be classified into homogeneous and heterogeneous depending upon whether they are composed of atoms or molecules of one kind or more than one kind. Whereas bulk solids possess overlapping energy bands, clusters exhibit discrete electronic energy levels as shown in Figure 1.1. This enables the tailoring of
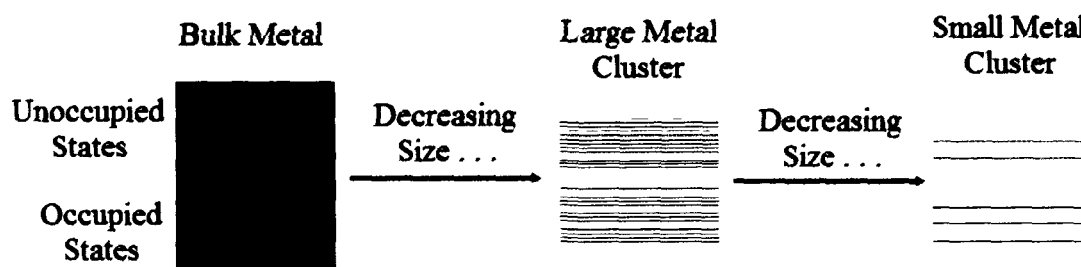
Figure 1.1 Energy levels of metals changing from continuous to discrete states on going from bulk metal to large and small clusters.

electronic properties of the cluster by varying its size and charge state. Besides electronic properties, chemical, thermal, mechanical, electrical, magnetic and optical properties of clusters also show significant size dependence. Figure 1.2 shows the different colours exhibited by gold nanoparticles with changing size.
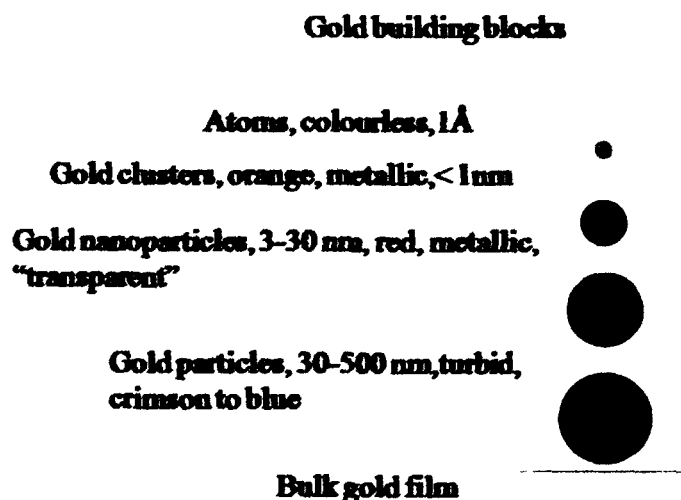
Figure 1.2 Change of colour of gold nanoparticles with size.

Metal nanoclusters have lower melting point compared to the corresponding bulk material. The band gap of semiconductor clusters varies significantly with size. Perhaps the most striking property of clusters is the very high surface-to-volume ratio compared to bulk material. As particle size decreases, the ratio of surface atoms to interior atoms increases. For example, a 38 atom cuboctahedral cluster has 32 surface atoms and 6 interior atoms, while a 13 atom icosahedral cluster has twelve surface atoms and only one interior atom. These surface atoms have low co-ordination and can serve as active sites. Clearly, cluster materials are chemically more reactive than bulk materials.

The physical and chemical properties of metal clusters are determined by the valence electron states which are not localized to single atoms but to the cluster as a whole. The delocalized electrons occupy states in an effective potential just like protons and neutrons in an atomic nuclei. Thus metal clusters exhibit electronic shell structures with corresponding magic numbers. This shell structure gets reflected in many size dependent properties like fragmentation energy, ionization energy, electron affinity and polarizability. According to the electronic shell model, the numbers which correspond to shell closings are called magic numbers. In case of alkali metals which have one valence s electron and the coinage metals with electronic configuration $nd^{10}(n+1)s^{1}$, clusters having magic number of atoms are found to be exceptionally stable. Lithium clusters with having number of atoms 2, 8, 20, 34, 40, 58,....have been found to be highly stable.[1]

Much of the interest in clusters is fuelled by their many possible applications and the related nanoscale technologies. Nanoclusters not only exhibit interesting electronic and optical properties intrinsically associated with their low dimensionality and the quantum confinement effect, but also represent the critical components in potential nanoscale electronic[2] and photonic device applications.[3,4,5] Mention may be made of the wide use of nanoclusters in optical data storage, as fluorescent labels for biological studies and in improved sensors besides heterogeneous catalysis. Due to their wide spread applications, both homogeneous and heterogeneous metal clusters have been widely studied.[6,7]

1.1.1 Variation of cluster properties with size

The physical and chemical properties of nanoclusters are found to exhibit

profound size dependence. This facilitates the design of nanoclusters for various applications by controlling their size. Properties like quantum confinement effect in semiconductor nanoparticles, surface plasmon resonance in metal nanoparticles and superparamagnetism in magnetic clusters are found to vary with size.

1) Cluster Stability

It is seen that clusters having an even number of valence electrons are more stable than those with odd number of valence electrons. In Figure 1.3 we show the mass spectrum of sodium clusters with N = 4-100. Large peaks are seen at N = 8, 20, 10 and 58. Higher counting rate indicates greater abundance and hence higher stability.
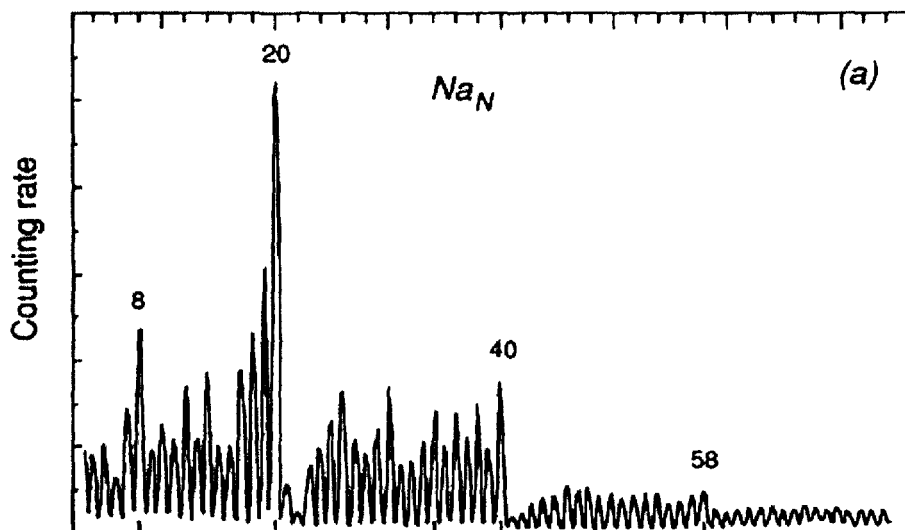
Figure 1.3 Experimental Na cluster abundance spectrum. (taken from reference 66)

2) Ionization Potential

Ionization potential of metal clusters vary with cluster size. Figure 1.4 shows the one-photon ionization mass spectra of silver nanoclusters upto a system size of 100. It is seen from the plot that ionization potential of silver clusters have an oscillatory nature with the even numbered clusters having higher value of ionization potential compared to the odd numbered ones. The ionization potential is exceptionally high for the cluster sizes 18, 20, 34, 40, 48, 58 and 92. Higher value of ionization potential indicates greater stability.
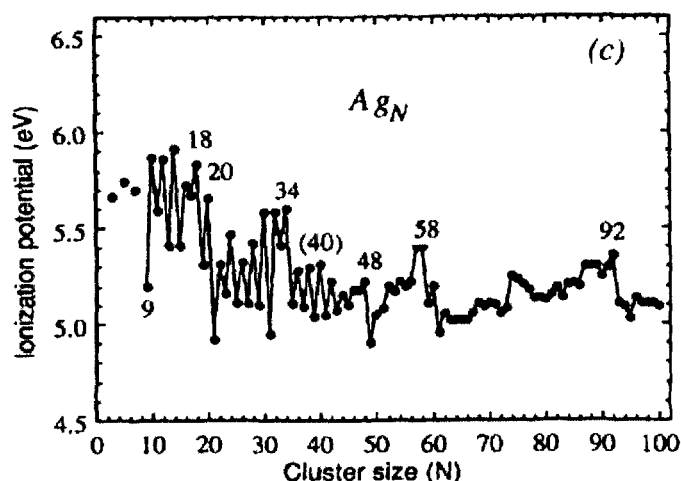
Figure 1.4 Ionization potential of silver clusters. (taken from reference 67)

3) Reactivity

It is seen that the reactivity of metal clusters depend on the size and charge state of the cluster. Figure 1.5 shows the experimental plot of reactivity of gold cluster anions Au_n^- (n = 2-20) towards CO and O_2. The plot shows odd-even oscillation in reactivity. Molecular oxygen adsorbs more strongly on clusters having even number of gold atoms with the reactivity being highest for Au_6^-. In case of CO, even-odd oscillations start at a cluster size of ten atoms. Gold clusters with odd number of atoms react more strongly with CO than those with even number of atoms.
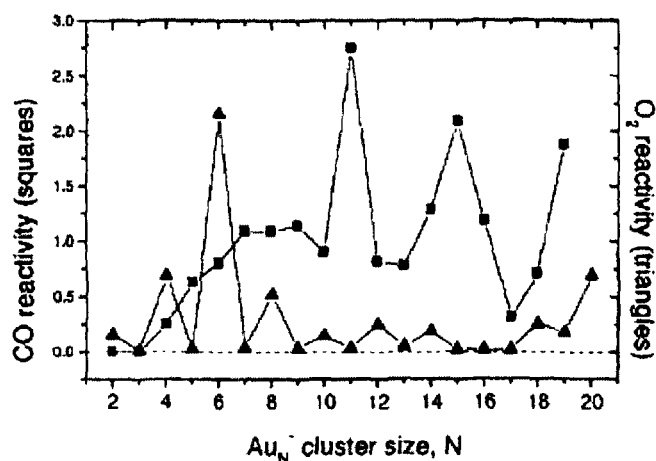
Figure 1.5 Variation in the reactivities of CO (squares) and O_2 (triangles) towards gold cluster anions Au_n^- when a 20% reactant gas: He mixture is pumped into the flow-tube reactor. (taken from reference 64).

4) Melting Temperature

Melting temperature of nanoclusters increases with cluster size. Figure 1.6 shows the variation of melting temperature of Au and CdS nanoclusters with size. It is seen that for lower size of the cluster, upto about 10 nanometers, the melting temperature increases rapidly with size while for larger nanoclusters the rise is more gradual.
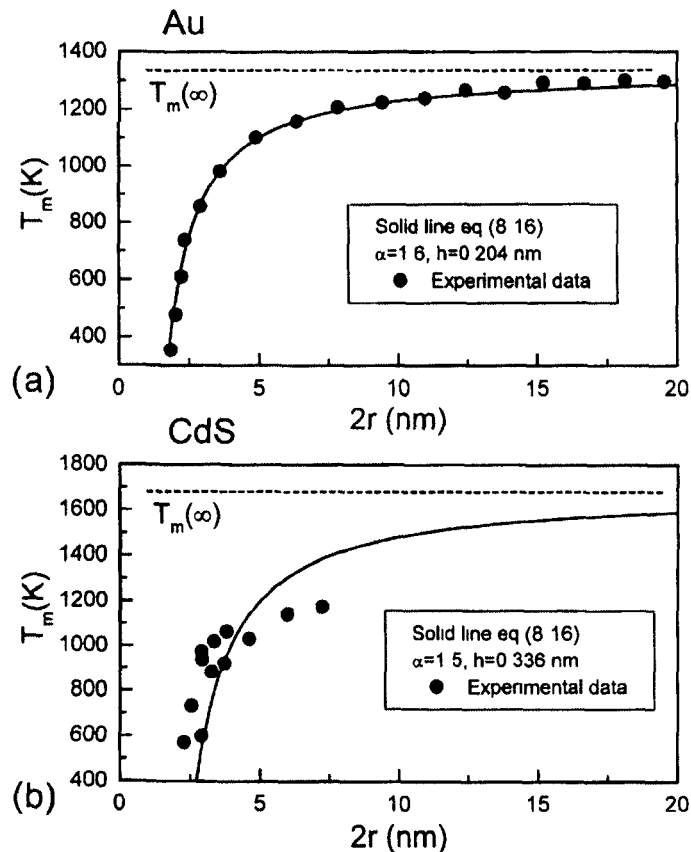
Figure 1.6 Dependence of the melting temperature T_m on the size of (a) gold and (b) CdS nanoparticles (taken from reference 63).

1.2 Transition Metal Clusters

Transition metals contain unfilled d shells. The presence of unfilled d shells gives rise to a large number of low-lying excited states due to the different possibilities of arranging the electrons among the unfilled shells. The d electrons give rise to directional bonds. If the d electrons retain their atomic character and remain localized, the cluster will be magnetic. But increased s-d and d-d hybridization will lead to a decrease in the magnetic moment. This immense possibility of tuning the electronic structure and hence properties makes the study of transition metal clusters particularly interesting.[8,9] As the energy gap between the

(n+1)s and nd levels is very small, electronic structure and chemical properties of these clusters are determined by the interplay between s and d electrons. Among the transition metals, clusters of coinage metals have been widely studied[10,11] mainly because of their industrial applications. These metals with their filled d shell and singly occupied s shell [electronic structure nd^{10}(n+1)s^1, with n = 3, 4 and 5 for Cu, Ag and Au, respectively] can be regarded as a bridge between the "simple" s-only alkali metals and the more complicated transition metals. Coinage metals may be regarded as perturbed s^1-electron systems with the (filled) d-shell influence increasing from copper to gold. Gold exhibits properties very different from the other two coinage metals, viz, copper and silver, mainly due to relativistic effect.

1.3 Synthesis of metal clusters

There are two basic approaches for manufacturing metal clusters. The "Bottom Up" approach builds the cluster by assembling individual atoms and molecules. The other approach which is called "Top Down" reduces macroscopic particles to nano size scale. This route is not well suited to preparing uniformly shaped particles.[12] Bottom-up procedures are much better suited to generating uniform particles, often of distinct size, shape and structure. Botton-up methods start with atoms that aggregate in solution or even in the gas phase to form particles of definite size, if appropriate experimental conditions are applied. We shall discuss the bottom-up procedure in detail.

1.3.1 Gas Phase Synthesis

Figure 1.7 shows a schematic diagram of a cluster-beam generator. It consists of a heating unit where metal targets are evaporated by simple heating, or by laser irradiation. The flow of atoms then passes through several slits constructed to focus the beam. Modern techniques use mass spectrometric units to separate different particles according to mass, leading to fractions of very uniform particles. The disadvantage of this method is the lack of a protecting skin for the clusters. Bare metal clusters aggregate into polycrystalline powders due to thermodynamic stability of the metal-metal bonds. Thus the particles lose individuality. A solution to this problem is achieved by forming the particles on supports or by making the particles react with ligands in solution.[12] The naked particles of a cluster beam react with molecules covering their surface faster than they react with each other.
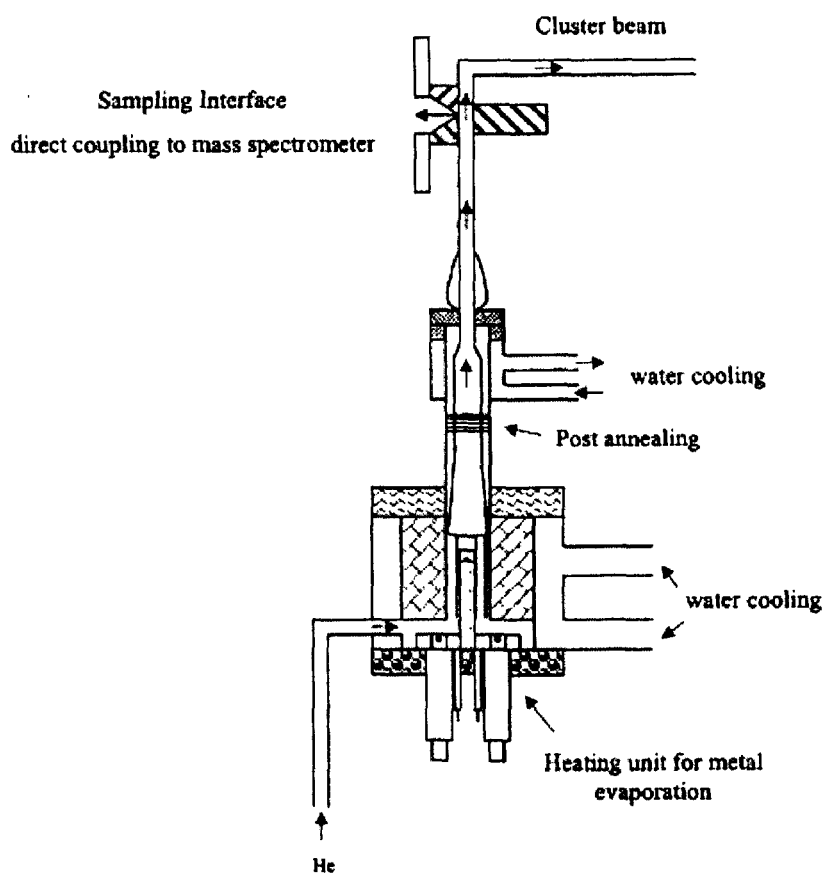
Figure 1.7 Simplified sketch of a cluster beam generator on the basis of a generator described in reference 65. (taken from reference 11)

1.3.2 Chemical Synthesis

The most common synthetic route to production of nanosized metal particles is the reduction of positively charged metal atoms, either as pure ions or centres of metal complexes in solution.[13] Solvents can vary from water to very nonpolar media like hydrocarbons depending on the nature of the salt or the complex used. The nature of the metal compound also determines the kind of reducing agent to be applied. Common reducing agents are gaseous hydrogen, hydrilic compounds and alcohol. The nano clusters have to be produced in the presence of molecules that will cover the surface. This is the most crucial step in cluster formation. If the ligands are already present before the reduction starts then formation of larger clusters may be prevented by blocking cluster growth. On the other hand, if ligands are added later, then it is difficult to determine when the cluster growth has to be stopped. Thus it involves an interplay between generation of metallic precipitates on one hand and formation of mono or oligonuclear complexes on the other. Other less

frequently used methods for formation of metal nanoparticles include thermal decomposition of organometallic compounds,[13] ligand reaction and displacement from organometallics, photolysis and radiolysis.

1.4 Gold Nanoclusters

Gold is regarded as "the king of elements". Few materials have exercised as much of a hold on human history and civilization as has gold. About 75% of all gold produced today is consumed in jewellery alone. Gold metal and gold alloys are used in electrical and electronics industry for various applications including electroplating. Gold surfaces are used for surface engineering. Gold nanoclusters both in the gas phase and on supports serve as active sites for catalytic reactions. Gold salts and gold complexes serve as homogeneous catalysts for organic reactions and exhibit properties like luminescence, liquid crystalline or non-linear optical behaviour. The ancient Romans were among the world's first nanotechnologists. They worked out how to make red glass using a process that converts gold metals into particles 10 nanometers across. At this size gold glows ruby red. Medieval artisans produced stained glass by mixing gold and silver in such a way so as to result in tiny spheres which reflect sunlight producing a variety of colours. Michael Faraday was the first to scientifically investigate gold colloid formation in the mid nineteenth century. He reduced a solution of $HAuCl_4$ with elemental phosphorus resulting in the formation of ruby-red gold sols. It is now known that the reason for this colour is the interaction of visible light with the surface electrons of gold nanoparticles. In the following sections we describe some important properties of gold nanoclusters.

1.4.1 Aurophilic Interactions

The term aurophilicity[14] is used to describe various kinds of Au-Au interactions within and between gold compounds. This term is derived from the Latin word "Aurum" (gold) and the Greek word "Philos" (with an affinity for). Such interactions are most evident among the formally closed-shell Au^I centres (with $5d^{10}$ valence electronic configuration). The Au-Au bond distances range from 2.7 to 3.3 Å. Such a phenomenon is also observed in polynuclear compounds where the gold atoms seem to be drawn to each other, which results in Au-Au distances of

around 3 Å. These distances are shorter than the sum of two van der Waals radii (3.7 Å). "Aurophilicity" was proposed to express the specificity of the unexpected attraction between two or more gold centres in compounds where the metals are already chemically saturated according to conventional valence concepts. Gold atoms interact with other gold atoms in neighboring molecules ignoring all other potential donor or acceptor sites. A generalization of aurophilicity is metallophilicity. Some strengths of interactions between pairs of gold atoms have been measured by temperature dependent NMR spectroscopy and found to have values in the range 29-46 kJ/mol which is comparable to that of a hydrogen bond,[15] and is intermediate between ionic/covalent bonding and van der Waals interaction. Experimental evidence for the existence of aurophilic contacts come from Raman spectra and electronic absorption and emission spectroscopy. It is observed that some Au-Au bonded species show intense photoluminescence in the UV/vis region.[16,17] Aurophilic mechanism can coexist with covalent bonding, for example, in the [{AuPH$_3$}$_4$]$^{2+}$ model system.[18] There are also evidences of the coexistence of aurophilic interaction and hydrogen bonding.[19] Theoretical studies on such systems led to the conclusion that the hydrogen bond loses strength and directionality in order to retain the gold-gold interaction.[20] It has been estimated that about 17% of the cohesive energy of bulk gold, or 0.015 eV/Au-Au pair comes from aurophilic interactions.[21] Aurophilicity is attributed to electron correlation of the closed-shell components, somewhat similar to van der Waals interactions, but much stronger. Therefore it is sometimes referred to as "Super van der Waals interactions".[15] In polynuclear compounds aurophilicity leads to clustering of gold atoms/cations at virtually any donor site (halides, hydroxides, mercaptides, amines, phosphines, methane, activated methyl etc.).[22] Good theoretical explanation of aurophilic interactions requires the inclusion of relativistic effects. Such interactions are absent or negligible in gold(III) compounds.

1.4.2 Relativistic Effects

Relativistic effects occur due to the finite speed of light, i.e, due to the nonadditivity of velocities. In light atoms relativistic effects are not significant as the velocities of all the electrons are orders of magnitude smaller than c, the velocity of light. But the situation changes drastically when we move over to heavy atoms. In such atoms the

inner electrons which are very strongly attracted by the electrostatic field of the nucleus, move very fast. For example in gold (Z = 79), electrons in the 1*s* orbital move with a velocity which is 60% that of light. As a result the relativistic mass increases by about 25% of the rest mass. The effective Bohr radius of the electron from the nucleus decreases which leads to the contraction of the 1*s* orbital and a stabilization of the energy levels. As the *s* orbitals of higher principal quantum numbers have to be orthogonal to the 1*s* orbital, they suffer a concomitant contraction. For elements in the mass range of gold, this effect is felt upto the 6*s* orbital. The 2*p* orbital also undergoes a similar contraction as it also experiences very strong electrostatic effects of the nucleus. Again following the orthogonality argument, the outer *p* orbitals also contract. The contraction of the 1*s* and 2*p* orbitals leads to stronger screening of nuclear potential and hence the *d* and *f* orbitals are expanded and get destabilized. Expansion of the 5*d* orbital and contraction of the 6*s* orbital lead to change in the corresponding energy levels and increases the interaction between them. Thus due to relativistic effects, bonding interactions requiring *sd* hybridization are enhanced. Relativity leads to stronger coupling between each electron's spin and orbital angular momentum than would be found for lighter elements, thus necessitating j-j coupling, rather than L-S coupling to describe multi electron systems in case of heavy elements. Relativistic effects scale roughly as Z^2. It is noteworthy that relativistic effect in gold is higher than in any other element with Z<100.[23] Figure 1.8 depicts the core contraction of the 6s orbital for elements Cs to Fm shown as the ratio of average electron-nuclear distances obtained from a relativistic $< r >_R$, and non relativistic $< r >_{NR}$ calculation. Very high relativistic effects in gold lead to the differences in properties between gold and the other coinage metals, most notably silver, though they belong to the same group in the periodic table. It has been found that Au-Au contact in metallic gold is less than Ag-Ag contact in metallic silver. Also Au(I) has been found to be smaller in size compared to Ag(I).[24] Relativistic effects also account for the high electron affinity of gold relative to silver and for the existence of aurides (eg, Cs^+Au^-) which are non-metallic semiconductors.[25] This is also the reason why the first ionization potential of gold is much higher than silver (IP1 for Au 9.225 eV, IP1 for Ag 7.576 eV).[26] The tighter binding of the *s* electron in case of gold leads to higher cohesion energy of gold metal and higher melting point. The yellow color of gold is also attributed to
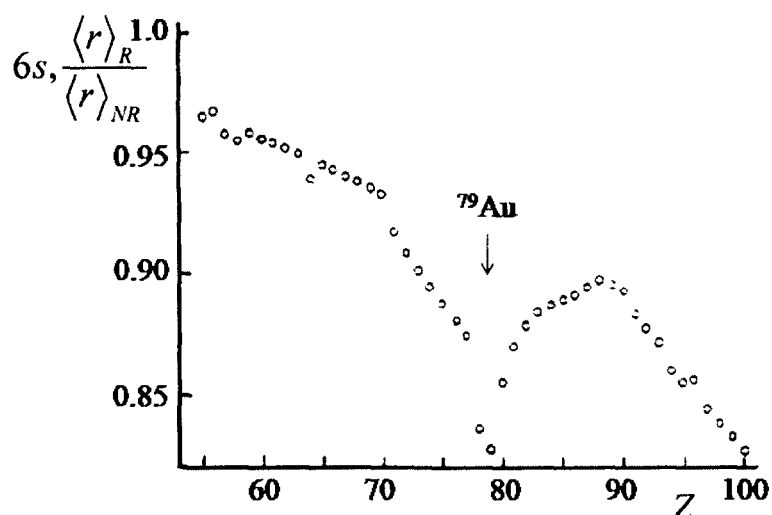
Figure 1.8 The ratio of relativistic and non relativistic shell radii in the atomic ground states of the elements 55-100.[27]

relativistic effects. The preference of gold clusters for two dimensional structures upto large system size is also due to relativistic effect. Influence of relativistic effect on calculated properties of some small molecules involving gold are presented in Table 1.1. There are two ways of treating relativistic effects in quantum mechanical calculations. The first, called scalar-relativistic methods, do not include spin-orbit interaction. The second, called Zero Order Regular Approximation (ZORA),[28,19] is a fully relativistic method that includes spin-orbit interaction. It should be noted that improvements in the calculated properties due to the inclusion of spin-orbit interaction in the Hamiltonian is only marginal, the major relativistic effects are described at the scalar relativistic level.

Table 1.1 Relativistic benchmark results on atomic gold, [AuH], [Au$_2$] and Au(s). (Taken from Reference 23)

System	Property[a]	Exp.	R	NR	R-NR	Method
Au(atom)	IP[eV]	9.22554(2)	9.197	7.057	2.14	CCSD
	EA[eV]	2.30863	2.295	1.283	1.012	CCSD
	α	30(4)	36.06			CCSD(T)
Au$^+$	α		12.75			CCSD(T)
AuH	R$_e$[pm]	152.4	152.5	175	-22.5	AE CCSD(T)
			152.7	174.7	-22.0	PP CCSD(T)
			151.0		0.0[b]	PP CCSD(T)
	ω_e[cm^{-1}]	2305	2288	1565	723	AE CCSD(T)
			2306	1575	731	PP CCSD(T)
			2330		6[b]	PP CCSD(T)
	D$_e$[eV]	2.302(8)	2.92	1.79	1.13	AE CCSD(T)
			3.124	2.086	1.038	PP CCSD(T)
			3.31		0.03[b]	PP CCSD(T)
Au$_2$	R$_e$	247.2	248.8			AE cp CCSD(T)
	ω_e[cm^{-1}]	191	187			AE cp CCSD(T)
	D$_e$[eV]	2.302(8)	2.19			AE cp CCSD(T)
			2.23		0.06[b]	PP CCSD(T)
Au(solid)	a$_0$[pm]	408	407	429	-22	
	E$_{coh}$(eV)	3.81	3.96	3.03	0.93	
	B$_0$[Gpa]	173.2	182	108	74	
	E$_{interband}$[eV]	2.24	2.38	4	-1.62	

[a] Dipole polarizability, α in atomic units. Bond lengths R$_e$ in pm, vibrational frequencies ω_e in cm^{-1}, and dissociation energies D$_e$ in eV. For solids, a$_0$ is the lattice parameter, E$_{coh}$ is the cohesive energy and E$_{interband}$ is the interband energy from the top of the 5d band to the Fermi level. R= relativistic, NR= non relativistic. [b] SO contribution.

1.4.3 Oxidation States

The gold atom is known to support several oxidation states from -1 to +5 and so it is chemically very rich. The most common oxidation states are +1 and +3, while +5 has only been observed in fluoro gold compounds. The local co-ordination in these three cases are in general linear (+1), quadratic planar (+3) and octahedral (+5). That gold can exist in several oxidation states has been demonstrated both experimentally and theoretically. For example, in (AuX$_2$)^q, X = Cl, Br, mass-spectroscopic experiments in combination with theoretical calculations reveal that

gold can have three oxidation states $+1$, $+2$ and $+3$ corresponding to the total charges q of -1, 0 and $+1$, respectively.[29] For the Au^{2+} atom, both monomeric open-shell Au^{2+} compounds as well as dimeric closed-shell compounds are known to exist. There is one report of the existence of Au^{4+} compound by Puddephatt and Vittal.[30] Oxidation state 0 exists not only in solid gold and clusters but also in some compounds. Also, there is evidence of the existence of the oxidation state -1, for example, in cesium auride, Cs^+Au^-. The existence of several oxidation states in gold is attributed to relativistic effect. Due to the very strong relativistic effect in gold there is a high tendency for the $6s$ and $5d$ orbitals to hybridize, thus leading to a wide range of oxidation states.

1.4.4 Applications of gold nanoclusters

The driving force behind fundamental research into nanoclusters is the perceived and demonstrated properties that can be exploited into practical applications. Below we describe some of the most common applications of gold nanoclusters.

1) Homogeneous and Heterogeneous Catalysis

In the bulk state gold is chemically inert and so it was believed to be unimportant in catalysis. However, the pioneering work of Haruta[31,32] demonstrated the exceptionally high reactivity and/or selectivity of ultrafine gold particles (2nm $\leq$ diameter $\leq$ 5nm) supported on certain metal oxides like MgO, Al_2O_3, TiO_2 etc. towards combustion of CO and saturated hydrocarbons. He found that gold nanoparticles could be used to convert toxic CO to the benign CO_2 at room temperature and at temperatures as low as $-70\,^\circ C$. Around the same time it was demonstrated that gold could be an extraordinarily good catalyst for the hydrochlorination of acetylene to vinyl chloride. Today supported gold clusters are used in reactions like NO reduction, N_2O decomposition, water-gas shift reaction, partial oxidation of hydrocarbons, hydrogenation of carbon oxides, unsaturated carbonyl compounds, alkynes and alkadienes. Most of these reactions occur with higher degrees of selectivity over gold catalysts compared to other metal catalysts. Supported gold nanocluster catalysts find applications in areas like indoor air quality control, pollution abatement and production of H_2 energy carrier.

2) Sensors

Biosensors are sensors that consist of biological recognition elements often called bioreceptors or transducers. Gold nanoparticles find applications as optical, electrochemical and piezoelectric biosensors. There is a recent report[33] of the feasibility of using gold nanocluster based fluorescent sensors for detection of cyanide in water, soil, food and biological samples. Gold nanoparticles can also be used as NO_x sensors. Thus they are effective in environmental pollution control.

3) Medicine

One of the major applications of nanotechnology is in biomedicine. Gold nanoparticles can be engineered as nanoplatforms for effective and targeted drug delivery. They are also used in medical diagnostic devices and for the detection and treatment of cancerous cells. Highly fluorescent sub-nanometer sized gold nanoclusters can be used for subcellular imaging. The red fluorescence of the nanoclusters enhances biomedical images of the body as there is reduced background fluorescence and better tissue penetration.

4) Electronics

Gold nanoparticles find use in novel printed gold inks for low temperature printing applications. They are also used in optical and photonic devices, and as tips and contacts in electronic devices. Researchers[34] have developed a new memory device that uses gold nanoparticles and the organic semiconducting compound pentacene. This novel pairing is a key step forward in the efforts to develop organic plastic memory devices, which can be considerably cheaper and more versatile than the conventional silicon based devices used in computers, flash drives and other applications.

1.4.5 Theoretical Study of gold nanoclusters

The successful investigation of small clusters dates back to the 1980s.[35,36] The interest in clusters reached an extraordinary degree with the assembly of carbon based fullerenes. There has been a lot of focus on the properties of small metal clusters for three decades now and hence have been extensively investigated both

theoretically and experimentally.[37-41] There has been a lot of theoretical investigations regarding the structure of small gold clusters. Häkkinen and Landman[42] and Grönbeck and Andreoni[43] carried out density functional studies on neutral and anionic gold clusters and predicted minimum structures upto the decamer. Häkkinen and Landman[42] located the planar-3D transition for neutral and anionic clusters at n = 7 and n = 6 respectively. However, a DFT calculation by Gronbeck and Broqvist[44] revealed that the Au_8 cluster prefers a two dimensional configuration. On analysing the electronic structure, they found a substantial hybridization between $(n-1)d$ and ns orbitals. The preference of planar configurations for Au is traced to a sizable d-d overlap and d-electron delocalization. However, ab-initio calculations at the MP2 and CCSD(T) level of theory reveal the lowest Au_8 isomer to be nonplanar.[45] Another DFT study by A. V. Walker[46] found that for neutral clusters, the 2D-to-3D crossover occurs at Au_{11}. Cationic structures have been found to be planar upto n = 7. However, 3D structure starts appearing at n = 8.[47,48]

The interest in hydrogen chemistry on gold clusters has been stimulated by the recent discovery that supported gold clusters catalyse the hydrogenation of ethylene, 1,3-butadiene, 1-butene,[49] acrolein[50] and the partial hydrogenation of acetylene to ethylene.[51] Varganov *et al.*[52] have investigated the reactions of molecular hydrogen with small gold clusters with two and three atoms. They have found that molecular hydrogen easily binds to neutral Au_2 and Au_3 clusters with binding energies of 0.55 eV and 1.10 eV, respectively. The barrier heights to H_2 dissociation on these clusters with respect to Au_nH_2 complexes are 1.10 eV and 0.59 eV for n = 2 and n = 3. Although negatively charged Au_n^- clusters do not bind molecular hydrogen, H_2 dissociation can occur with energy barriers of 0.93 eV for Au_2^- and 1.39 eV for Au_3^-. The energies of the $Au_2H_2^-$ and $Au_3H_3^-$ complexes with dissociated hydrogen molecules are lower than the energies of $Au_2^- + H_2$ and $Au_3^- + H_2$ by 0.49 eV and 0.96 eV, respectively.

The interaction of CO with transition-metal and main-group-element atoms, clusters and surfaces plays a very important role in material science and chemical industry.[53,54] Many industrial processes employ CO as reagent and transition-metal compounds as heterogeneous catalysts and involve the intermediates of metal carbonyls. As noble-metal compounds, gold carbonyls have been the subject of a number of studies. The first carbonyl derivative of gold, Au(CO)Cl, was reported in

1925.[55] Neutral gold mono and dicarbonyls have been successfully synthesized in rare-gas matrixes by several groups.[56] Recently, it has been found that gold becomes catalytically active when deposited on select metal oxides as hemispherical ultrafine particles with diameters smaller than 5 nm.[57] The supported Au nanoparticles exhibit remarkable catalytic activities and/or excellent selectivities in a number of reactions such as low-temperature CO oxidation[58,59] and reduction of nitrogen oxides.[57] Interestingly enough, the activity of gold clusters has been found to depend critically on the size of the particle and the nature of the substrate. For example, when supported on the $Mg(OH)_2$ surface, the best catalytic activity for oxidation of CO is observed for a system size of 13 atoms[60] while the optimal activity of gold clusters supported on TiO_2 surfaces occurs for sizes of 2-3 nm (corresponding to a few hundred atoms, approximately). In general, probe molecules are used to gain insight into the chemisorption characteristics and catalytic activity of nanoclusters. Jiang *et al.*[61] have performed a DFT calculation on the adsorption of CO on gold atoms and small gold clusters Au_n (n = 1-5). They found that the Au atom forms both mono and dicarbonyls. AuCO is predicted to have a bent geometry with a $^2A'$ ground state which lies 4.51 kcal/mole lower than the linear structure. $Au(CO)_2$ is predicted to have a $^2A_1$ ground state with C_{2v} symmetry and the $Au_2(CO)_2$ molecule is predicted to be linear. These results are in good agreement with experimental values. Another DFT study has been undertaken by Phala *et al.*[62] They studied CO adsorption on Au_n(n = 1-13) clusters and determined the optimized geometries of the clusters before and after CO adsorption. They found that CO binding onto the on-top site of the gold clusters is the most favourable configuration, except for Au_{13}. The on-top and bridge configurations are degenerate on Au_5.

In spite of there being a huge volume of work done on gas phase and supported gold nanoclusters, there still exists a number of open questions, some of which will be addressed in the present thesis.

1.5 OBJECTIVES OF THE PRESENT WORK

The work presented in this Ph. D. thesis was undertaken with the following objectives in mind.

1. Systematic investigation of structural and electronic properties of small gas phase neutral and singly charged cationic and anionic gold nanoclusters

based on Density Functional Theory (DFT).

2. Study the reactivity of the minimum energy cationic, neutral and anion Au_n clusters (n = 2-13) on the basis of conceptual density functional theory.

3. DFT studies of adsorption and co-adsorption of oxygen and carbon monoxide on gas phase and zeolite supported gold nanoclusters.

4. Study the phenomenon of reverse hydrogen spillover in zeolite supported gold clusters by QM   method .

5. Study of optical spectra of coinage metal dimers supported on MgO(001) surface by TDDFT.

References

[1]   Harbola, M. K. Magic numbers of metallic clusters and the principle of maximum hardness. *Proc. Natl. Acad. Sci. USA.*, **89**, 1036-1039 (1992).

[2]   Yang, Y.; Chen. S. Surface manipulation of the electronic energy of subnanomeer-sized gold clusters: an electrochemical and spectroscopic investigation. *Nano Lett.*, **3**, 75-79 (2003).

[3]   Brongersma, M. L., Nanoscale photonics: nanoshells: gifts in a gold wrapper. *Nat. Mat.*,**2**, 296-297 (2003).

[4]   Andres, R. P. *et al.* Coulomb staircase at room temperature in a self-assembled molecular nanostructure. *Science*, **272**, 1323-1325 (1996).

[5]   Dorogi, M.; Gomez, J.; Osifichin, R.; Andres, R. P.; Reifenberger, R. Room-temperature Coulomb blocade from a self-assembled molecular nanostructure. *Phys. Rev. B*, **52** 9071- 9077 (1995).

[6]   Kabir, M.; Mookerjee, A.; Kanhere, D. G. *Magnetism in pure and doped manganese clusters. Lecture series on computer and computational sciences*, **4**, 1018-1021, Brill Academic Publishers, The Netherlands (2005).

[7]   Dutta, S.; Kabir, M; SahaDasgupta, T.; Sarma D. D.; First principle study of structural stability and electronic structure of CdS nanocrystals. *J. Phys. Chem. C.* **112**, 8206-8214 (2008).

[8]   Kabir, M. Mookerjee, A.; Kanhere, D. G. Structure, electronic properties and magnetic transition in manganese clusters. *Phys. Rev. B.*, **73**, 224439-1 − 224439-11 (2006).

[9]   Kabir, M.; Kanhere, D. G.; Mookerjee, A. Large magnetic moments and anomalous exchange coupling in As-doped Mn clusters. *Phys. Rev. B*, **73**, 75210-1 − 75210-5 (2006).

[10]   Kabir, M. Mookerjee, A.; Bhattacharya, A. K. Structure and stability of Cu clusters: A tight-binding molecular dynamics study. *Phys. Rev. A.* **69**, 043203-1-043203-10.

[11]   Häkkinen, H.; Moseler, M.; Landman, U. Bonding in Cu, Ag and Au clusters: Relativistic effects, trends and surprises. *Phys. Rev. Lett.* **89**, 033401-1 − 033401-4 (2002).

[12]   Schmid, G. *Nanoscale Materials in Chemistry* Ed. Klabunde, K. J. John Wiley & Sons, Inc., 2001

[13] *Cluster and Colloids. From Theory to applications.* Ed. Schmid, G. VCH, Weinheim (1994)

[14] Scherbaum, F.; Grohmann, A.; Huber, B.; Krüger, C.; Schmidbaur, H. "Aurophilicity" as a consequence of relativistic effects: the hexakis (triphenyl-phosphaneaurio) methane dicatopn [(PH$_3$PAu)$_6$C]$^{2-}$. *Angew Chem Int. Ed.* **27**, 1544-1546 (1988).

[15] Pyykkö, P. Strong closed-shell interactions in inorganic chemistry. *Chem. Rev.* **97**, 597-636 (1997).

[16] a) Assefa, Z. *et al.* Syntheses, structures and spectroscopic properties of gold(I) complexes of 1,3,5-Triaza-7-phosphaadamantane (TPA). Correlation of the supramolecular Au.cntdot. .cntdot. . cntdot.Au Interaction and photoluminescence for the species (TPA)AuCl and [(TPA-HCl)AuCl]. *Inog. Chem.* **34**, 75-83 (1995). b) Zhang, T.; Drouin, M.; Harvey, P. D.; Preparation, spectroscopic characterization, and frontier MO study of the heteronuclear luminescent [Pt$_2$Au$_2$(dmb)$_2$(PPh$_3$)$_4$](PF$_6$)$_2$ cluster (dmb=1,8-diisocyano-p-menthane). A cluster with formal Au^0-Au^0 bond encapsulated inside a "Pt$_2$(dmb)$_2$$^{2+}$" fragment. *Inorg. Chem.* **38**, 4928-4936 (1999). (c) Yam, V. W-W.; Lai, T-F.; Che, C-M. Novel luminescent polynuclear gold(I) phosphine complexes. Synthesis, spectroscopy and x-ray crystal structure of (Au$_3$(dmmp)$_2$]$^{3+}$[dmmp=bis (dimethylphosphinimethyl)methylphosphine]. *J. Chem. Soc., Dalton Trans.,* 3747-3752 (1990).

[17] Li, D. *et al.* Spectroscopic properties and crystal structures of luminescent linear tri-and tetra-nuclear gold(I) complexes with bis (diphenylphosphinomethyl) phenyl-phosphine ligand. *J. Chem. Soc., Dalton Trans.,* 1, 189-194 (1993).

[18] Pyykkö, P.; Runeberg, N. Calculated properties of the 'empty' [AuPH$_3$]$^{2+}$$_4$ and related role of systems: role of covalent and correlation contributions. *J. Chem. Soc., Chem. Commun.* **24**, 1812-1813 (1993).

[19] Schneider, W.; Bauer, A.; Schmidbauer, H. (Isocyanide)gold(I) thiosalicylates: supramolecular assembly based on both aurophilic and hydrogen bonding. *Organometallics,* **15**, 5445-5446 (1993).

[20] Codina, A. *et al.* Do Aurophilic interactions compete against hydrogen bonds? Experimental evidence and rationalization based on *ab initio* calculations. *J. Am. Chem. Soc.*, **124**, 6781-6786 (2002).

[21] Rehr, J. J.; Zaremba, E; Kohn, W. van der Waals forces in the noble metals. *Phys. Rev. B*, **12**, 2062-2066 (1975).

[22] Schmidbauer, H. High-carat gold compounds. *Chem. Soc. Rev.* **24**, 391-400 (1995).

[23] Pyykkö, P. Theoretical chemistry of gold. *Angew. Chem. Int. Ed.* **43**, 4412-4456 (2004).

[24] (a) Bayler, A.; Schier, A.; Bowmaker, G. A.; Schmidbauer, H. Gold is smaller than silver. Crystal structures of [Bis(trimesithylphosphine)gold(I)] and [Bis(trimesithylphosphine)silver(I)] tetrafluoroborate. *J. Am. Chem. Soc.*, **118**, 7006-7007 (1996). (b) Tripathi, U. M.; Bauer, A.; Schmidbauer, H. Covalent radii of four-co-ordinate copper(I), silver(I) and gold(I): crystal structures of [Ag(AsPh$_3$)$_4$]BF$_4$ and [Au(AsPh$_3$)$_4$]BF$_4$. *J. Chem. Soc., Dalton Trans.*, 2865-2868 (1997).

[25] Spicer, W. E.; Sommer, A. H.; White, J. G. Studies of the semiconducting properties of the compound CsAu. *Phys. Rev.* **115**, 57-62 (1959).

[26] Moore, C. E. in *Atomic Energy Levels*, Vol. III, Natl. Bur. Std. (U. S.) Circ. No. 467 (U. S. GPO, Washington, D. C.) (1958).

[27] Pyykkö, P.; Desclaux, J. P. Relativity and the periodic system of elements. *Acc. Chem. Res.* **12**, 276-281 (1979).

[28] Lenthe, E. van; Baerends, E. J.; Snijders, J. G. Relativistic regular two-component Hamiltonians. *J. Chem. Phys.*, **99**, 4597-4610 (1993).

[29] Schröder, D. *et al.* Gold dichloride and gold dibromide with gold atoms in three different oxidation states. *Angew. Chem. Int. Ed.* **42**, 311-324 (2003).

[30] Puddephatt, R. J.; Vittal, J. J. in *Encyclopedia of inorganic chemistry*, Vol. 3 (Ed.: R. B. King), Wiley, Chichester, 1320-1331 (1994).

[31] Haruta, M.; Yamada, Y.; Kobayashi, T.; Iijima, S. Gold catalysts prepared by co-precipitation for low-temperature oxidation of hydrogen and of carbón monoxide. *J. Catal.* **115**, 301-309 (1989).

[32] Haruta, M. Size- and support-dependency in the catalysis of gold. *Catal. Today*, **36**, 153-166 (1997).

[33] Liu, Y.; Ai, K.; Cheng, X.; Huo, L.; Lu, L. Gold-nanocluster-based fluorescent sensors for highly sensitive and selective detection of cyanide in water. *Adv. Funct. Mater.* **20**, 951-956 (2010)

[34] Leong, W. L.; Lee, P. S.; Mhaisalkar, S. G.; Chen, T. P.; Dodabalapur, A. Charging phenomenon in pantacene-gold nanoparticles memory device, *Appl. Phys. Lett.*, **90**, 042906-1 – 042906-3 (2007).

[35] Andres, R. P. *et al. Physics and Chemistry of Finite Systems: From Clusters to Crystals.* Kluwer, Dordrecht, 1992.

[36] Birringer, R.; Gleiter, H.; Klein, H. P.; Marqardt, P. Nanocrystalline materials an approach to a novel solid structure with gas-like disorder? *Phys. Lett. A*, **102**, 365-369 (1984).

[37] Hermann, A.; Scuhmacher, E.; Wöster, L. Preparation and photoionization potentials of molecules of sodium, potassium, and mixed atoms. *J. Chem. Phys.*, **68**, 2327-2336 (1978).

[38] Wang, C. R. C.; Pollack, S.; Kappes, M. M. On the optical response of Na_{20} and its relation to computational prediction. *J.Chem. Phys.*, **94**, 2496-2501 (1991).

[39] Bonacic-Koutecký, V. Fantucci, P.; Koutecký, J. Quantum chemistry of small clusters of elements of groups Ia, Ib and IIa: fundamental concepts, predictions, and interpretation of experiments. *Chem. Rev.*, **91**, 1035-1108 (1991).

[40] Martin, T. P. *et al.* Electronic shell structure of laser-warmed Na clusters. *Chem. Phys. Lett.*, **186**, 53-57 (1991).

[41] *Metal Clusters*, Ed. W. Ekardt (Wiley, Chichester, 1999).

[42] Häkkinen, H.; Landman, U. Gold clusters (Au_N, 2< ~N< ~10) and their anions. *Phys. Rev. B.* **62**, R2287-R2290 (2000).

[43] Grönbeck, H.; Andreoni, W. Gold and platinum microclusters and their anions: comparison of structural and electronic properties. *Chem. Phys.* **262**, 1-14 (2000).

[44] Grönbeck, H.; Broqvist, P. Comparison of the bonding in Au_8 and Cu_8: A density functional theory study. *Phys. Rev. B*, **71**, 073408-073411 (2005).

[45] Olson, R. M. *et al.* Where does the planar-to-nonplanar turnover occur in small gold clusters? *J. Am. Chem. Soc.*, **127**, 1049-1052 (2004).

[46] Walker, A. V. Structure and energetics of small gold nanoclusters and their positive ions. *J. Chem. Phys.* **122**, 094310-1 - 094310-12 (2005).

[47] Furche, F. *et al.* The structures of small gold cluster anions as determined by a combination of ion mobility measurements and density functional calculations. *J. Chem. Phys.* **117**, 6982-6990 (2002).

[48] Gilb, S.; Weis, P.; Furche, F.; Ahlrihs, R.; Kappes, M. M. Structures of small gold cluster cations (Au_n^+, n<14): ion mobility measurements versus density functional calculations. *J. Chem. Phys.* **116**, 4094 - 4101 (2002).

[49] Sárkány, A.; Révay, Z. S. Some features of acetylene and 1,3-butadiene hydrogenation on Ag/SiO_2 catalysts. *Appl. Catal. A*, **243**, 347-355 (2003).

[50] Mohr, C.; Hofmeister, H.; Radnik, J.; Claus, P. Identification of active sites in gold-catalysed hydrogenation of acrolein. *J. Am. Chem. Soc.* **125**, 1905-1911 (2003).

[51] Jia, J.; Haraki, K.; Kondo, J. N.; Domen, K.; Tamaru, K. Selective hydrogenation of acetylene over Au/Al_2O_3 catalyst *J. Phys. Chem. B*, **104**, 11153-11156 (2000).

[52] Varganov, S. A.; Olson, R. M.; Gordon, M. S.; Mills. G.; Metiu, H. A study of reactions of molecular hydrogen with small gold clusters. *J. Chem. Phys.* **120**, 5169-5175 (2004).

[53] Cotton, F. A.; Wilkinson, G.; Murillo, C. A.; Bochmann, M. *Advanced Inorganic Chemistry*, 6th Ed. ;Willy: New York, 1999.

[54] Alonso, J. A. Electronic and atomic structure and magnetism of transition-metal clusters. *Chem. Rev.* **100**, 637-678 (2000).

[55] Manchot, W.; Gall. H. *Chem. Ber.* **58**, 2175 (1925).

[56] McIntosh, D.; Ozin, G. A. Synthesis of binary gold carbonyls, $Au(CO)_n$ (n = 1 or 2). Spectroscopic evidence of isocarbonyl(carbonyl)gold, a linkage isomer of bis(carbonyl)gold. *Inorg. Chem.*, **16**, 51-59 (1977).

[57] Haruta, M.; Yamada, N.; Kobayashi, T.; Iijima, S. Gold catalysts prepared by coprecipitation for low-temperature oxidation of hydrogen and of carbon monoxide. *J. Catal.*, **115**, 301-309 (1989).

[58] Haruta, M. Size- and support-dependency in the catalysis of gold. *Catal. Today*, **36**, 153-166 (1997).

[59] Grunwaldt, J. D.; Baiker, A. Gold/titania interfaces and their role in carbon monoxide oxidation. *J. Phys. Chem. B*, **103**, 1002-1012 (*1999*).

[60] Cunningham, D. A. H.; Vogel, W.; Kageyama, H.; Tsubota S.; Haruta, M. The relationship between the structure and activity of nanometer sized gold when supported on $Mg(OH)_2$. *J. Catal.*, **177**, 1-10 (1998).

[61] Jiang L.; Xu, Q. Reactions of gold atoms and small gold clusters with CO: Infrared spectroscopic and theoretical characterization of Au_nCO (n = 1-5) and $Au_n(CO)_2$ (n = 1,2) in solid argon. *J. Phys. Chem. A*, **109**, 1026-1032 (2005).

[62] Phala, N. S.; Klatt, G.; Steen, E. van. A DFT study of hydrogen and carbon monoxide chemisorption onto small gold clusters. *Chem. Phys. Lett.*, **395**, 33-37 (2004).

[63] Shi, F. G. Size dependent thermal vibrations and melting in nanocrystals. *J. Mater. Res.*, **9**, 1307-1313 (1994).

[64] Wallace, W. T.; Whetten, R. L., Coadsorption of CO and O_2 on selected gold clusters: evidence for efficient room-temperature CO_2 generation. *J. Am. Chem. Soc.*, **124**, 7499-7505 (2002).

[65] Harfenist, F. A.; Wang, Z. L.; Whetten, R. L.; Vezmar, I.; Alvarez, M. M. Three-dimensional hexagonal close-packed superlattice of passivated Ag nanocrystals. *Adv. Mater.*, **9**, 817-822 (1997).

[66] Knight, W. D. *et al.* Electronic shell structures and abundances of sodium clusters. *Phys. Rev. Lett.*, **52**, 2141-2143, **53**, 510(E) (1984)

[67] Alameddin, G. J.; Hunter, J.; Cameron, D.; Kappes, M. M. Electronic and geometric structure in silver clusters. *Chem. Phys. Lett.*, **192**, 122 -128(1992).

CHAPTER 2

Background of Electronic Structure Methods

In 1929, P. A. M. Dirac, one of the founders of Quantum Mechanics remarked,

> The fundamental laws necessary for the mathematical treatment of large parts of physics and the whole of chemistry are thus fully known, and the difficulty lies only in the fact that application of these laws leads to equations that are too complex to be solved.

This was indeed true at that time. Even today, after a lot of advancement in this field, the application of these laws to realistic problems in material science, physics and chemistry lead to equations which are not analytically solvable in all but most simple situations. Due to the efforts of a number of research groups, numerical solutions to these problems began appearing since the 1920s. But they became popular only in the 1950s after the invention of the computer. Nowadays several models based on approaches ranging from the less accurate semi-empirical to the highly accurate *ab-initio* methods are available. Development of convenient software packages and tremendous computational power has enabled the application of these theories to systems of interest like atoms, molecules, nanoclusters, solids, surfaces etc. Computer modelling is being increasingly used in other areas like climate modelling, weather forecasting, drug design, medical diagnostics, crash simulations etc.

In this chapter we shall provide a brief description of various computational methods used for electronic structure calculations including Density Functional Theory on which our calculations are mainly based.

Computational methods

Computational methods serve as a bridge between theoretical models and experimental results. They not only provide results which may be compared to experimental values, e.g. to equilibrium geometries, binding energies, vibrational frequencies or photoelectron spectra, but can also offer supplementary information not directly available from experiment. Computer simulation at the atomic level can be done by using classical mechanics while the treatment at the electronic level requires quantum mechanics. Computational methods encompass all numerical methods based on molecular mechanics, molecular dynamics, Monte Carlo and quantum mechanics. These methods are employed for obtaining qualitative and quantitative information regarding structure, electronic, magnetic and optical properties of matter, crystal lattice parameters, reactivity, surface phenomenon like chemisorption, surface reconstruction, chemical reactions and catalysis.

The computational methods used in this thesis are based on density functional theory, time-dependent density functional theory and hybrid quantum mechanics/molecular mechanics. These methods are briefly discussed below.

2.1 Molecular Mechanics

Molecular mechanics simulations are based on a mathematical model that treats molecules as a collection of balls (corresponding to atoms) held together by springs (corresponding to bonds). This is referred to as the "ball and spring" model.[1] The energy of a system for a given nuclear configuration is expressed as a parametric function of the nuclear coordinates. These parameters are fitted to experimental or higher level computational data. In molecular mechanics quantum aspects of nuclear motion are neglected and the interactions between nuclei are investigated as being due to force fields. Accuracy of the results depends on the type of force field and the reliability of the parameters used. Electrons are not treated explicitly in molecular mechanics. However, electronic effects get included in the force field through parameterizations.

The force field energy E_{FF} is expressed as a sum of various terms, each describing the energy required to distort a molecule in a specific fashion.[2]

$$E_{FF} = E_{stretch} + E_{bend} + E_{torsion} + E_{vdw} + E_{el} + E_{cross} \tag{2.1}$$

where $E_{stretch}$ is the energy function for stretching a bond between two atoms, E_{bend} represents the energy required for bending through an angle, $E_{torsion}$ is the torsional energy for rotation around a bond, E_{vdw}, the van der Waals energy and E_{el}, the electrostatic energy describe the non bonded atom-atom interactions and E_{cross} represents the coupling between the first three terms. Once the force field energy is calculated, geometries and relative energies can be determined. Stable molecules correspond to minima on the potential energy surface which can be obtained by minimizing E_{FF} as a function of nuclear coordinates.

Different force fields vary mainly in three aspects, viz, the functional form of each energy term, the number of cross terms included and the type of information used for fitting the parameters. Some of the commonly used force fields are MM2,[3] MM3,[3] CVFF,[4] CFF91,[5] AMBER,[6] MOMEC[7] and UFF.[8]

The biggest advantage of force field methods is the speed. Molecular mechanics calculations are not computationally expensive. This renders it possible to treat systems with thousands of atoms by computers of modest size. These methods are increasingly being used for molecular modelling of biological macromolecules, like proteins and DNA. In case of systems for which good parameters are available, it is possible to make good predictions of geometries and relative energies within a short time, and interconversion between conformers can also be studied. The disadvantage is that molecular mechanics provides good results only for systems for which good parameters are known. This limits the applicability of the method. It is not possible to estimate the errors involved in a certain calculation within the method. This can be done only by comparing the results with other methods or with experimental data. Moreover, this method cannot be applied to processes involving bond formation and bond breaking.

2.2 Quantum Mechanical Methods

Electrons being light particles, cannot be described even qualitatively by using classical mechanics. For describing the electronic structure of a system one has to resort to quantum mechanics. Methods which aim to solve the electronic Schrödinger equation are referred to as "electronic structure calculations". Quantum mechanical methods can be broadly classified into two categories, *ab-initio* and semiempirical methods. *Ab-initio* is a Latin word meaning "from the beginning".

These methods generate solutions to the time-independent Schrödinger equation without reference to experimental data. Hence they generate accurate results. *Ab-initio* methods include Hartree-Fock (HF), Configuration interaction (CI), Muticonfiguration and multireference methods (MCSCF), Møller-Plesset many-body perturbation theory (MBPT), Coupled cluster (CC) and Density functional theory (DFT). Accurate *ab-initio* calculations for large molecular systems are computationally very expensive. Semi-empirical methods involve a reduced form of the Hamiltonian and make use of adjustable parameters which can be fitted to experimental data. Hence they require less computational time; the results are not as accurate as in case of *ab-initio* methods. Nevertheless, they provide a good compromise between accuracy and computational expense. Some of the commonly used semiempirical methods include Hückel molecular orbital theory (HMO), INDO, NDDO, MINDO/1 etc. The following subsections briefly discuss some important quantum mechanical methods.

2.2.1 Hartree-Fock method

For accurate determination of the electronic properties of matter, one needs to solve the time-dependent Schrödinger equation. However, it is found that ground state properties are time-independent. So, stationary solutions suffice for most of our systems of interest. In order to further simplify the calculations most electronic structure methods apply the Born-Oppenheimer approximation[9] where the motion of the nuclei is neglected when calculating the electronic structure. This approximation can be justified from the fact that the mass of the nucleus is about three orders of magnitude more than that of the electrons. With these approximations the fundamental task is to solve the many-body time-independent Schrödinger equation for the electrons in the Coulomb field of the fixed nuclei

$$\hat{H}\psi_i(\vec{x}_1,\vec{x}_2,........,\vec{x}_N,\vec{R}_1,\vec{R}_2,....,\vec{R}_M) = E_i\psi_i(\vec{x}_1,\vec{x}_2,........,\vec{x}_N,\vec{R}_1,\vec{R}_2,....,\vec{R}_M) \qquad (2.2)$$

where $\hat{H}$ is the Hamiltonian operator of a molecular system consisting of M nuclei and N electrons. For a fixed set of locations R of the nuclei, the Hamiltonian $\hat{H}$ is written as

$$\hat{H}_{elec} = -\frac{1}{2}\sum_{i=1}^{N}\nabla_i^2 - \sum_{i=1}^{N}\sum_{A=1}^{M}\frac{Z_A}{r_{iA}} + \sum_{i=1}^{N}\sum_{j>i}^{N}\frac{1}{r_{ij}} \qquad (2.3)$$

The first term in equation (2.3) represents the kinetic energy of the electron i, the second term represents the attractive potential between the electron i and the nucleus A separated by a distance R_{iA} while the third term represents the repulsion between the electrons i and j separated by a distance r_{ij}. Equation (2.3) represents the electronic Hamiltonian as it does not contain the nucleus-nucleus interaction term. In most electronic structure calculations the nucleus-nucleus repulsion is not included in the Hamiltonian, but is added as a separate constant term later.

In Hartree-Fock (HF) theory the complicated N-electron wavefunction is expressed as a product of N one-electron wavefunctions $\chi_i(\vec{x}_i)$. This product is referred to as a Slater determinant Φ_{SD}.

$$\Phi_{SD} = \frac{1}{\sqrt{N!}} det\{\chi_1(\vec{x}_1)\chi_2(\vec{x}_2)......\chi_N(\vec{x}_N)\} \qquad (2.4)$$

The one electron wave functions $\chi_i(\vec{x}_i)$ are called spin orbitals. Each spin orbital consists of spatial orbital $\phi_i(\vec{r})$ and a spin function $\alpha(s)$ or $\beta(s)$.

The Slater determinant Φ_{SD} has been used as an approximation to the exact wavefunction ψ_{exact}. In order to find the best Slater determinant, that is, the one that provides the lowest energy, the variational principle is used under the restriction that the spin orbitals χ_i remain orthonormal.

$$E_{HF} = \min_{\Phi_{SD}\rightarrow N} E[\Phi_{SD}] \qquad (2.5)$$

The Hartree –Fock energy is obtained as

$$E_{HF} = \left\langle \varphi_{SD}\left|\hat{H}\right|\varphi_{SD}\right\rangle = \sum_{i}^{N}(i|\hat{h}|i) + \frac{1}{2}\sum_{i}^{N}\sum_{j}^{N}(ii|jj) - (ij|ji) \qquad (2.6)$$

where $(i|\hat{h}|i) = \int \chi_i^*(\vec{x}_1)\left\{-\frac{1}{2}\nabla^2 - \sum_{A}^{M}\frac{Z_A}{r_{1A}}\right\}\chi_i(\vec{x}_1)d\vec{x}_1 \qquad (2.7)$

defines the contribution to the kinetic energy and the electron-nucleus attraction and

$$(ii \mid jj) = \int \int \mid \chi_i(\vec{x}_1) \mid^2 \frac{1}{r_{12}} \mid \chi_j(\vec{x}_2) \mid^2 d\vec{x}_1 d\vec{x}_2 \qquad (2.8)$$

$$(ij \mid ji) = \int \int \chi_i(\vec{x}_1)\chi_j^*(\vec{x}_1) \frac{1}{r_{12}} \chi_j(\vec{x}_2)\chi_i^*(\vec{x}_2) d\vec{x}_1 d\vec{x}_2 \qquad (2.9)$$

represent the electron-electron interaction. Equations (2.8) and (2.9) are called Coulomb and exchange integrals, respectively. E_{HF} in equation (2.6) is a functional of the spin orbitals, $E_{HF} = E[\{\chi_i\}]$. Using the variational principle and varying the spin orbitals leads to the Hartree Fock equations

$$\hat{f}_i \chi_i = \varepsilon_i \chi_i \quad , i = 1,2,3,\dots,N \qquad (2.10)$$

This is a set of N eigenvalue equations. ε_i are the Langrange multipliers, which gives the eigenvalues of the Fock operator $\hat{f}_i$. ε_i have the interpretation of molecular orbital (MO) energies. $\hat{f}_i$ is an effective one-electron operator defined as

$$\hat{f} = -\frac{1}{2}\nabla_i^2 - \sum_A^M \frac{Z_A}{r_{iA}} + V_{HF}(i) \qquad (2.11)$$

The first two terms in the above equation describe the kinetic energy of the ith electron and its potential energy due to the presence of the nucleus A, respectively, while the third term $V_{HF}(i)$, the *Hartree-Fock potential*, gives the potential energy of the ith electron due to the presence of the other N-1 electrons. The complicated electron-electron repulsion term $1/r_{ij}$ of the Hamiltonian is replaced by the one electron term $V_{HF}(i)$ by treating the electron-electron repulsion in an average way. Thus in Hartree-Fock theory each electron is considered to be moving in the field of the nucleus and the average field of the other $n-1$ electrons.

As the Fock operator depends through the Hartree Fock potential on the spin orbitals, i.e, on the solution of the eigenvalue problem that needs to be solved, equation (2.10) represents a pseudo eigenvalue problem and needs to be solved iteratively through the self-consistent field (SCF) procedure. The solution begins with a guessed set of orbitals with which the Hartree Fock equations are solved. The resulting new set of orbitals is then used in the next iteration and so on until the input and output orbitals vary by less than a predetermined value.

Electron Correlation

In Hartree-Fock theory, the many-electron wavefunction is approximated as a single Slater determinant. This is not a good approximation and so the energy obtained is not the exact ground state energy of the system. According to the variational principle, this energy is greater than the ground state energy E_0. The difference between the exact ground state energy E_0 and the Hartree Fock energy E_{HF} is called correlation energy. It is a negative quantity.

$$E_C^{HF} = E_0 - E_{HF} \qquad (2.12)$$

As the number of basis functions increases the accuracy of the MOs become better. In the limit of a complete basis set (infinite number of basis functions) the results become similar to those obtained by numerical Hartree Fock methods. This is the best solution to the Schrödinger equation that can be obtained by a single determinant wave function and is known as the Hartree Fock limit. This limit can never be reached in actual practice.

2.2.2 Density Functional Theory

Density functional theory (DFT) is an *ab-initio* method used for determining the ground state of atoms, molecules and solids. Solving the many-electron Schrödinger equation for such systems by the traditional wave-function based methods presents a formidable task as the wavefunction is a function of 3N spatial coordinates and N spin coordinates, N being the number of electrons in the system. The central quantity in DFT is the electron density $\rho(\vec{r})$ which is a function of three spatial coordinates only irrespective of the size of the system. So the calculations are much simpler. Once the electron density is known, the external potential, and consequently the Hamiltonian of the system can in principle be uniquely determined. The knowledge of Hamiltonian in its turn leads to the determination of the total electronic wavefunction. Consequently, every quantum mechanical observable is a functional of the ground-state density.

DFT which includes electron correlation, provides a very good compromise between the accuracy of the results and the computational expenses involved. The popularity of density functional theory can be gauged from the increasing number of publications using DFT based methods as depicted in Figure 2.1.

Citations In Each Year
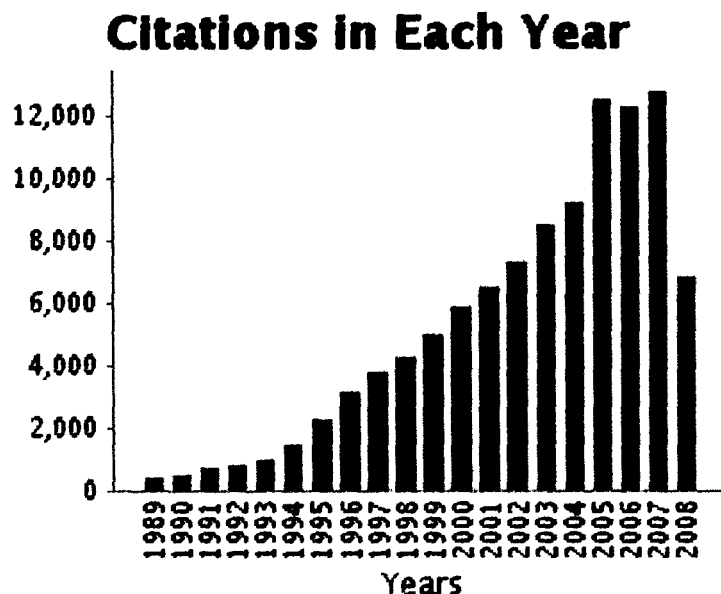
Figure 2.1 Number of publications per year where the phrase "density functional theory" appears in the title or abstract for the period 1989-2008. (taken from ISI Web of Science).

The development of density functional theory began in the mid-sixties through the efforts of Hohenberg and Kohn[10] and later by Kohn and Sham[11] although early attempts in this direction were made by Thomas[12] and Fermi.[13] Walter Kohn was awarded the nobel prize in Chemistry in 1998 for his work on DFT alongwith John Pople.

The electronic one-particle density is obtained from the wavefunction by quadrature

$$\rho(\vec{r}) = N \int \dots \int \left| \psi(\vec{x}_1, \vec{x}_2, \dots, \vec{x}_N) \right|^2 ds_1 d\vec{x}_2 \dots dx_N \qquad (2.13)$$

$\rho(\vec{r})$ determines the probability of finding any of the N electrons within a volume element $d\vec{r}_1$ with arbitrary spin while the other N-1 electrons have arbitrary positions and arbitrary spin in the state represented by ψ. $\rho(\vec{r})$ is a non-negative function which vanishes at infinity and integrates to the total number of electrons.

$$\rho(\vec{r} \rightarrow \infty) = 0 \qquad (2.14)$$

$$\int \rho(\vec{r}) d\vec{r}_1 = N \qquad (2.15)$$

Unlike the wavefunction the electron density is an observable and can be determined experimentally, for example, by x-ray diffraction.[14]

The theoretical formulation of density functional theory is based on the Hohenberg-Kohn theorems. The first Hohenberg-Kohn (HK) theorem states that two N-electron systems with different external potentials cannot have the same electron density $\rho(\vec{r})$. Thus the ground state electron density $\rho(\vec{r})$ gives the external potential upto a constant and determines the Hamiltonian of the multi-particle Schrödinger equation, i.e, the density $\rho(\vec{r})$ completely describes the electronic system.

The total electronic energy of the system and all its contributions are expressed as functionals of the electron density $\rho(\vec{r})$.

$$E = E[\rho(r)] = T[\rho(r)] + E_{Ne}[\rho(r)] + E_{ee}[\rho(r)] \qquad (2.16)$$

where T is the kinetic energy of all the electrons, E_{Ne} is their potential energy due to the nuclei and other possible external potentials, E_{ee} is the electron-electron interaction which consists of the classical Coulomb term and other non-classical terms.

Equation (2.16) may be separated out into terms that are system dependent, that is, the potential energy due to electron nucleus attraction, $E_{Ne}[\rho(r)] = \int \rho(\vec{r})V_{Ne}d\vec{r}$ and the rest which are system independent. Collecting the system independent terms into a new functional, the Hohenberg-Kohn functional $F_{HK}[\rho]$ we arrive at

$$E[\rho] = \int \rho(\vec{r})V_{Ne}d\vec{r} + F_{HK}[\rho] \qquad (2.17)$$

where

$$F_{HK}[\rho] = T[\rho(r)] + E_{ee}[\rho(r)] \qquad (2.18)$$

The functional forms of both the terms in $F_{HK}[\rho]$ are unknown. The second Hohenberg-Kohn theorem enunciates a variational principle for the electron density. This theorem states that $F_{HK}[\rho]$, the functional that delivers the ground state energy of the system provides the lowest energy if and only if the input density is the ground state density ρ_0. Thus this theorem provides a starting point for implementing the promises made by the first HK theorem. However, as no analytical expressions for $F_{HK}[\rho]$ are known, implementation of HK theorems is not an easy task. A straight-forward approach to calculating the electronic density

directly from the external potential was attempted in the Thomas-Fermi theory,[15] but its application to chemical problems fails to provide the necessary accuracy.

2.2.2.1 Kohn-Sham Method

The Kohn-Sham approach[11] to density functional theory introduces a non-interacting reference system whose wave-function ϕ_{KS} is a Slater determinant composed of one-particle orbitals ϕ_i and whose ground state density is identical to the ground state density of the real system.

The DFT expression for the total energy equation (2.16) is reformulated in Kohn-Sham (KS) theory by introducing the kinetic energy of the non-interacting reference system $T_s[\rho]$. From the electron-electron interaction energy a term $J[\rho]$ is extracted which describes the classical Coulomb energy of the charge density $\rho(\vec{r})$. The remaining term of the electron-electron interaction E_{xc}, termed as the exchange-correlation energy contains the difference between the kinetic energy of the interacting and non-interacting systems.

$$E[\rho(r)] = E_{Ne}[\rho(r)] + T_s[\rho(r)] + J[\rho(r)] + E_{xc}[\rho(r)] \qquad (2.19)$$

The classical Coulomb energy $J[\rho(r)]$ of a charge density $\rho(\vec{r})$ is

$$J[\rho(r)] = \frac{1}{2}\iint \frac{\rho(\vec{r})\rho(\vec{r}')}{|\vec{r}-\vec{r}'|} d\vec{r} d\vec{r}' \qquad (2.20)$$

The exchange-correlation energy is defined as

$$E_{xc}[\rho(r)] = T[\rho(r)] - T_s[\rho(r)] + E_{ee}[\rho(r)] - J[\rho(r)] \qquad (2.21)$$

In general, the exchange-correlation energy, which is a functional of energy density $\rho(\vec{r})$ is not known except for the most simple case of a homogeneous electron gas. The kinetic energy of the non-interacting reference system is expressed as

$$T_S = -\frac{1}{2}\sum_i^N \langle \phi_i | \nabla^2 | \phi_i \rangle \qquad (2.22)$$

where ϕ_i are the Kohn-Sham orbitals which satisfy the Kohn-Sham equation

$$\hat{h}_{KS}\phi_i = \varepsilon_i \phi_i \qquad (2.23)$$

where

$$\hat{h}_{KS} = -\frac{1}{2}\nabla^2 + V_{eff}(\vec{r}), \qquad V_{eff} = V_{Ne}(r) + \int \frac{\rho(r')}{|r - r'|} dr' + V_{XC}(r) \qquad (2.24)$$

where V_{XC} is the functional derivative of E_{XC} with respect to ρ.

$$V_{XC}[\rho] = \frac{\delta E_{XC}[\rho]}{\delta \rho} \qquad (2.25)$$

The KS orbitals ϕ_i can be expressed as a linear combination of a set of functions known as basis functions χ_μ as

$$\phi_i = \sum_\mu C_{\mu i} \chi_\mu \qquad (2.26)$$

The electron density ρ is related to the KS orbital by

$$\rho(r) = \sum_{i=1}^{n} |\phi_i(r)|^2 \qquad (2.27)$$

The exact form of the exchange-correlation energy E_{XC} as a functional of ρ is not known. However, several approximations to E_{XC} exist. The Kohn-Sham equations are solved iteratively by the SCF procedure as in the Hartree Fock method.

2.2.2.2 Energy Functionals

A) *The Local Density Approximation (LDA)*

This model forms the basis of all exchange-correlation energy functionals. This model is based on a hypothetical uniform electron gas in which the electrons are believed to be moving in a positive charge background, such that the system as a whole is electrically neutral. The number of electrons and the volume V are considered to approach infinity while the electron density remains constant. Physically, this model represents an idealized metal consisting of positive cores and valence electrons.

In this model the exchange-correlation energy is expressed as

$$E_{XC}^{LDA}[\rho] = \int \rho(\vec{r}) \varepsilon_{XC}(\rho(\vec{r})) d\vec{r} \qquad (2.28)$$

Here, $\varepsilon_{XC}\rho(\vec{r})$ is the exchange-correlation energy per particle of an uniform electron gas of density $\rho(\vec{r})$. Thus in LDA the exchange-correlation energy

depends on the electron density ρ only. The quantity $E_{xc}^{LDA}[\rho]$ can be split into exchange and correlation contributions,

$$\varepsilon_{xc}(\rho(\vec{r})) = \varepsilon_{x}(\rho(\vec{r})) + \varepsilon_{c}(\rho(\vec{r}))$$

(2.29)

The exchange part ε_{x}, which represents the exchange energy of an electron in a uniform electron gas of a particular density, was originally derived by Bloch and Dirac[16] in the 1920s.

$$\varepsilon_{x} = -\frac{3}{4}\left(\frac{3\rho(\vec{r})}{\pi}\right)^{1/3}$$

(2.30)

The exchange functional (2.30), is apart from the pre-factor equal to the form found by Slater in his approximation to the Hartree-Fock exchange and is known as Slater exchange, abbreviated as S. No such explicit expression for the correlation part ε_{c} is known. However, highly accurate numerical quantum Monte-Carlo simulations of the homogenous electron gas are available. Based on these results several authors have presented analytical expressions for ε_{c}. The most widely used representations for ε_{c} include those of Vosko, Wilk and Nussair (VWN),[17] and that of Perdew and Wang (PW).[18,19]

Introducing electron spin into LDA results in the local spin density approximation (LSDA).

B) The Generalised Gradient Approximation (GGA)

In generalized gradient approximation (GGA) the exchange correlation energy depends not only on the electron density $\rho(\vec{r})$ at a particular point $\vec{r}$ but also on the gradient of the charge density $\nabla\rho(\vec{r})$. The dependence on the gradient of density is believed to account for the non-homogeneity of the true electron density. In this model the exchange correlation energy reads as

$$E_{xc}^{GGA}[\rho] = \int \rho(\vec{r})\varepsilon_{xc}(\rho, \nabla\rho)d\vec{r}$$

(2.31)

Prominent examples of GGA functionals include those by Perdew and Wang,[20] by Perdew, Burke and Ernzerhof (PBE)[21] and Becke's formula[22] for the exchange part with Perdew's 1986 formula for correlation.[9] Becke's exchange when combined with the correlation functional given by Lee, Yang and Parr[23] yields the BLYP functional.

C) Hybrid Functional

It is found that the exchange contributions are significantly larger than the correlation contributions.[14] So the accuracy of the results of DFT calculations depends a lot on the expression for the exchange functional used. In case of hybrid functionals Hartree-Fock exchange is coupled with LDA and GGA exchange correlation functionals. This provides a better description of the exchange term and leads to improved results. A commonly used hybrid functional is the B3LYP functional. The expression for this functional is given by

$$E_{xc}^{B3LYP} = 0.8\,E_x^{LDA} + 0.2E_x^{HF} + 0.72E_x^{B88} + 0.81E_c^{LYP} + 0.19E_c^{VWN} \tag{2.32}$$

2.2.3. Basis Sets

A basis set is a set of mathematical functions used to approximate molecular orbitals of a system. The molecular orbitals are obtained as a linear combination of atomic orbitals or basis functions (equation 2.26) centred at each atomic nucleus within the system. There are two main kinds of basis functions used in electronic structure calculations.

A) Slater Type Orbitals (STO)

John C. Slater was the first to introduce the idea of basis functions in 1930.[24] The basis functions given by him are known as Slater type orbitals. They have the following functional form

$$f^{STO}(r) = \left(\frac{\xi^3}{\pi}\right)^{0.5} exp\left(-\xi r\right) \tag{2.33}$$

These basis functions correctly model the electron density in the valence region, but the electron density in the region near the nucleus is not represented very well. Also, the evaluation of the integrals is tedious. This difficulty was overcome by Frank Boys who suggested that the STOs can be approximated as linear combination of GTOs, the overlap and other integrals being easier to calculate with Gaussian basis functions.

B) Gaussian Type Orbitals (GTO)

The GTOs have the advantage that they require much less computational time compared to the STOs. A GTO has the following functional form

$$f^{GTO}(r) = \left(\frac{2\alpha}{\pi}\right)^{0.5} exp\left(-\alpha r^2\right)$$

(2.34)

The use of Gaussian basis functions enables the complicated four-centre integrals to be reduced to two-centre integrals. So the computational efficiency is high.

Classification of basis sets

Having decided on the type of basis function (STO/GTO), the most important factor is the number of functions to be used. The accuracy of the results depends upon the number of basis functions used. A short description of different types of basis sets are given below.

1) Minimal basis set

This contains the smallest number of basis functions. Only one basis function (STO, GTO or linear combination of GTOs) is employed for each atomic orbital in the atom. Example- STO-3G.

2) Double-zeta, Triple-zeta and Quadruple-zeta basis sets

The double-zeta (DZ) basis set treats each orbital separately as the sum of two STOs with different zeta (ξ) values in equation (2.33). The different ξ values represent different sizes of the orbitals, the linear combination of which gives the atomic orbital. The triple-zeta (TZ) and quadruple-zeta (QZ) basis sets are similar to that of DZ, except that they use three and four STOs instead of the two used in DZ.

3) Split-valence basis sets

As it is only the valence electrons that take part in the bonding, computational expenses can be reduced by using more than one basis function for the valence electrons and only one basis function (which can be a linear combination of some Gaussian type of functions) for the core electrons. Such a basis set is known as split-valence basis set. For example, the basis set 3-21G consists of one basis function (which is a linear combination of three Gaussian type functions) for

each atomic orbital to describe the inner shell. Two basis function per atomic orbital are used to describe the valence electrons. Of these, one is a linear combination of two Gaussian type functions, while the second consists of one Gaussian function only.

4) Polarization functions

For a better description of chemical bonding it becomes necessary to include higher angular momentum functions than those occupied in the atom in the basis sets. Such functions are called polarization functions. For example, the bonding involving a hydrogen atom can be better described by adding p-functions to the s-functions of hydrogen. One asterisk (*) at the end of a basis set denotes that polarization has been taken into account in p orbitals. Examples: 3-21G* and 6-31G*. Two asterisks (**) means that polarization has taken into account in s orbitals in addition to p orbitals. Examples: 3-21G** and 6-31G**.

5) Diffuse functions

Diffuse functions are basis functions with a larger spatial extent than the normal ones, which are particularly important for modelling lone pairs, anions, excited states etc. Diffuse basis sets are represented by the '+' or 'aug'. One '+' means that diffuse functions are being used for elements having p or higher occupied orbitals, while '++' means that diffuse functions are being used for both heavy and light elements.

6) Numerical basis sets

In this kind of basis set realized within the DMol^3 program,[25] the basis functions are given numerically as values on an atomic-centred spherical-polar mesh, rather than as analytic functions. These basis functions are generated by numerically solving the atomic KS equations with the corresponding approximate exchange-correlation functional. Because of the better quality of the atomic orbitals, basis set superposition errors are minimized and an excellent description of even weak bonds are possible.

7) Effective Core Potentials (ECP) basis sets

These basis sets are used for heavy elements. Heavy elements (3rd row or higher in the periodic table) contain a large number of core electrons and hence require a large number of basis functions for their description. Relativistic effects in the heavier elements further complicate the treatment. This problem can be simplified by introducing the effective core potential (ECP), also called pseudopotential to represent the core electrons. The core electrons are modelled by a suitable function and only the valence electrons are treated explicitly. In many cases ECP is found to give good results at a fraction of the computational cost of all electron calculations.

Figure 2.2 depicts the relationship between basis sets and accuracy. As we move fron left to right, electron correlation effects get included. On moving from bottom to top we are improving the basis sets. For an accurate description of the system both these factors, namely, the method, and the basis set, must be taken into account.

Basis
complete |—+ Exact HF   + Exact solution

Minimal   HF   Full CI
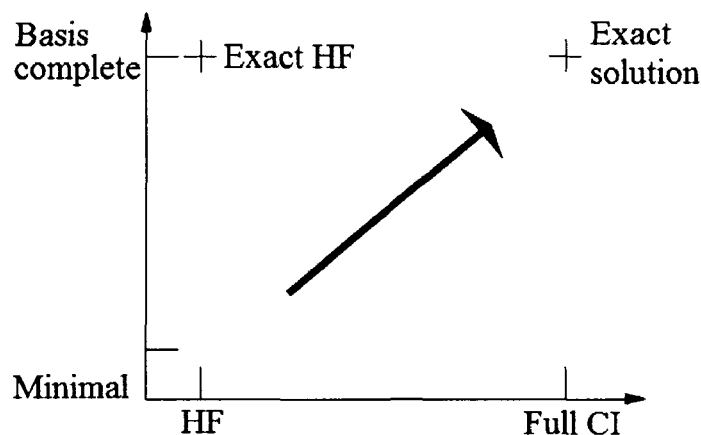
Figure 2.2 Various basis sets with different computational methods leading to the exact solution of Schrödinger equation.

2.2.4 Time-Dependent Density Functional Theory (TDDFT)

Time-dependent density functional theory (TDDFT) is the natural extension to the time domain of ordinary Density Functional Theory (DFT). While the main scope of DFT is the description of ground state properties of a system at equilibrium, the extension to the time domain grants access to its excited state and non-equilibrium properties. Unlike DFT, in TDDFT the electron density is a function of

spatial coordinates and time. The time dependent density determines the time-dependent external potential and hence all physical observables. TDDFT is based on Runge Gross theorem.[26] The starting point is the time-dependent Schrödinger equation.

$$\hat{H}(t)\psi(t) = i\frac{\partial}{\partial t}\psi(t)$$ (2.35)

The Hamiltonian consists of the kinetic energy $\hat{T}$, the Coulomb interaction $\hat{W}$ and the time-dependent external potential $\hat{V}(t)$

$$\hat{H}(t) = \hat{T} + \hat{W} + \hat{V}(t)$$ (2.36)

The external potential $\hat{V}(t)$ may contain several time dependent external potentials, each of which should be expandable in a Taylor series about the finite time t_0.[27] The essence of the Runge Gross theorem is that the time-dependent electron densities $\rho(r,t)$ and $\rho'(r,t)$ of two systems evolving from the same initial state $\psi(t_0)$ under the influence of two scalar potentials $V(r,t)$ and $V'(r,t)$ are not identical. Thus the time-dependent density determines the external potential upto an additive time-dependent function. The external potential on the other hand uniquely determines the time-dependent wavefunction which can therefore be considered as a functional of the time-dependent density.

$$\psi(t) = \psi[\rho](t)$$ (2.37)

where $\psi[\rho]$ is unique upto a time-dependent phase factor. As a result the expectation value of any quantum mechanical operator $O[\rho](t)$ is a unique functional of the density.[28]

$$O[\rho](t) = \langle \psi[\rho](t)|\hat{O}(t)|\psi[\rho](t)\rangle$$ (2.38)

TDDFT being the time-dependent counterpart of DFT, requires the time-dependent Kohn-Sham equations.

$$\hat{h}_{KS}(t)\phi_i(r,t) = \varepsilon_i\phi_i(r,t)$$ (2.39)

$$i\frac{\partial}{\partial t}\phi_i(r,t) = \left(-\frac{1}{2}\nabla^2 + V_{KS}[\rho](r,t)\right)\phi_i(r,t)$$ (2.40)

with the density obtained from the non interacting orbitals

$$\rho(r,t) = \sum_{i=1}^{N} n_i|\phi_i(r,t)|^2$$ (2.41)

The potential $V_{KS}(r,t)$ is usually called the time-dependent KS potential and is written as

$$V_{KS}[\rho](r,t) = V_{ext}(r,t) + \int \frac{\rho(r',t)}{|r-r'|} d^3r' + V_{XC}(r,t) \qquad (2.42)$$

where $V_{ext}(r,t)$ is the external potential and $V_{XC}(r,t)$ is the time-dependent exchange correlation potential which is unknown and has to be approximated for practical applications.

The functional derivative of the time-dependent potential $V_{XC}(r,t)$ with respect to the time-dependent electron density $\rho(r,t)$ is called the exchange-correlation kernel denoted by f_{xc}.

$$f_{xc}(r,t;r',t') = \frac{\partial V_{XC}(r,t)}{\partial \rho(r',t')} \qquad (2.43)$$

Given some approximations for the exchange-correlation kernel, the time-dependent Kohn-Sham equations can be solved, providing a self-consistent scheme for calculating the first order time-dependent density response.

2.3 Quantum Mechanics/Molecular Mechanics (QM/MM) Methods

The increasing computational cost with increasing size of the system hinders the use of *ab-initio* methods for treatment of large systems. A solution to this problem is obtained by restricting the quantum mechanical treatment to the 'active region' only where the bond breaking/bond formation, adsorption etc. takes place and treating the rest of the system by parameterized inter atomic potential functions. Such an approach is known as hybrid quantum mechanics-molecular mechanics (QM/MM) method. The term 'molecular mechanics' stresses the force field type of interatomic functions like MM2,[3] CFF91,[5] CHARMM,[29] UFF[8] etc.

Three papers by Warshel and Levitt,[30] Singh and Kollman,[31] and Field, Bash and Karplus[32] are usually credited with having introduced QM/MM methods. The QM-MM approach divides the energy of the whole system S into the QM energy of the active or inner part I, the MM energy of the outer part (environment), O, and an interaction term I-O (Figure 2.3).[33]

$$E_{QM-MM}(S) = E_{QM}(I) + E_{MM}(O) + E(I-O) \qquad (2.44)$$

The interaction term is either given by the potential function (MM method), or parts of it, the electrostatic interaction and sometimes the polarization of I by O, are described by the QM method. In the latter case, the potential due to point charges of the outer part is simply added to the core part of the Hamiltonian.
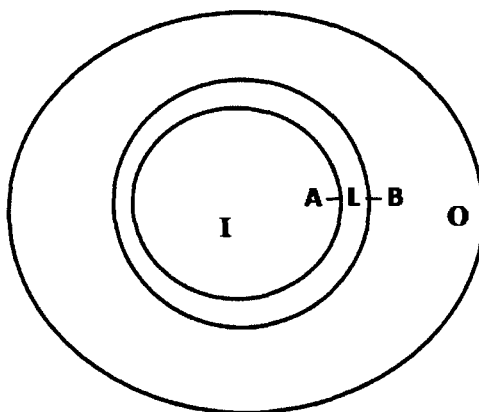
Figure 2.3 Chemical system consisting of an active (inner) part I and an outer part O. A–B is a bond which is broken on separating the system into I and O parts. L is the link atom used to saturate the inner part for QM calculations.

For most practical applications separation of the system into QM and MM region requires the cutting of bonds. In most hybrid methods the dangling bonds are saturated by link atoms or capping atoms, L and the QM calculations are performed for a cluster C, consisting of the active part and the link atom, C = I+L. However, the contributions of the link atoms cannot be evaluated separately, not even for MM energy and leads to complications. A subtraction scheme[34,35] is provided as a solution to this problem.

$$E_{QM\ MM}(S,L) = E_{QM}(C) + E_{MM}(S) - E_{MM}(C)$$ (2.45)

Morokuma and co-workers[36-38,39] developed the hybrid QM/MM method ONIOM (Our-own-N-layered Integrated molecular Orbital + molecular Mechanics) which is implemented within the program *Gaussian03*. The expression for the total energy of the whole system within the ONIOM methodology can be written as

$$E_{ONIOM2} = E_{Low}^{Real} + (E_{High}^{Model} - E_{Low}^{Model})$$ (2.46)

In this case the system has been divided into two regions. Here *high* denotes a high level computational method (the QM method in QM/MM) and *low* a lower level

method (the MM method in QM/MM), *real* and *model* refer to the full system and the QM region, respectively. The scheme can be extended to three or multiple layers.

Quantum Mechanics-Molecular Mechanics (QM/MM) methods have been used by several groups to study properties of large systems like zeolites, for adsorption studies on metal oxide surfaces, organometallic reactions and homogeneous catalysis, structure, reactivity and bond energies of large organic molecules including fullerenes, nanotubes and biomolecular structure and enzymatic reaction mechanisms.

In the present thesis we have performed DFT based QM and QM/MM calculations on gas phase and zeolite supported gold clusters using the program packages *DMol³* and *Gaussian03* and TDDFT calculations on coinage metal dimers adsorbed on the MgO(001) surface by using the program *ParaGauss*. The results of our investigations are presented in the following chapters.

References

[1] Dinur, U.; Hagler, A. T.; *Rev. Comput. Chem.*, **2**, 99-164 (1991); Burkert, U.; Allinger, N. L.; *Molecular Mechanics*, ACS Monograph, 1982; Rappe, A. K.; Casewit, C. J.; *Molecular Mechanics Across Chemistry*, University Science Books, 1997.

[2] Jensen, F. *Introduction to Computational Chemistry*, John Wiley & Sons, 1999.

[3] Burkert, U.; Allinger, N. L. *Molecular Mechanics*; American Chemical Society: Washington, DC, 1982

[4] Lifson. S.; Hagler, A. T.; Dauber, P. Consistent force field studies of intermolecular forces in hydrogen-bonded crystals. 1.Carboxylic acids, amides and the c:o.cntdot..cntdot..cntdot.H-hydrogen bonds. *J. Am. Chem. Soc.* **101**, 5111-5122 (1979).

[5] Hwang, H. J.; Stochfisch, T. P.; Hagler, A. T. Derivation of class II force fields.2. Derivation and characterization of a class II force field, CFF93, for the alkyl functional group and alkane, molecules. *J. Am. Chem. Soc.*, **116**, 2515-1525 (1994).

[6] Cornell, W. D. *et al.* A second generation force field for the simulation of proteins, nucleic acids, and organic molecules. *J. Am. Chem. Soc.* **117**, 5179-5197 (1995).

[7] Comba, P.; Hambley, T. W. *Molecular modelling of inorganic compounds*, VCH, 1995.

[8] Rappé, E.; Casewit, C. J.; Colwell, K. S.; Goddard III, W. A.; Skiff, W. M. UFF, a full periodic table force field for molecular mechanics and molecular dynamics simulations. *J. Am. Chem. Soc.*, **114 (25)**, 10024-10035 (1992).

[9] Perdew, J. P.; Density-functional approximation for the correlation energy of the inhomogeneous electron gas. *Phys. Rev. B*, **33**, 8822-8824 (1986).

[10] Hohenberg, P.; Kohn, W. Inhomogeneous electron gas. *Phys. Rev.*, **136**, B864-B871 (1964).

[11] Kohn, W.; Sham, L. J. Self-consistent equations including exchange and correlation effects. *Phys. Rev.*, **140**, A1133-A1138 (1965).

[12] Thomas, L. H. The calculation of atomic fields. *Proc. Camb. Phil. Soc.*, **23**, 542-548 (1927).

[13] Fermi, E. Eine statistische methode zur bestimmung einiger eigenschaften des atoms und ihre anwendung auf die theorie des periodischen systems der elemente. *Z. Phys.*, **48**, 73 (1928).

[14] Koch, W.; Holthausen, M. C. *A Chemist's Guide to Density Functional Theory*, WILEY-VCH, Weinheim, Germany, second edition, (2000).

[15] Lieb, E. H. Thomas-Fermi and related theories of atoms and molecules. *Rev. Mod. Phys.*, **53**, 603-641 (1981).

[16] Dirac, P. A. M. Note on exchange phenomenon in the Thomas atom. *Proc. Camb. Phil. Soc.*, **26**, 376-385 (1930).

[17] Vosko, S. J.; Wilk, L.; Nusair, M. Accurate spin-dependent electron liquid correlation energies for local spin density calculations: a critical analysis. *Can. J. Phys.*, **58**, 1200-1211 (1980).

[18] Perdew, J. P. in *Electronic Structure of Solids '91*, Ed. Ziesche, P. and Eschrig, H. Akademie Verlag, Berlin, (1991).

[19] Perdew, J. P. *et al.* Atoms, molecules, solids and surfaces: applications of the generalized gradient approximation for exchange and correlation. *Phys. Rev. B*, **46**, 6671-6687 (1992).

[20] Wang, Y. Generalized gradient approximation for the exchange-correlation hole of a many-electron system. *Phys. Rev. B*, **54**, 16533-16539 (1996).

[21] Perdew, J. P.; Burke, K.; Ernzerhof, M. Generalized gradient approximation made simple. *Phys. Rev. Lett.* **77**, 3865-3868 (1996).

[22] Becke, A. D. Density-functional exchange-energy approximation with correct asymptotic behavior. *Phys. Rev. A.*, **38**, 3098-3100 (1988).

[23] Lee, C.; Yang, W.; Parr, R. G. Development of the Colle-Salvetti correlation-energy formula into a functional of the electron density. *Phys. Rev. B*, **37**, 785-789 (1988).

[24] Slater, J. C. Atomic shielding constants. *Phys. Rev.* **36**, 57-64 (1930).

[25] Delly, B. An all-electron numerical method for solving the local density functional for polyatomic molecules. *J. Chem. Phys.*, **92**, 508-517 (1990).

[26] Runge, E.; Gross, E. K. U. Density-functional theory for time-dependent systems. *Phys. Rev. Lett.* **52**, 997-1000 (1984).

[27] Nardelli. A. *Ph. D. Thesis*, University of Trieste, 2008.

[28] Gross, E. K. U.; Kohn, W. in *Adv. Quantum Chem.* Vol. **21** Ed. Trickey, S. B. Academic, San Diego, 1990.

[29] Brooks, B. R. *et al.* Charm: A program for macromolecular energy, minimization, and dynamics calculations. *J Comput. Chem* **4**, 187-217 (1983).

[30] Warshel, A.; Levitt, M. Theoretical studies of enzymatic reactions: dielectric, electrostatic and steric stabilization of the carbonium ion in the reaction of lysosyme. *J. Mol. Biol.*, **103**, 227-249 (1976).

[31] Singh, U. C.; Lomman, P. A.; A combined *ab-initio* quantum-mechanical and molecular-mechanical method for carrying out simulations for complex molecular systems- applications to the $CH_3Cl^+Cl^-$ exchange-reaction and gas-phase protonation of polyethers. *J. Comp. Chem.*, **7**, 718-730 (1986).

[32] Field, M. J.; Bash, P.A.; Karplus, M. A combined quantum-mechanical and molecular-mechanical potential for molecular-dynamics simulations. *J. Comp. Chem.*, **11**, 700-733 (1990).

[33] Sauer, J.; Sierka, M. Combining quantum mechanics and interatomic potential functions in *ab initio* studies of extended systems. *J. Comp. Chem.* **21**, 1470-1493 (2000).

[34] Kömel, C. M.; Sauer, J. SOLIDS_EMBED Program Version1.0 in Catalysis Release 3.0; BIOSYM Technologies, Inc.: San Diego, CA, 1994.

[35] Eichler, U.; Kömel, C. M.; Sauer, J. Combining *ab initio* techniques with analytical potential functions for structure predictions of large systems: Method and application to crystalline silica polymorphs. *J Comp. Chem* **18**, 463-477 (1997).

[36] Dapprich, S.; Komaromi, I.; Byun, K. S.; Morokuma, K.; Frisch, M. J. A new ONIOM implementation in Gaussian98. Part I. The calculation of energies, gradients, vibrational frequencies and electric field derivatives. *J. Mol. Struct. THEOCHEM* **461-462**, 1-21 (1999).

[37] Svensson, M.; Humbel, S.; Morokuma, K. Energetics using the single point IMOMO (integrated molecular orbital + molecular orbital) calculations: choices of computational levels and model systems. *J Chem. Phys.* **105**, 3654-3661 (1996).

[38] P. B. Karadakov and K. Morokuma, *Chem. Phys. Lett.* ONIOM as an efficient tool for calculating NMR chemical shielding constants in large molecules. **317**, 589-596 (2000).

[39] Vreven, T.; Morokuma, K. On the application of the IMOMO (integrated molecular orbital + molecular orbital) method. *J. Comput. Chem.* **21**, 1419-1432 (2000).

CHAPTER 3

Density Functional Studies on Gas Phase Nanoclusters of Gold

In this chapter we present a detailed and systematic investigation of the isomers of small gas phase gold clusters Au_n (n = 2-13), elucidating their geometric and electronic properties using density functional theory. This study is based on an unconstrained geometry optimization with all electron scalar relativistic method. We have been able to identify fifty eight structures of neutral gold clusters in the entire size range, out of which twelve are novel structures. Vibrational frequency calculations have been performed to verify that all the structures are minima on the potential energy surface. The minimum energy structure for each cluster size is found to be planar. Electronic properties like HOMO-LUMO gap, chemical hardness, second difference of binding energy and fragmentation energy are found to exhibit odd-even alternations indicating that even numbered clusters are more stable than the odd numbered ones. This study is extended to singly charged cationic and anionic gold clusters in the same size range.

3.1 Introduction

The physical and chemical properties of gold nanoclusters are found to have a marked dependence on their physical structures. So, significant efforts have been made to determine the most stable configurations of gold clusters in the nano size range. Before developing any practical applications, it is important to understand the chemical, thermodynamic, electronic and optical properties of the nanoclusters. Apart from the most stable cluster isomers, other possible low-energy structures

must also be investigated. Unfortunately, direct and comprehensive experimental information of smaller gold clusters is difficult to acquire. Therefore, smaller gold clusters have been theoretically investigated using various computational methods over the past few years. [1-17] Most of these studies have shown that neutral and charged gold clusters favor two-dimensional (2D) structures to unusually large sizes while few of them have found the lowest energy structure to be three-dimensional (3D). The occurrence of planar gas-phase clusters with large cluster sizes is attributed to the strong relativistic bonding effects in gold that reduce the s-d energy gap thus inducing hybridization of the atomic $5d$-$6s$ orbitals which cause an overlap of the $5d$ shells of neighboring atoms in the cluster. [2]

Rösch and coworkers[8] have investigated a series of gold clusters in the size range from Au_6 to Au_{147} using scalar-relativistic all-electron density functional theory. They analyzed the convergence of cluster properties towards the bulk limit and compared the results obtained by LDA and GGA exchange correlation functionals. Häkkinen and Landman[1] have investigated the low-energy structures of gold clusters and their anions for n = 2 to 10 atoms using density functional theory employing scalar relativistic pseudopotentials for the $5d^{10}6s^1$ valence electrons of gold and a generalized gradient approximation (GGA). They located the planar to 3D transition for neutral clusters at n = 7. They also compared their DFT based electronic structure calculations of small gold cluster anions with experimental photoelectron spectroscopy (PES) data. [2] Walker[4] performed DFT calculations to determine the optimized geometries of neutral Au_n (n = 2-11) and cationic Au_n^+ (n = 2-9) clusters and found that the 2D-to-3D transition for neutral clusters occurs at Au_{11}. Furche et $al.$[6] performed a combined experimental and theoretical study of gold cluster anions for n<13. The experimental study consisted of ion mobility experiments and the theoretical study was done by using ab $initio$ molecular dynamics. By comparing theoretical and experimental results, they assigned structures for the gold cluster anions and located the transition from two-dimensional to three-dimensional cluster to occur at n = 12. While several ab $initio$ calculations on gold nanoclusters in the past have been limited by symmetry constraints,[7,8] an unconstrained global minima search[9] is necessary for locating all possible low-energy isomers. Considerable progress has been made towards this goal by Garzón et $al.$[10] and Soler et $al.$[18] who predicted amorphous structures for the most stable isomers of intermediate size Au_n (n = 38,55,75) nanoclusters based on an

exhaustive minima search using generic optimization methods that employed classical Gupta n-body potentials. Similarly, empirical potentials have been employed in the past to determine the lowest energy structures of medium sized gold clusters.[11-13] However, recently Zhao and coworkers[14] have used a combined scheme of DFT with empirical generic algorithms to generate a number of possible structural isomers for gold clusters of up to 20 atoms, which were further optimized at the DFT level to determine the lowest energy structures. They have found that small Au_n clusters adopt planar structures up to n = 6, flat cage structures are preferred in the range of n = 10-14 and a structural transition from flat-cage-like structure to compact near-spherical structure occurs at around n = 15. Xiao and Wang[15] used a plane wave DFT basis set and the PW91 functional for Au_{14} and Au_{20} to predict by interpolation that the crossover from planar to non planar gold clusters occurs at the cluster consisting of 15 gold atoms. Sankaran and Viswanathan[16] performed DFT calculation on Au_n clusters (n = 2-12) using B3LYP functional and LANL2DZ effective core potential basis set without imposing any symmetry and observed a 2D to 3D conversion at Au_5. Li et al.[19] have located the 2D-3D turnover for neutral gold clusters at Au_{12}. Thus, inspite of such large number of studies dedicated to the structure of both neutral and ionic gold clusters, there appears to be little consensus regarding the "turnover point" from clusters in which planar isomers are lowest in energy to those in which non planar isomers dominate.

Therefore, we were motivated to investigate the 2D-to-3D conversion of gold clusters using density functional theory with all electron scalar relativistic effects. Most studies on gold clusters make use of effective core potential (ECP), in which the core electrons are replaced by an effective potential, thereby eliminating the need for core basis functions. The use of ECP reduces the computational expense drastically. In contrast to these earlier calculations, the work described here uses a first principles all-electron method based on DFT incorporating scalar relativistic effects for the treatment of core electrons. We have attempted to predict a number of possible low-energy structural isomers for each Au_n cluster (n = 2 to 13) with unconstrained geometry optimizations starting from different initial candidate geometries.

1.2 Computational Details

The isomers of gold clusters Au_n (n = 2-13) have been fully optimized using Kohn-Sham Theory.[20,21] We used the generalized gradient approximation (GGA) in our calculations. At the GGA level, we have chosen the BLYP functional[22,23] which incorporates Becke's exchange and Lee-Yang-Parr correlation. The efficiency of the BLYP functional in studying gold clusters have been demonstrated by Bonačić-Koutecký et al.[24] in their work on silver-gold bimetallic clusters. The basis set chosen is DNP.[25] The DNP basis functions are the double-numerical atomic orbitals augmented by polarization functions, i.e, functions with angular momentum one higher than that of the highest occupied orbital in the free atom. The size is comparable with the Gaussian 6-31G** basis set, but the DNP basis set is supposed to be more accurate than a Gaussian basis set of similar size. This basis set is suitable even for treating completely dissociated atoms. Gold being a heavy atom, relativistic effects become important. So, all-electron calculations with scalar relativistic corrections are used. While calculations involving all-electron relativistic (AER) method are more difficult to perform due to the huge computational expense, they are supposed to provide better accuracy than those involving effective core potentials as a result of the lesser number of approximations in AER. The advantages of the all electron scalar relativistic method over the effective core potential methods have been demonstrated by Orita et al.[26] in their work on CO adsorption on Pt(111). They found that the AER method can correctly predict the atop adsorption site and gives adsorption energies which are closer to the experimental values than those predicted by ECP methods. Fine grid mesh points are employed for the matrix integrations. Self-consistent field procedures are done with a convergence criterion of 10^{-6} a.u. on the energy and electron density. All the calculations are carried out by using the $DMol^3$ program.[27] The nature of the stationary points has been characterized by running vibrational frequency calculations at the same level of theory. In order to determine the ground electronic state for a given cluster size, test calculations were initially performed in two spin states, singlet, and doublet, for neutral clusters having even and odd number of gold atoms, respectively. Then the same calculations were repeated in higher spin states, viz, triplet and quartet. An analysis of the results revealed that though the structures remained the same, calculations in higher spin states gave higher energies (2.1 eV to

3.6 eV) for all the clusters studied. So we decided to perform the calculations in the minimum spin states, singlet and doublet. For charged clusters the choice of singlet or doublet state was made depending upon the number of electrons being even or odd, respectively. For a given cluster size, the most stable structure is determined from the relative energy of the isomers. This is further confirmed by comparing their binding energies.

In order to determine the size evolution of the stability of the clusters and their electronic properties, we have determined the binding energy per atom, second difference of binding energy, fragmentation energy, first vertical ionization potential, electron affinity and chemical hardness of the stable structures.

The average binding energy per atom for neutral clusters is computed from:

$$E_b(n)=[nE(Au_1)-E(Au_n)]/n \tag{3.1}$$

where $E(Au_n)$ is the energy of a cluster with n atoms.

For ionic clusters, the formula used for binding energy per atom calculation is

$$BE = -E_{tot}^{\pm} / n \tag{3.2}$$

where $E_{tot}^{\pm} = E_n^{\pm} - (n-1)E_1 - E_1^{\pm}$ is the total energy of an ionized cluster, in which $E_1^{\pm}$ and $E_n^{\pm}$ are the energies of the singly charged Au atom (Au_1^{+}) and $Au_n^{\pm}$ clusters

The fragmentation energy for a cluster of size n has been calculated from:

$$D(n,n-1) = E(Au_{n-1}) + E(Au_1) - E(Au_n) \tag{3.3}$$

For the most stable structure for each cluster size n, the second difference of binding energy $\Delta^2 E_b(n)$ has been obtained as:

$$\Delta^2 E_b(n)=2E_b(n)-E_b(n+1)-E_b(n-1) \tag{3.4}$$

where $E_b(n)$ is the binding energy per atom of the cluster with n atoms.

The vertical ionization potential (IP) and electron affinity (EA) are calculated as:

$$IP = E(Au_n^{+}) - E(Au_n) \tag{3.5}$$

$$EA = E(Au_n) - E(Au_n^{-}) \tag{3.6}$$

where $E(Au_n^{+})$ and $E(Au_n^{-})$ are the total energy of the cationic and anionic clusters, respectively at the optimized geometry of the neutral cluster.

Chemical hardness is used as a parameter to determine the reactivity of a system. In density functional theory, hardness (η) of an electronic system is defined as the second derivative of energy (E) with respect to the number of electrons (N) at constant external potential, $v(\vec{r})$ [28]

$$\eta = \frac{1}{2}\left(\frac{\partial^2 E}{\partial N^2}\right)_{v(\vec{r})} = \frac{1}{2}\left(\frac{\partial \mu}{\partial N}\right)_{v(\vec{r})} \tag{3.7}$$

where μ is the chemical potential of the system.

Using the finite difference approximation and the Koopmans' theorem, global hardness, η can be approximated as

$$\eta = \frac{IP - EA}{2} \tag{3.8}$$

where *IP* and *EA* are the first vertical ionization potential and electron affinity, respectively of the chemical system.

3.3 Results and Discussion

In order to determine the best exchange-correlation functional to be used for the calculations, we made a comparative study of the bond length, vibrational frequency and dissociation energy of the gold dimer using various functionals. The results are presented in Table 3.1.

Table 3.1. Calculated properties of Au_2.

Method	$R_e(\text{Å})$	$\omega_e(\text{cm}^{-1})$	$D_e(\text{eV})$
BLYP/DNP	2.53	171	2.203
BOP/DNP	2.61	137	2.025
BP/DNP	2.57	148	2.324
HCTH/DNP	2.60	135	2.007
PBE/DNP	2.57	147	2.400
PW91/DNP	2.57	148	2.426
rPBE/DNP	2.60	140	2.140
VWN_BP/DNP	2.57	148	2.325
VWN/DNP	2.44	205.8	2.982
Experimental	2.47	191	2.302

Experimental values are taken from References [29,45].

The experimental value of the bond length for Au_2 is 2.47 Å.[29] Among the functionals used, the VWN functional gives the best value of bond length, but the vibrational frequency and dissociation energy are overestimated. The dissociation energy calculated by the VWN_BP and the BP functionals are close to the

experimental value of 2.302 eV, but the vibrational frequency is far too low. Among all the available functionals, it is observed that the BLYP functional gives the best estimate of all the three parameters considered. Hence we choose this functional for the present study.

For all the Au$_n$ clusters (n = 2-13) a number of low-energy structures were obtained along with the most stable structure (Figures 3.1(a), 3.1(b)). The total energy of all the clusters and their relative energies along with the symmetry point group are given in Table 3.2. Each structure is identified by its shape and symmetry. The energy differences are given relative to the most stable structure. However, it should be noted that DFT cannot distinguish the structures whose energy difference falls within the ca. 0.2 eV range.[30] We take this energy as the "isomer-coexistence interval". The binding energy per atom, second difference of binding energy, fragmentation energy, average bond length, HOMO-LUMO energy gap, first vertical ionization potential and electron affinity and the value of chemical hardness for each structure are given in Table 3.3. In what follows, we will first discuss and compare structure and energetics of Au$_n$ clusters and then their electronic properties.
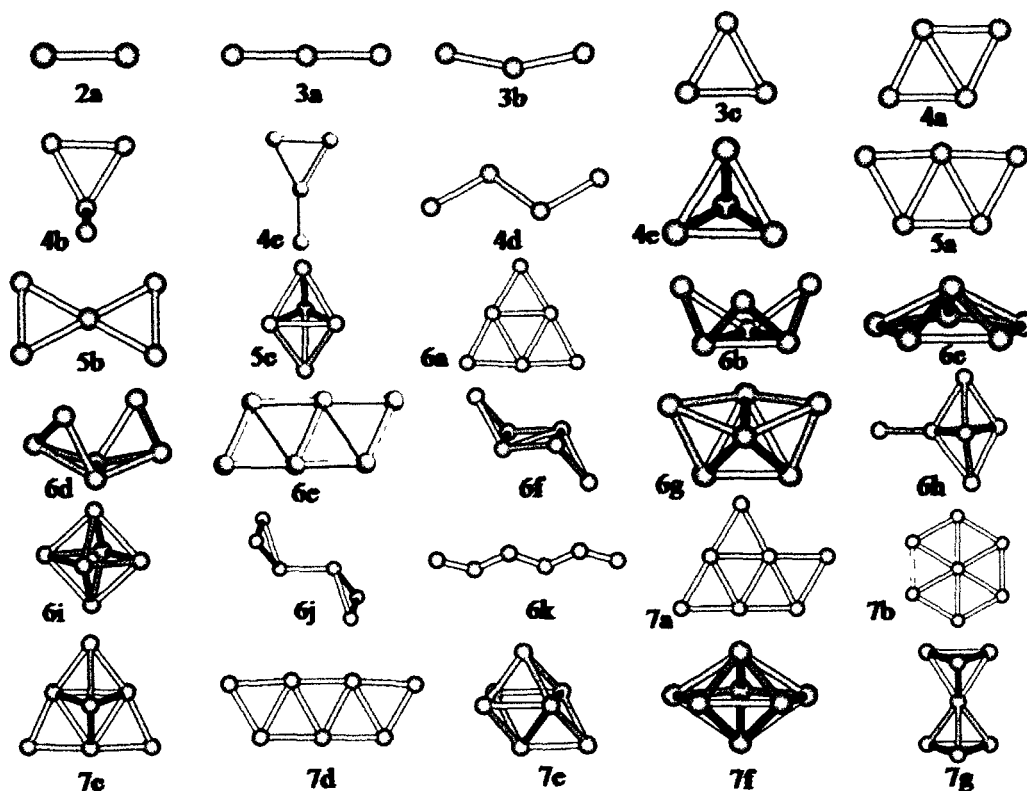
Figure 3.1(a). The optimized structures of gold neutral clusters (Au$_n$, n = 2 to 7) at BLYP/DNP level of calculations.

3.3.1 Structure and Energetics

3.3.1.1 Neutral gold clusters

Au₂: We first present our calculated values of Au_2 and compare them with the reported experimental and theoretical values. The calculated bond length, binding energy and vibrational frequency for Au_2 are 2.53 Å, 2.214 eV and 171 cm^{-1}, respectively. These GGA calculated values are in satisfactory agreement with experimental results (R_e = 2.47 Å, E_b = 2.30 eV and v = 191 cm^{-1}).[31,32] The BLYP/DNP level of theory gives 2.4% error in bond length, 8.8% error in binding energy and 10.4% error in vibrational frequency. However, our values are still better than some of the theoretical values reported earlier.[4,14] The LDA results of Wang et al.[14] gave a value of 2.55 Å for Au-Au bond length. Using the PW91PW91 exchange-correlation functional, Walker[4] found that the calculated bond length is 2.56 Å with Stuttgart 1997 basis set, 2.55 Å with LANL2DZ and 2.54 Å with CRENBL. The previous theoretical calculations show that the error in the calculated vibrational frequencies is > 10% using various functionals and basis sets.[4] Using the PW91PW91 exchange-correlation functional, the calculated frequency is 126 cm^{-1} with Stuttgart 1997 basis set, 170 cm^{-1} with LANL2DZ and 172 cm^{-1} with CRENBL.[4] Our binding energy values are in very good agreement with PW91PW91/LANL2DZ (2.20 eV) and PW91PW91/CRENBL (2.23 eV) levels of theory. The value of Au-Au bond length determined by us agrees well with the CCSD(T) value of 2.512 Å.[33] The calculated ionization potential (IP) for Au_2 falls within 2.2% of the experimental value.

Au₃: Three isomers (3a-3c) are obtained with the linear one being lowest in energy. This is in agreement with DFT-LDA results of Wang et al.[14] who predicted a linear structure and also with earlier CASSCF[34] studies but disagrees with the lowest energy triangular structure reported by Walker.[4] The next higher in energy is a V shaped structure (3b) with a bond angle of 154.2°and an energy difference of 0.010 eV as compared to the linear molecule. The highest energy structure is a triangle 3c (D_{3h}) with an energy difference of 0.052 eV over the lowest energy linear structure. Another study[19] has the V shaped cluster as the lowest in energy, followed by the linear structure, and has the triangular geometry as the highest energy structure. The accuracy of the DFT method for calculating the energy difference between gold

clusters has been estimated to be 0.1 eV[6] (or 0.2 eV[30]) and so the three structures are probably not distinguishable at this level of theory. The values of binding energy per atom for the structures 3a, 3b and 3c are 1.209, 1.205 and 1.191 eV, respectively.

Au₄: For Au₄ we have obtained five stable structures as shown in Figure 3.1 (4a-4e). The calculations reveal three structures (4a, 4b, 4c) within the "isomer-coexistence interval" of 0.2 eV (Table 3.2). Thus, the lowest energy structures are a rhombus (4a) with C_s symmetry, a "distorted Y" shaped one (4b) and a "planar Y" shaped structure (4c). The rhombus is slightly distorted with opposite edges revealing Au-Au bond lengths of 2.64 and 2.69 Å, respectively. The '4a' structure was reported to be the most stable structure by Walker[4] and Zhao et al.[5] The other structures are a zigzag structure (4d) and a tetrahedron geometry (4e). Structures '4d' and '4e' are higher in energy than '4a' by 0.381 eV and 1.008 eV, respectively. The "distorted Y" structure (C_1) is three dimensional, and to the best of our knowledge, it has not been reported in earlier theoretical studies. The average bond length for this structure is 2.68 Å. Another structure, a square shaped one was also obtained. However, it was found to be a transition state. Other authors have also predicted that the most stable Au₄ cluster has a rhombic structure with the "planar Y" shaped structure lying higher in energy.[2,19,24] Our results match this trend in energy. The rhombic and tetrahedron structures have binding energies per atom of 1.49 eV and 1.24 eV, respectively. Second-order many-body perturbation theory calculations[35] give binding energy per atom values of 1.73 eV and 1.37 eV for these structures.

Au₅: In case of Au₅, three stable structures were obtained as shown in Figure 3.1 (5a-5c). The lowest energy cluster is a "W" shaped one with C_{2v} symmetry (5a). This structure has a binding energy per atom value of 1.623 eV which is higher than that for the structures '5b' and '5c'. There is an X shaped structure 5b (D_{2h}) lying 0.387 eV higher in energy. A higher energy three dimensional trigonal bipyramidal structure with D_{3h} symmetry is also found in our BLYP/DNP level calculation. This structure is 0.805 eV higher in energy than the "W" shaped structure. Our results are in agreement with the results of Walker.[4] The binding energy per atom for the structures '5b' and '5c' are 1.546 eV and 1.462 eV, respectively.

Au$_6$: The stable structures obtained in our calculations for Au$_6$ are shown in Figure 3.1 (6a-6k). We have obtained two nearly degenerate lowest-lying Au$_6$ structures, a triangle (6a, C_{2v}) and a tri-capped triangle (6b, C_l). The structure '6b' lies only 0.001 eV higher in energy compared to the structure '6a'. They have the same value of binding energy per atom of 1.843 eV. The tri-capped triangle is three dimensional and consists of four triangles, one lying in the plane and three above the plane - one on each side of the first triangle. All the four triangles are isosceles. The one lying on the plane has Au-Au bond lengths of 2.71 Å and 2.76 Å and for the other triangles the bond lengths lie between 2.63 Å and 2.67 Å. A lowest energy triangular structure for Au$_6$ with D_{3h} symmetry was predicted by other workers.[2,4,19] Hence, within the DFT error, there is a 2D-3D coexistence for neutral gold clusters at Au$_6$. The next higher energy structure is a pentagonal pyramid (6c) with C_{5v} symmetry which is also reported by Bonačić-Koutecky et al.[36] Among the other stable structures for Au$_6$ are a bicapped butterfly structure (6d) with C_{2h} symmetry, a planar parallelogram structure (6e) which is a combination of two rhombuses, a chair structure (6f) with C_{2h} symmetry. In structure '6d', the Au-Au bond length varies between 2.64 Å and 2.80 Å for the basic butterfly structure while for the capping the bond lengths are 2.63 Å and 2.64 Å. The chair form of Au$_6$ consists of a planar central Au$_4$ ring and two Au atoms lying above and below the ring connected to two opposite edges. The average Au-Au distance for the Au$_4$ ring of this structure is 2.63 Å while for the other bonds it is 2.67 Å. The values of binding energy per atom, the first vertical ionisation potential and electron affinity for this structure are 1.675 eV, 7.473 eV and 3.054 eV, respectively. Other higher energy structures include a boat (6g, C_l), capped trigonal bipyramid (6h, C_s), an octahedron (6i, O_h) and a see-saw structure (6j) consisting of two equilateral triangles connected through their vertices. The two triangles are non overlapping. The highest energy structure (6k) is a zigzag one (C_l). The pentagonal pyramid, capped bipyramid, rhombus and boat structures have also been reported by Walker.[4] In case of the trigonal bipyramid structure '5c', the Au-Au bond distances for the triangular ring is 2.78 Å and the other bond distances are 2.75 Å. For the capped trigonal bipyramid the Au-Au distance for the triangular ring varies between 2.74 Å and 2.77 Å. The other bond lengths lie between 2.71 Å and 2.85 Å. The capped Au atom lies at a distance of 2.53 Å from the nearest atom in the triangular ring. The groups of Michaelian[11] and Wilson[12] found that the bipyramid is the lowest energy structure of Au$_6$ using n-

body Gupta potential and empirical Murrell-Mottram many body potential, respectively. Both n-body Gupta and the Murrell-Mottram many-body potentials are designed to reproduce properties of bulk crystalline gold which may not reproduce the properties of clusters. To the best of our knowledge, the tri-capped triangle (6b), the chair (6f), and the see-saw structure (6j) have not been reported in any previous experimental and theoretical work.
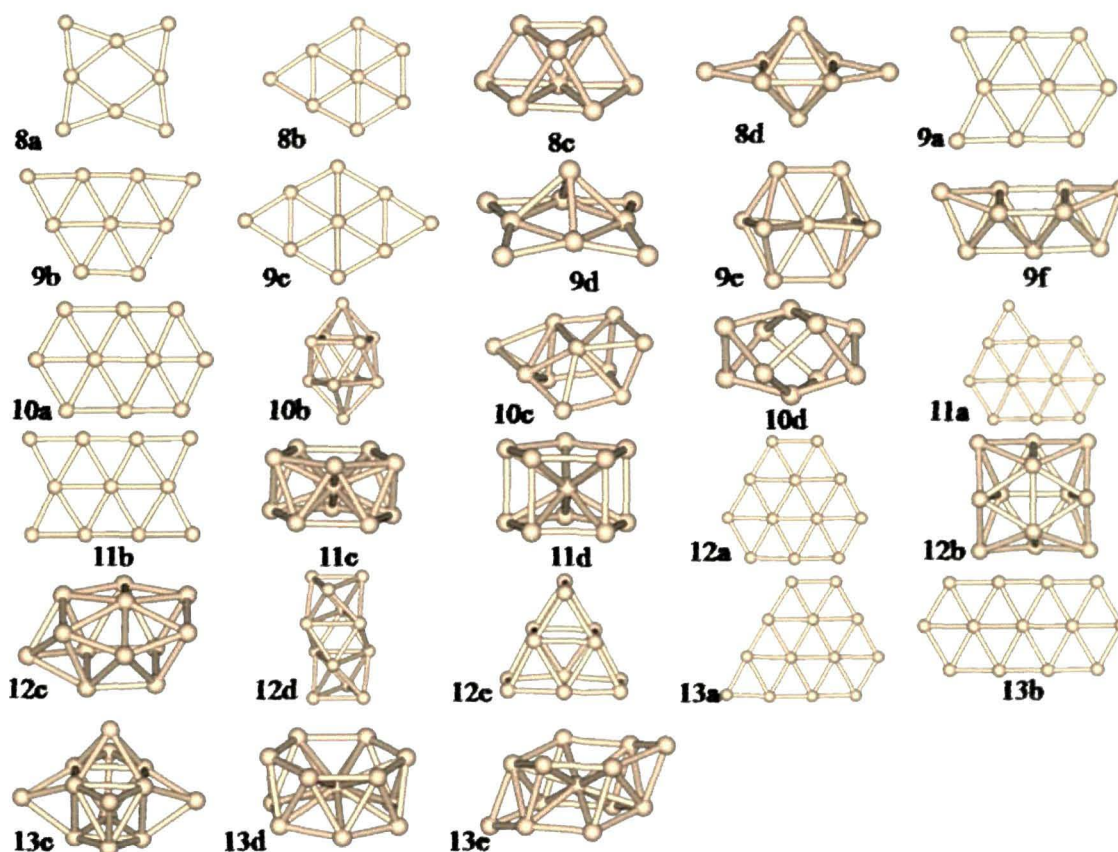
Figure 3.1(b). The optimized structures of neutral gold clusters (Au$_n$, n = 8 to 13) at BLYP/DNP level of calculations.

Au$_7$: Au$_7$ has seven stable structures (7a-7g). Within the isomer-coexistence interval, the lowest energy structures for Au$_7$ are a planar capped triangle with C_s symmetry (7a, C_s) and a hexagon with one gold atom occupying the centre of the ring (7b, D_{6h}). A planar capped triangle with C_s symmetry was also obtained as the minimum energy structure by other workers by adding a gold atom to the planar triangular structure of Au$_6$.[1,4,19,36] Then we have a bi edge-capped trigonal bipyramid structure (7c) which is about 0.393 eV higher in energy than the hexagonal structure.

Wang *et al.*[14] reported a three dimensional pentagonal bipyramid structure as the lowest energy structure for Au_7. In our case this pentagonal bipyramid structure was found to be 0.671 eV higher in energy than the minimum energy structure. Gilb *et al.*[37] found a hexagon with one central atom as the lowest energy structure for Au_7 cation. In our case this structure is found to be next higher in energy as compared to the minimum energy capped triangular structure. The next higher energy structure is a planar extended W (7d, C_{2v}) with an energy difference of 0.453 eV over the capped triangle. Other high energy structures include a face capped octahedron (7e, C_{3v}), a pentagonal bipyramid (7f, D_{5h}) and an eclipsed sandwich structure '7g' with D_{3h} symmetry. This eclipsed sandwich structure consists of two triangular rings, one on top of the other connected by a gold atom at the middle. The average bond length is 2.74 Å. This structure was not reported in earlier studies. It has the highest energy among all the structures with the energy difference between this and the capped trianglar structure being 1.835 eV. A comparison of the structures '6i' and '7e' shows that the Au-Au bond distances which have a value of 2.78 Å in the octahedron structure (6i) changes as a result of face capping. In the structure '7e', the Au-Au distances in the octahedron varies from 2.74 Å to 2.91 Å. The capped gold atom lies at a distance of 2.71 Å from an atom in the capped face of the octahedron. We did not find a 2D-3D coexistence for Au_7 as observed for Au_6.

Au_8: The lowest energy structure for Au_8 cluster is clearly a planar tetra edge capped rhombus (8a) with D_{2h} symmetry (Figure 3.2). Our calculated minimum energy structure is in agreement with those reported in the literature.[2,4,19] Wang *et al.*[14] reported that a distorted bicapped octahedron is the lowest energy structure. In our case we have obtained a bi-edge capped octahedron as the highest energy structure. In an earlier paper, Häkkinen and Landman[1] reported a capped tetrahedron as the lowest energy structure for neutral Au_8 cluster. The other structures obtained in our calculation are a capped hexagon (8b, C_s) and a three dimensional bi edge capped octahedron (8d, D_{2h}). Another three dimensional structure (8c) with C_{2v} symmetry is obtained which is higher in energy than the minimum energy planar structure by 0.706 eV. Structure 8d has the highest energy with the energy difference between this and the minimum energy planar structure being 1.604 eV. The binding energy per atom value for these isomers of Au_8 lie in

the range 1.923 to 1.723 eV. The minimum energy planar structure '8a' has the highest value of binding energy per atom as expected.

Table 3.2. Shape, symmetry, total energy and relative energy values for Au_n clusters, n=2-13 optimized at the BLYP/DNP level of theory. All energies are in eV.

n	Structure No.	Shape	Symmetry	Total energy including ZPVE	Relative Energy
2	2	Linear	$D_{\infty h}$	-1001298.46578	
3	3a	Linear	$D_{\infty h}$	-1501948.02002	0.000
3	3b	V	C_{2v}	-1501948.00969	0.010
3	3c	Triangle	D_{3h}	-1501947.96816	0.052
4	4a	Rhombus	C_s	-2002598.48497	0.000
4	4b	Distorted Y	C_1	-2002598.42509	0.060
4	4c	Y	C_{2v}	-2002598.34697	0.138
4	4d	Zigzag	C_s	-2002598.10427	0.381
4	4e	Tetrahedron	T_d	-2002597.47693	1.008
5	5a	W	C_{2v}	-2503248.77241	0.000
5	5b	X	D_{2h}	-2503248.38505	0.387
5	5c	Trigonal bipyramid	D_{3h}	-2503247.96743	0.805
6	6a	Triangle	C_{2v}	-3003899.84412	0.000
6	6b	Tricapped triangle	C_1	-3003899.84324	0.001
6	6c	Pentagonal pyramid	C_{5v}	-3003898.92761	0.917
6	6d	Bicapped butterfly	C_{2h}	-3003898.84505	0.999
6	6e	Parallelogram	C_1	-3003898.84369	1.000
6	6f	Chair	C_{2h}	-3003898.83910	1.005
6	6g	Boat	C_1	-3003898.51200	1.332
6	6h	Capped trigonal bipyramid	C_s	-3003898.31692	1.527
6	6i	Octahedron	O_h	-3003898.17314	1.671
6	6j	See saw	C_{2h}	-3003898.03159	1.813
6	6k	Zigzag	C_1	-3003897.81153	2.003
7	7a	Capped Triangle	C_s	-3504549.50540	0.000
7	7b	Hexagon	D_{6h}	-3504549.44987	0.056
7	7c	Bi edge-capped trigonal bipyramid	C_s	-3504549.11205	0.393
7	7d	Extended W	C_{2v}	-3504549.05293	0.453
7	7e	Face capped octahedron	C_{3v}	-3504548.88791	0.618
7	7f	Pentagonal bipyramid	D_{5h}	-3504548.83410	0.671
7	7g	Eclipsed sandwich	D_{3h}	-3504547.67017	1.835
8	8a	Tetra edge capped rhombus	D_{2h}	-4005200.43709	0.000
8	8b	Capped hexagon	C_s	-4005200.14378	0.293
8	8c	Three dimensional structure	C_{2v}	-4005199.73131	0.706
8	8d	Bi edge-capped octahedron	D_{2h}	-4005199.83354	1.604
9	9a	Bi edge-capped hexagon I	C_{2v}	-4505850.54997	0.000

n	Structure No.	Shape	Symmetry	Total energy including ZPVE	Relative Energy
9	9b	Bi edge-capped hexagon II	C_s	-4505850.53316	0.017
9	9c	Bi edge-capped hexagon III	D_{2h}	-4505850.47574	0.074
9	9d	Tetra edge capped square pyramid	C_{4v}	-4505850.27459	0.275
9	9e	Condensed trigonal bipyramid	D_{2h}	-4505848.62416	1.926
9	9f	Boat	D_3	-4505848.52930	2.021
10	10a	Tri capped hexagon	D_{2h}	-5006501.24075	0.000
10	10b	Square antiprism	C_1	-5006500.07229	1.168
10	10c	Three dimensional structure I	C_1	-5006499.00000	1.922
10	10d	Three dimensional structure II	D_{4d}	-5006498.84051	2.400
11	11a	Tetra capped hexagon	C_s	-5507151.46912	0.000
11	11b	Tetra edge capped hexagon	D_{2h}	-5507151.30703	0.162
11	11c	Staggered Sandwich	C_{2h}	-5507149.27896	2.190
11	11d	Eclipsed Sandwich	D_{5h}	-5507149.14500	2.324
12	12a	Pentacapped hexagon	D_{3h}	-6007802.52572	0.000
12	12b	Three dimensional structure I	D_{2d}	-6007800.84008	1.686
12	12c	Three dimensional structure II	C_1	-6007800.77947	1.746
12	12d	Ladderane	D_{3d}	-6007800.52935	1.996
12	12e	Distorted Condensed Triangle	C_{2v}	-6007800.42735	1.938
13	13a	Hexa capped hexagon	C_s	-6508452.31362	0.000
13	13b	Condensed hexagon	D_{2h}	-6508452.24670	0.067
13	13c	Tricapped boat	C_{2v}	-6508451.61101	0.703
13	13d	Staggered Sandwich	D_{6d}	-6508450.93911	1.375
13	13e	Distorted Sandwich	C_{2h}	-6508450.71491	1.599

Table 3.2 continued

Au9:   Au9 has three structures within an energy difference of 0.1 eV. The calculated lowest energy structure of Au9 is a "bi edge-capped hexagon I" (9a) with C_{2v} symmetry. This structure is in agreement with the results of Walker.[4] Recent calculations by Xiao and Wang[15] and that of Bonačić-Koutecký and co-workers[36] predict the "bi edge-capped hexagon II" structure (9b) of Figure 3.2 as the lowest energy structure for Au9. We found this structure to be only 0.017 eV higher in energy than the capped hexagon I structure. We also note that Wang *et al.*[14] and Häkkinen and Landman[1] predicted that the lowest energy structure for Au9 has a three dimensional structure. Here, the lowest energy three dimensional structure is

found to be 0.275 eV higher in energy compared to the minimum energy structure. Clearly, there is no 2D-3D coexistence for the stable isomers of Au_9. The two dimensional "bi edge-capped hexagon III" structure (9c, D_{2h}) also lies within the isomer coexistence interval of the lowest energy structure '9a' as does the structure '9b'. Thus the three two dimensional structures '9a', '9b' and '9c' may be said to coexist as the minimum energy structure. Higher energy stable structures include the three dimensional tetra edge-capped square pyramid (9d, C_{4v}), a condensed trigonal bipyramid structure (9e, D_{2h}) and a boat structure with D_3 symmetry (9f). The condensed trigonal bipyramid structure (9e, D_{2h}) consists of two trigonal bipyramids condensed through a vertex of the triangular ring. The average bond length for this cluster is 2.78 Å. To the best of our knowledge, this structure has not been reported previously. The boat shaped one with D_3 symmetry is another new structure obtained in this study. Among all the stable structures obtained for Au_9, this boat structure has the highest energy with the energy difference between this and the most stable bi edge capped hexagon I being 2.021 eV.

Au_{10}: The lowest energy structure for Au_{10} is a tricapped hexagon (10a) having D_{2h} symmetry which is in agreement with the result obtained by Walker[4] and Li et al.[19] The other stable structures are three dimensional. The energy difference between the minimum energy planar structure and the next higher energy three dimensional square antiprism structure (10b) is 1.168 eV. Structure '10b' consists of two square pyramids placed back to back in staggered conformation. This structure has been obtained by Furche et al.[6] and by Häkkinen et al.[2] in their study on gold cluster anions. The other two higher energy structures (10c and 10d) have C_1 and D_{4d} symmetry with average bond lengths 2.79 Å and 2.70 Å, respectively. The highest energy structure '10d' is 2.4 eV higher in energy than the minimum energy planar structure.

Au_{11}: In agreement with the results of Häkkinen et al.[2] for gold cluster anions, we find a planar tetra capped hexagon (11a, C_s) as the minimum energy structure for Au_{11}. The next higher energy structure (11b) is also planar and is separated by an energy difference of 0.162 eV from the structure '11a'. Structure '11a' has been reported by several groups.[2,6,19] We have also obtained two previously unreported structures - one of them is a staggered sandwich structure (11c, C_{2h}). In this case,

the atoms in the two pentagonal rings are placed in staggered position with respect to each other. The average bond length of the pentagonal ring is 2.90 Å while the central gold atom is separated from an atom in the pentagonal ring by a distance of 2.74 Å. The other is an eclipsed sandwich structure (11d, D_{5h}). This structure consists of two overlapping regular pentagonal rings with Au-Au distance of 2.79 Å with a gold atom in between the two planes. All the distances between the constituent atoms of the pentagonal ring and the central gold atom are equal (2.79 Å). The distance between an atom in the pentagonal ring and the gold atom at the centre is 2.79 Å. The pentagonal rings are separated from each other by a distance of 2.82 Å. The binding energy per atom value for the two structures are 1.803 eV and 1.791 eV, respectively.

Au$_{12}$: Again, we find a planar penta capped hexagon structure to be the lowest in energy for Au$_{12}$ (12a, D_{3h}). This structure consists of a hexagonal ring with capping at five positions, three on the edges and two at the vertices. This is in agreement with the results of Furche *et al.*[6] and Häkkinen *et al.*[2] for gold cluster anions. This structure has also been obtained by Hou and coworkers[5] in their study of two dimensional gold clusters. Li *et al.*[19] also obtained this structure. However, this structure was found to be higher in energy by 0.022 eV than the minimum energy structure, which they found to be three dimensional. Then, we have two three dimensional structures 12b (D_{2d}) and 12c (C_l) lying 1.686 eV and 1.746 eV, respectively higher in energy than the minimum energy planar structure. Structure '12b' consists of six four membered rings, two of which are planar and the rest are butterfly shaped. The average bond length for the planar ring is 2.77 Å while for the butterfly shaped rings it is 2.81 Å. The next higher in energy is a ladderane structure (12d) having D_{3d} symmetry with four stacked triangles, one on top of the other in staggered positions. All the triangles are equilateral. The top and bottom triangles have Au-Au bond length of 2.81 Å while for the middle two the Au-Au bond length is 2.98 Å. The binding energy per atom for this structure is 1.913 eV. This exotic structure was not reported in earlier studies. The highest in energy is a distorted condensed triangle (12e) with C_{2v} symmetry. This structure consists of two hexanuclear gold triangles (similar to structure 6a) joined in a parallel conformation. The two triangles deviate slightly from planarity, the Au-Au-Au bond angle of the deviated edge being 151.7°. Li *et al.*[19] have found this structure to be the minimum

energy structure for Au_{12}. In our study, we find that the 12e structure is 1.938 eV higher in energy than the minimum energy planar structure 12a.

Au_{13}: Five stable structures were obtained with two planar structures, a hexa capped hexagon (13a, Cs) and a planar condensed hexagon structure (13b, D_{2h}) as lowest structures within the "isomer coexistence interval". Hou and coworkers[5] have also obtained the condensed hexagon structure consisting of two hexagonal rings condensed through a vertex as the most stable structure. Taking the hexagonal ring as the base, Häkkinen *et al.*[2] have also found a planar structure as the minima in their study on gold cluster anions. However, their structure contains capping at different positions whereas there is no capping in our structure. Kappes and coworkers[37] have found a three dimensional C_{2v} structure as the lowest energy one in their study on gold cluster cations. The other stable structures for Au_{13} are three dimensional and higher in energy than the planar ones. Among them is a tricapped boat structure (13c, C_{2v}) and two hitherto unreported structures: one is a staggered sandwich structure (13d, D_{6d}) consisting of two six member planar rings placed one on top of the other with one gold atom in between the planes. The six member rings are regular hexagons with the Au-Au distance being 2.70 Å while the distance of the central gold atom from the atoms in the hexagonal ring is 2.96 Å. A comparison of structures '11c' and '13d', both of which are staggered sandwiches, shows that in the case of the pentagonal ring (11c), the Au-Au distance is not uniform with the average bond length being 2.90 Å, while the hexagonal ring shows equal Au-Au bonds. On going from Au_{11} to Au_{13} there is an increase in the distance between the central gold atom and atoms in the planar ring from 2.74 Å to 2.96 Å. The other structure is a distorted sandwich structure (13e, C_{2h}) with two distorted non planar Au_6 rings. The average bond length of this structure is 2.79 Å.

Table 3.3. Binding energy/atom, second differential of binding energy, fragmentation energy, average Au-Au distance, HOMO-LUMO gap, first vertical ionisation potential, electron affinity and hardness for Au_n (n = 2-13) clusters. All energies are in eV.

n	Structure No.	E_b	$\Delta^2 E_b$	D	Average Bond Length(Å)	HOMO-LUMO gap	IP	EA	η
2	2	1.102		2.203	2.53	1.637	9.294	1.820	3.737
3	3a	1.209	-0.175	1.423	2.55	2.231	8.754	3.361	2.696
3	3b	1.205			2.55	2.005	8.679	3.347	2.666
3	3c	1.191			2.68	0.007	7.416	2.208	2.604
4	4a	1.490	0.148	2.334	2.68	0.927	7.996	2.387	2.804
4	4b	1.475			2.68	0.966	8.130	2.585	2.773
4	4c	1.455			2.62	0.976	7.972	2.484	2.744
4	4d	1.395			2.68	1.140	8.337	2.867	2.735
4	4e	1.238			2.75	1.513	7.309	2.430	2.440
5	5a	1.623	-0.086	2.156	2.68	1.142	7.790	2.962	2.414
5	5b	1.546			2.65	0.505	7.115	2.720	2.198
5	5c	1.462			2.78	0.190	7.267	2.643	2.312
6	6a	1.843	0.272	2.940	2.68	1.727	7.840	2.243	2.798
6	6b	1.843			2.68	1.721	7.839	2.244	2.797
6	6c	1.690			2.73	1.641	7.633	2.291	2.671
6	6d	1.676			2.78	0.189	7.472	3.051	2.211
6	6e	1.676			2.69	0.176	7.413	3.050	2.181
6	6f	1.675			2.68	0.180	7.473	3.054	2.210
6	6g	1.621			2.73	0.475	7.420	2.667	2.377
6	6h	1.588			2.71	0.630	7.576	2.883	2.346
6	6i	1.564			2.55	1.806	7.541	2.983	2.279
6	6j	1.541			2.68	0.684	7.338	3.010	2.164
6	6k	1.504			2.55	0.832	7.860	3.477	2.192
7	7a	1.798	-0.170	1.530	2.69	1.077	7.225	2.870	2.178
7	7b	1.790			2.70	1.396	6.900	2.921	1.989
7	7c	1.742			2.76	0.690	6.927	2.798	2.065
7	7d	1.733			2.69	0.467	7.367	3.374	1.997
7	7e	1.710			2.78	1.306	6.710	3.094	1.808
7	7f	1.702			2.78	0.784	7.069	2.778	2.146
7	7g	1.536			2.74	0.591	6.798	2.866	1.966
8	8a	1.923	0.127	2.856	2.67	1.420	7.512	2.834	2.339
8	8b	1.887			2.70	0.729	7.342	2.945	2.198
8	8c	1.835			2.76	1.332	7.389	2.407	2.491
8	8d	1.723			2.76	0.144	7.447	3.326	2.061
9	9a	1.930	-0.056	1.982	2.70	0.584	7.146	3.239	1.954
9	9b	1.928			2.70	0.786	7.373	3.467	1.953
9	9c	1.922			2.71	0.051	7.148	3.064	2.042
9	9d	1.899			2.72	1.113	7.319	3.195	2.062
9	9e	1.716			2.78	0.073	6.678	2.962	1.858
9	9f	1.705			2.78	0.530	7.163	3.371	1.896
10	10a	1.993	0.053	2.560	2.71	1.172	7.349	2.967	2.191
10	10c	1.801			2.76	0.255	6.831	2.924	1.954
10	10d	1.753			2.70	0.845	6.709	2.841	1.934

Table 3.3 continued

n	Structure No.	E_b	$\Delta^2 E_b$	D	Average Bond Length(Å)	HOMO -LUMO gap	IP	EA	η
11	11a	2.002	-0.054	2.097	2.71	0.913	7.025	3.553	1.736
11	11b	1.988			2.70	0.727	7.004	3.606	1.699
11	11c	1.803			2.87	0.346	6.653	3.071	1.791
11	11d	1.791			2.80	0.011	6.565	3.018	1.774
12	12a	2.066	0.088	2.765	2.71	0.938	7.236	3.209	2.014
12	12b	1.939			2.80	0.229	7.360	3.035	2.163
12	12c	1.934			2.78	0.468	6.934	3.093	1.921
12	12d	1.913			2.80	1.423	7.051	3.344	1.853
12	12e	1.904			2.74	0.356	6.863	3.207	1.828
13	13a	2.047		1.657	2.71	0.033	6.770	3.343	1.714
13	13b	2.042			2.71	0.612	6.921	3.760	1.580
13	13c	1.99			2.80	0.539	6.487	3.051	1.718
13	13d	1.941			2.76	0.070	6.842	3.424	1.709
13	13e	1.924			2.79	0.058	7.415	3.250	2.082

3.3.1.2   Cationic gold clusters

Geometry optimizations for singly charged cationic gold clusters have been performed in a similar manner. The minimum energy structures of the cationic gold clusters Au_n^+ (n = 2-13) are shown in Figure 3.2 while their properties are listed in Table 3.4. As can be observed from the figure, all the minimum energy structures are planar. The cationic dimer Au_2^+ exhibits a bond length of 2.57 Å which is larger than that of the neutral dimer, where the Au-Au distance is 2.53 Å. For Au_3^+ the linear geometry yielded a negative vibrational frequency. As obtained for the neutral cluster, the minimum energy structure for the cationic Au_4^+ cluster is a rhombus. The next higher energy structure, a tetrahedron lies 0.35 eV higher in energy. For Au_5^+ cluster, the "W" structure exhibited negative frequency. Of the other two structures obtained, "X" lies lower in energy. This is in agreement with the results of Walker.[4] For Au_6^+, we could obtain ten isomeric structures devoid of negative frequency. Of these, the triangular structure with a HOMO-LUMO gap of 2.11 eV lies lowest in energy. This is the largest HOMO-LUMO gap among the minimum energy Au_n^+ structures obtained in the present study.

In case of the Au_7^+ cluster, the minimum energy structure is the same capped triangular structure as obtained for the neutral cluster. The other structures include a bi edge-capped trigonal bipyramid, an extended W, a pentagonal bipyramid and an eclipsed sandwich structure. For Au_8^+, we have obtained four structures, out of
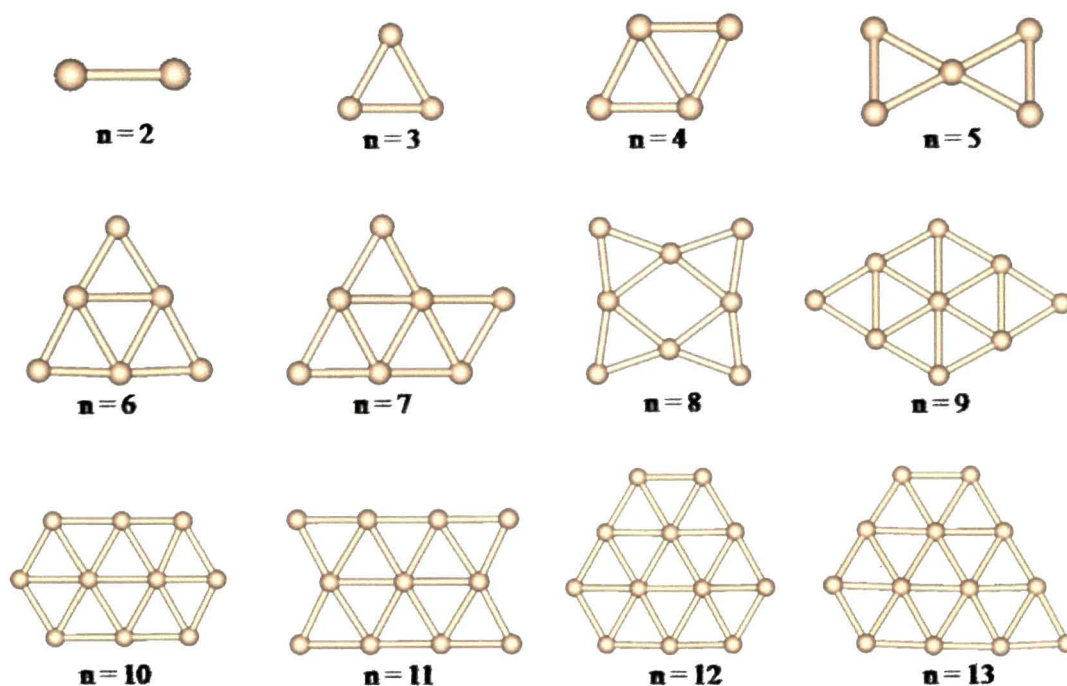
Figure 3.2. The calculated structures of cationic gold clusters (Au_n^+, n = 2 to 13) at BLYP/DNP level of calculations.

which the tetra edge capped rhombus lies lowest in energy. This is in agreement with the results of Remacle *et al.*[17] In case of the neutral cluster too, this same structure exhibited the lowest energy. However, the average bond length in case of cationic cluster is slightly longer, 2.68 Å, compared to 2.67 Å for the neutral cluster. In case of Au_9^+, the bi edge-capped hexagon with an average bond length of 2.71 Å is the minimum energy structure. Three structures were obtained for the Au_{10}^+ cluster, of which two are planar. Of these, the tricapped hexagonal structure lies lowest in energy. This structure is similar to the minimum energy neutral Au_{10} structure. For Au_{11}^+, the minimum energy structure is a tetra edge capped hexagon. This structure has a small HOMO-LUMO gap of 0.52 eV. For the neutral cluster this structure lies 0.162 eV higher in energy compared to the minimum energy planar structure. For Au_{12}^+ and Au_{13}^+ the minimum energy structures are a pentacapped hexagon and a hexacapped hexagon, respectively. Thus the optimal geometries of cationic Au_n^+ clusters for n = 3,5,9,11 differ from those of the neutral ones.

Table 3.4. Binding energy/atom, second differential of binding energy, average Au-Au distance and HOMO-LUMO gap for Au_n^+ (n = 2-13) clusters.

n	E_b	$\Delta^2 E_b$	Average Bond Length($\mathring{A}$)	HOMO-LUMO gap
	1.284		2.57	2.044
3	1.940	0.684	2.68	1.760
4	1.911	-0.182	2.68	0.794
5	2.063	0.069	2.64	1.052
6	2.146	0.061	2.68	2.105
7	2.169	-0.008	2.69	0.873
8	2.199	-0.008	2.68	1.029
9	2.237	0.052	2.71	1.243
10	2.224	-0.021	2.71	1.196
11	2.231	-0.030	2.69	0.514
12	2.268	0.018	2.71	0.906
13	2.288		2.71	0.918

Energies are in eV.

3.3.1.3 Anionic gold clusters

The optimized geometries of the minimum energy anionic Au_n^- (n=2-13) clusters are shown in Figure 3.3. As obtained for the neutral and cationic clusters, the minimum energy structures are planar in the entire size range considered. Fernández et al.[38] found anionic gold clusters to be planar upto n = 12 by using DFT GGA calculations based on norm conserving pseudopotentials and an atomic basis set. The dimer bond length elongates to 2.64 Å. The minimum energy structure for the anionic trimer is linear as in case of the neutral cluster. However the average bond length is elongated (2.55 Å for the neutral cluster vs. 2.58 Å for the anionic). For Au_4^- the minimum energy structure is a "zig-zag" one which was first reported by Häkkinen and Landman.[1] They found this structure to be degenerate with the planar Y-shaped structure. However, in our case, the Y-shaped structure yielded a negative frequency and hence is not considered in the present discussion.

For Au_5^- the minimum energy structure is a "W" in agreement with the results of other workers.[16] The binding energy for this structure is 1.81 eV. The minimum energy Au_6^- structure is obtained by adding a triangular motif to the "W-shaped" structure for Au_5^-. The resulting structure is the same planar triangular one as obtained for Au_6 and Au_6^+. However, in this case the HOMO-LUMO gap is quite small, only 0.259 eV indicating that it is highly unstable. The structure lying next
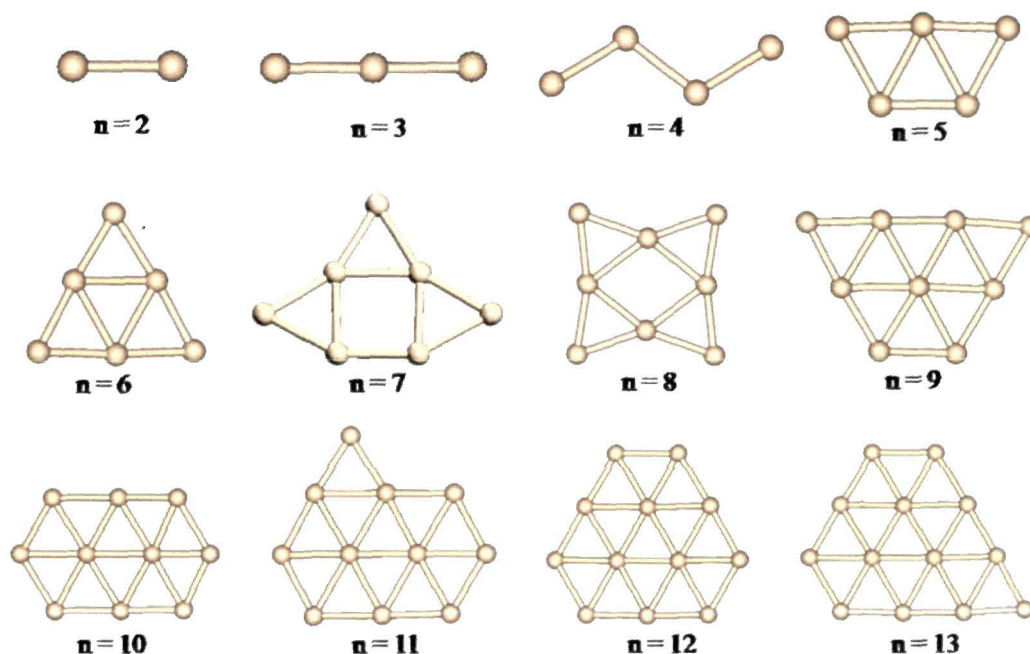
Figure 3.3. The calculated structures of anionic gold clusters (Au_n^-, n = 2 to 13) at BLYP/DNP level of calculations.

higher in energy is a zig-zag one, with the energy difference between this structure and the triangular structure being 0.62 eV. In case of the neutral cluster, this structure has the highest energy. For Au_7^- the minimum energy structure is a tri edge capped square. This structure has not been obtained for neutral and cationic clusters. It has also been obtained as the minimum energy structure for singly charged anionic Au_7^- cluster by Remacle *et al.*[17] The other structures obtained include a face capped octahedron, an extended W and a hexagon. The minimum energy structure of Au_8^- is the same tetra edge capped rhombus structure as obtained for the neutral and cationic clusters. The per atom binding energy for this anionic cluster is 2.035 eV while for the cationic cluster it is 2.199 eV. The Au_9^- cluster presents the bi-edge capped hexagon as the minimum energy structure. For the neutral cluster this structure lies 0.017 eV higher in energy compared with the minimum energy planar structure. Another capped hexagonal structure was obtained with cappings at different positions. This structure lies 0.189 eV higher in energy. The Au_{10}^- cluster exhibits a tri-capped hexagon as the minimum energy structure. The neutral and the cationic Au_n clusters also have the same minimum energy structure. The minimum energy structures for Au_{12}^- and Au_{13}^- are a penta capped hexagon and a hexa capped

hexagon, respectively which are similar to the minimum energy structures of the neutral and cationic clusters of the same size.

Table 3.5. Binding energy/atom, second differential of binding energy, average Au-Au distance and HOMO-LUMO gap for Au_n^- (n = 2-13) clusters.

n	E_b	$\Delta^2 E_b$	Average Bond Length(Å)	HOMO-LUMO gap
2	1.001		2.64	0.523
3	1.646	0.635	2.58	1.983
4	1.656	-0.145	2.68	1.676
5	1.811	0.083	2.71	1.141
6	1.884	-0.052	2.68	0.259
7	2.008	0.097	2.68	1.167
8	2.035	-0.030	2.68	0.867
9	2.093	0.057	2.71	0.785
10	2.093	-0.055	2.72	0.139
11	2.148	0.033	2.72	0.956
12	2.171	0.001	2.72	0.256
13	2.192		2.72	0.293

Energies are in eV.

3.3.2 Variation of average Au-Au bond length

In order to compare the variation of average Au-Au bond length of Au_n clusters with the increase of cluster size we choose the most stable structure for each of the neutral, cationic and anionic clusters. The variation of average Au-Au bond length of all the lowest energy structures as a function of cluster size is shown in Figure 3.4.
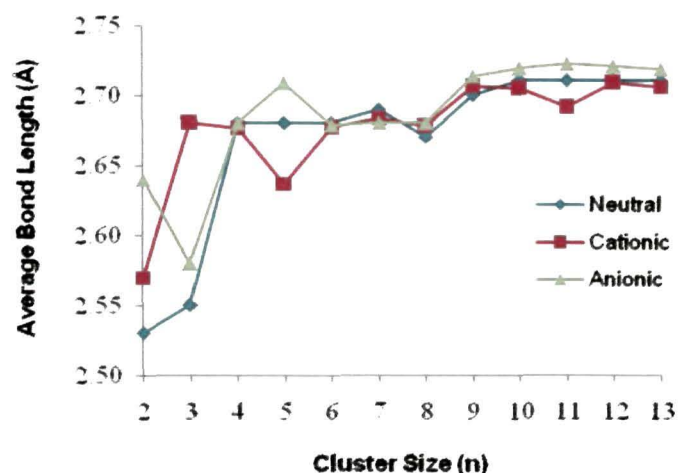
Figure 3.4. Variation of average bond length with respect to cluster size.

The average bond length of neutral and anionic Au_n clusters increases as we go from $n = 2$ to $n = 4$. For the cationic cluster the average bond length is higher for Au_3^+ compared to Au_2^+ and Au_4^+. This may be attributed to the fact that Au_3^+ being triangular, there is a change of geometry from linear to triangular at $n = 3$ which is not the case for neutral and anionic clusters. For system sizes of 4 and 6 atoms, the average bond lengths for neutral, cationic and anionic clusters are exactly the same. The Au_5^+ cluster shows a decrease in the average bond length which is not observed in case of the neutral and anionic clusters. This may be due to the different geometry exhibited by Au_5^+ compared to Au_5 and Au_5^-. For system sizes of 6 to 8 atoms the average bond length remains the same for cationic and anionic clusters, while for neutral cluster there is a slight increase at Au_7. The curve for the neutral cluster shows a dip at Au_8 which has a capped rhombus structure. The most stable rhombus structure of Au_4 has the similar Au-Au bond lengths. For the neutral and charged clusters there is a marked increase in the average Au-Au bond length on going from a system size of 8 to 9 atoms. For system sizes of 10 to 13 atoms, the average bond lengths remain constant for neutral and anionic clusters with the anionic clusters exhibiting slightly longer Au-Au bond lengths. For the cationic cluster there is a slight decrease at Au_{11}^+. The variation of average Au-Au bond lengths with cluster size in our calculations is at variance with some researchers. This is mainly due the different values of system size, n, at which 2D-3D crossovers are reported. For instance, Wang *et al.*[14] reported the onset of three dimensional structure for neutral clusters to occur at $n = 7$. On the other hand, all the minimum energy structures for neutral and charged clusters in our calculations are planar.

3.3.3   Binding energy and relative stability

The binding energy values for all the neutral Au_n ($n = 2-13$) clusters are given in Table 3.3 while those for the minimum energy cationic and anionic clusters are given in Tables 3.4 and 3.5, respectively. Our calculated binding energies for neutral clusters are lower than those reported by Wang *et al.*[14] using DFT-LDA methods. However, it is known that GGA underestimates the binding energy by 0.3–0.4 eV/atom with respect to LDA based values.[8] As a comparison, our GGA calculation yields a value 1.102 eV/atom for Au_2 as against a value of 1.22 eV/atom[14] by DFT-LDA methods. Our calculated binding energy is in very good

agreement with the experimental value of 1.15 eV/atom.[29]   The variation of calculated binding energy per atom (E_b) of the most stable neutral, cationic and anionic structure for each cluster as function of cluster size is shown in Figure 3.5. As can be seen from the plot, the per atom binding energy increases with cluster size for all clusters.   The curve for the neutral cluster exhibits a local maximum at Au_6 in agreement with the results of Häkkinen and Landman,[1] Xiao and Wang[15] and Bonačić-Koutecky and coworkers.[36]   This indicates that triangular Au_6 is more stable than its neighbours.   Our results for the cationic clusters are in good agreement with those of Walker.[4]
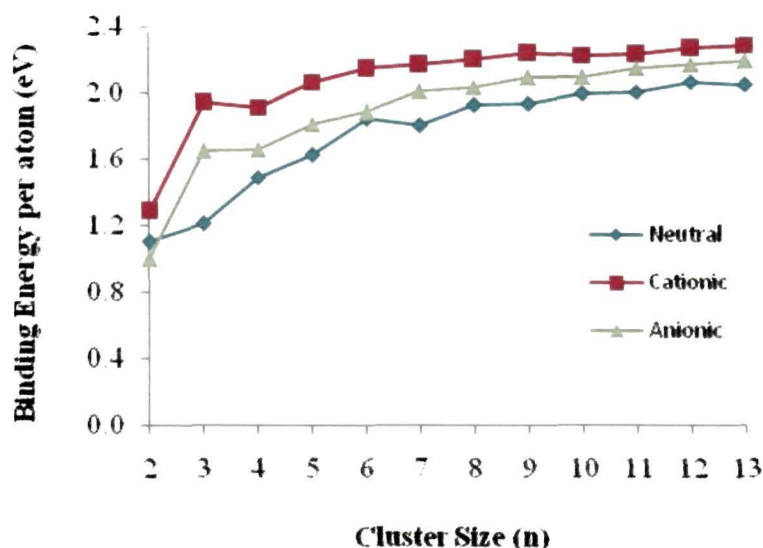
Figure 3.5. Variation of binding energy per atom with respect to cluster size.

The increase of $E_b(n)$ with n indicates the greater stability as the cluster grows in size.   This may be due to the fact that with increasing cluster size, the average number of nearest neighbours increases, which promotes greater average number of interactions per atom.   For the same cluster size, binding energy can be used to determine the relative stability of the isomers.[5]

In order to analyze the stability and size-dependent properties of gold clusters, we also calculated fragmentation energies, *D(n,n-1)*, using equation 3.3 and second differences in binding energy, $\Delta^2 E_b$ using equation 3.4 as defined in the methods section.   The fragmentation energies are sensitive to the relative stabilities that can be observed in mass abundance spectra.   Figure 3.6 shows *D(n,n-1)* of neutral gold clusters which oscillate with cluster size.   The peaks in the plot indicate that the

clusters with even number of atoms are more stable than those with odd number of atoms. The fragmentation energy value for the most stable Au_6 triangular cluster has the highest value of 2.94 eV indicating high stability of triangular Au_6 cluster. Figure 3.7 shows the variation of the second differential of binding energy per atom with cluster size n.
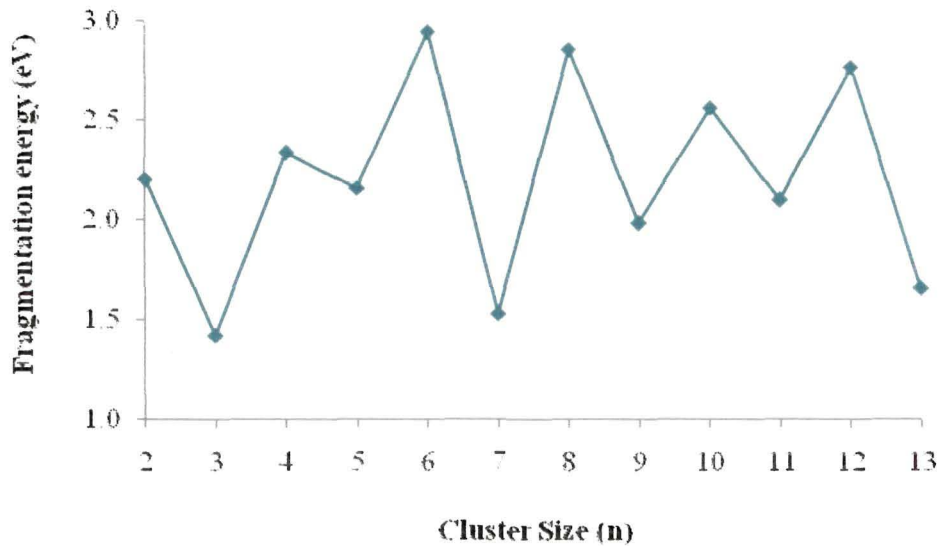
Figure 3.6. Variation of fragmentation energy of neutral clusters with respect to cluster size.
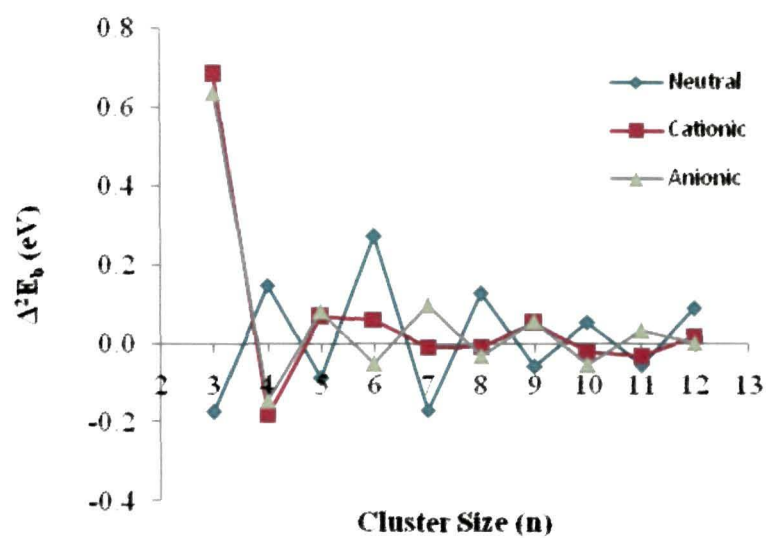
Figure 3.7. Variation of second energy differential of binding energy per atom with cluster size

In cluster physics, the quantity $\Delta^2 E_b$ is commonly known to represent the relative stability of a cluster of size n with respect to its neighbours.[1,5] The plots shows an odd-even oscillation with the even-numbered neutral and odd-numbered charged clusters having larger $\Delta^2 E_b$ values. This indicates that even-numbered Au_n clusters and odd-numbered $Au_n^{\pm}$ clusters are relatively more stable than the neighbouring odd-numbered and even-numbered ones, respectively. Cationic clusters exhibit $\Delta^2 E_b$ values nearly same as those for anionic clusters except for system sizes 6, 7 and 11. The odd-even oscillations for anionic clusters are more pronounced than those for cationic clusters. Among all the minimum energy structures, triangular Au_6 has the largest $\Delta^2 E_b$ value of 0.272 eV/atom, indicating its high stability.

3.3.4 HOMO-LUMO gap

The energy gap between the highest occupied molecular orbital (HOMO) and the lowest unoccupied molecular orbital (LUMO) for each stable neutral cluster and those of the minimum energy charged clusters has been calculated. A large HOMO-LUMO gap has been considered as an important requisite for the chemical stability of gold clusters.[39] The HOMO-LUMO gaps for the neutral clusters are shown in Table 3.3 while those for the charged clusters are given in Tables 3.4 and 3.5, respectively.

The variation in the HOMO-LUMO gap for the most stable structures for each cluster size is shown in Figure 3.8. As seen from the plot, the HOMO-LUMO energy gap shows an odd-even oscillation for n > 4. For neutral clusters the even-numbered clusters have larger HOMO-LUMO gap and are relatively more chemically stable than the odd numbered neighbours. Odd-even alterations in the HOMO-LUMO gap values have often been predicted by earlier calculations for other small metal clusters[40,41] as also for small Au_n clusters.[2,18,42] Most importantly, HOMO-LUMO gaps evaluated from photoelectron spectroscopy (PES) data of gold cluster anions have also shown oscillations.[43] Odd-even oscillation behaviors can be understood by the effect of electron pairing in orbitals. Even-sized neutral clusters have an even number of s valence electrons and a doubly occupied HOMO, while it is singly occupied for odd-sized clusters. The electron in a doubly occupied HOMO feels a stronger effective core potential due to the fact that the electron screening is

weaker for electrons in the same orbital than for inner-shell electrons. Our pattern of HOMO-LUMO gap for neutral clusters is in good agreement with that obtained by Wang *et al.*[14] The HOMO-LUMO gap is particularly large for Au_2, Au_6 and Au_8 in agreement with other theoretical studies.[1,4,18] The anionic clusters show odd-even alternations in the HOMO-LUMO gap with exceptions at n = 4 and n = 9. The odd numbered clusters have larger HOMO-LUMO gaps compared to the even numbered ones indicating their greater stability. This is in agreement with the results of Häkkinen and Landman.[1] Oscillations in the HOMO-LUMO gap for the cationic clusters are not so pronounced.
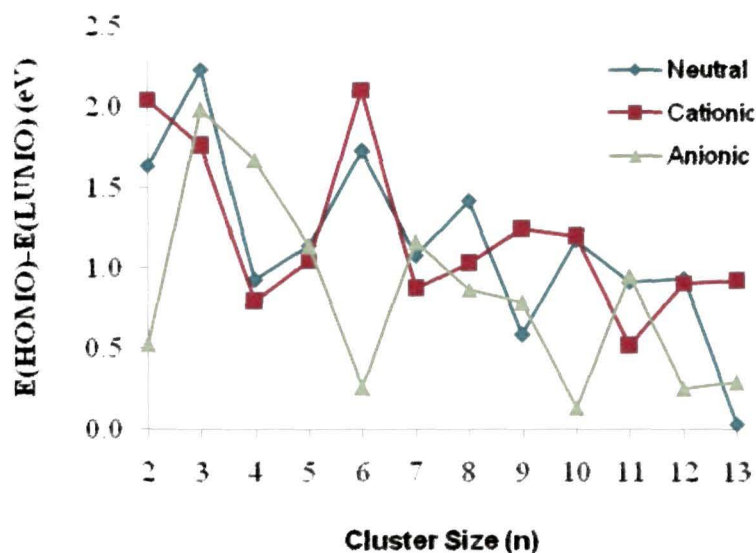
Figure 3.8. Variation of HOMO-LUMO gap with cluster size

1.3 3.3.5 Ionization potential, electron affinity and chemical hardness

In cluster science, ionization potential is used as an important property to study the change in electronic structure of the cluster with size. We have calculated the vertical ionization potential of all the stable structures. This has been obtained from consideration of the total energies of the neutral cluster and the cationic cluster at the geometry of the neutral cluster. We compare our values of ionization potential with experimental results. For linear chain trimer, our value (8.75 eV) is larger compared to the experimental value (7.50 eV).[44] Wang *et al.*[14] have determined an even higher value for the first vertical ionization potential of the linear trimer (9.05

eV). However, for the Au$_3$ triangle, our value of ionization potential (7.42 eV) compares well with the experimental value (7.50 eV).[44] This may indicate that for Au$_3$, the linear chain, which is only 0.052 eV lower in energy than the triangle is not much stable than the triangular structure. For W shaped Au$_5$ cluster, our value of ionization potential (7.79 eV) is very close to the experimental value (8.0 eV).[44] For triangular Au$_6$, the difference between our value (7.84 eV) and the experimental value (8.8 eV) is large. In Figure 3.9, the calculated ionization potentials of the minimum energy structures as a function of cluster size have been plotted. The plot shows even-odd alternative behaviour. The even-sized clusters with an even number of *s* valence electrons have larger values of ionization potential compared to their immediate neighbours. This is in agreement with previous studies.[1,2]
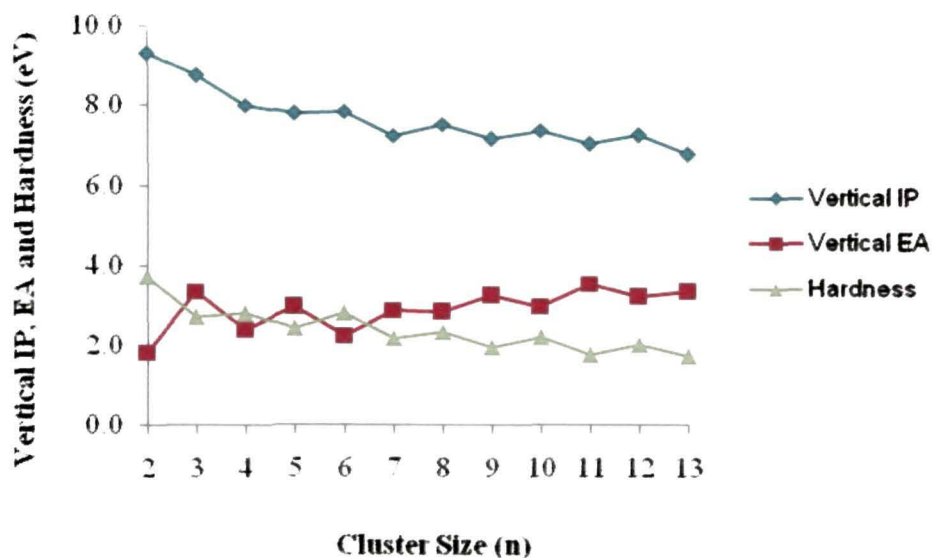
Figure 3.9. Variation of IP, EA and chemical hardness of neutral clusters with cluster size

Similar to ionization potential, we calculated vertical electron affinity values for all the minimum energy structures. We have also calculated the chemical hardness of all the stable structures based on finite difference approximation. The variation of vertical electron affinity and chemical hardness with cluster size are plotted in Figure 3.9. The vertical electron affinity values also show an odd-even alternating behaviour; but in this case, the nature is opposite to that of ionization potential. The odd-sized clusters have higher value of electron affinity compared to the even-sized ones. The chemical hardness values also show an oscillating behaviour as the

cluster size increases. The odd-even oscillation of the chemical hardness indicates that the even numbered gold clusters with higher hardness are more stable than their neighbouring odd-numbered clusters. It is to be noted that our Au_n clusters were generated by systematically adding an atom to the Au_{n-1} cluster. However, in case of large clusters as the number of possible structures increases this method may lead to missing out on some of the possible minima. Techniques like genetic algorithm (GA) and simulated annealing (SA) serve as efficient methods for generating all possible structures on the potential energy surface thereby leading to the global minimum.

2.4. Conclusions

We have investigated low-energy geometries, binding energy, relative stability, HOMO-LUMO gap and chemical hardness of neutral Au_n and charged $Au_n^{\pm}$ clusters, n varying from 2 to 13 using BLYP/DNP level of theory. Different initial guess geometries were considered for all the clusters which led to a number of structural isomers for each cluster size. Of these isomers, twelve structures were not reported previously. The minimum energy structures for all the neutral and charged clusters are found to be planar with coexistence of 3D structures for neutral Au_4 and Au_6 clusters within the DFT error. It is observed that some of our minimum energy structures obtained by using AER method are different from those reported with ECP calculations. Odd-even alterations are evident in the HOMO-LUMO gaps, chemical hardness, second energy difference of binding energy and fragmentation energy. Even-n neutral clusters and odd-n charged clusters are found to be relatively more stable compared to the odd-n and even-n ones, respectively indicating that electron spin-pairing stabilizes these clusters. The calculated results agree well with available experimental data and some of the earlier theoretical investigations of gold nanoclusters. From the considerations of fragmentation energy, second difference of binding energy, HOMO-LUMO gap, vertical ionization potential and chemical hardness it is found that the triangular Au_6 neutral cluster is highly stable. The systematic investigations of structural and electronic properties of small gold clusters present in this study will provide an insight into understanding more complicated gold clusters and clusters of other metals.

References

[1] Häkkinen, H.; Landman, U. Gold clusters Au_n ($2 \leq n \leq 10$) and their anions. *Phys. Rev. B* **62**, R2287-R2290 (2000).

[2] Häkkinen, H. *et al.* On the electronic and atomic structures of small Au_n^- (n = 4-14) clusters: a photoelectron spectroscopy and density-functional study. *J. Phys. Chem. A*, **107**, 6168-6175 (2003).

[3] Yoon, B.; Häkkinen, H.; Landman, U., Interaction of O_2 with gold clusters: molecular and dissociative adsorption. *J. Phys. Chem. A*, **107**, 4066-4071 (2003).

[4] Walker, A. V. Structure and energetics of small gold nanoclusters and their positive ions. *J. Chem. Phys.*, **122**, 094310-094321 (2005).

[5] Zhao, J.; Yang, J.; Hou, J. G. Theoretical study of small two-dimensional gold clusters. *Phys. Rev. B*, **67**, 085404-085409 (2003).

[6] Furche, F. *et al.* The strucutures of small gold cluster anions as determined by a combination of ion mobility measurements and density functional calculations. *J. Chem. Phys.*, **117**, 6982-6990 (2002).

[7] Cleveland, C. L. *et al.* Structural evolution of small gold nanocrystals: the truncated decahedral motif. *Phys. Rev. Lett.*, **79**, 1873-1876 (1997).

[8] Häberlen, O. D.; Chung, S.-C., Stener, M.; Rösch, N. From clusters to bulk: a relativistic density functional investigation on a series of gold clusters Au_n, n = 6,.......,147. *J. Chem. Phys.*, **106**, 5189-5201 (1997).

[9] Garzón, I. L.; Posada-Amarillas, A. Strucutral and vibrational analysis of amorphous Au_{55} clusters. *Phys. Rev. B*, **54** 11796-11802 (1996).

[10] Garzón, I. L. *et al.* Lowest energy structures of gold nanoclusters. *Phys. Rev. Lett.*, **81**, 1600-1603 (1998).

[11] Michaelian, K.; Rendon, N.; Garzón, I.L. Structure and energetics of Ni, Ag and Au nanoclusters. *Phys. Rev. B*, **60**, 2000-2010 (2000).

[12] Wilson, N. T.; Johnston, R. L. Modelling gold clusters with an empirical many-body potential. *Eur. Phys. J. D*, **12**, 161-169 (2000).

[13] Soler, M.; Garzón, I. L.; Joannopoulos, J. D. Structural pattern of unsupported gold clusters. *Solid State Commun.*, **117**, 621-625 (2001).

[14] Wang, J.; Wang, G.; Zhao, J., Density-functional study of Au_n (n = 2-20) clusters: Lowest-energy structures and electronic properties. *Phys. Rev. B*, **66**, 035418-035423 (2002).

[15] Xiao, L.; Wang, L. From planar to three-dimensional structural transition in gold clusters and the spin-orbit coupling effect. *Chem. Phys. Lett.*, **392**, 452-455 (2004).

[16] Sankaran, M.; Viswanathan, B. A DFT study of the electronic property of gold nanoclusters (Au$_x$, x= 1-12 atoms). *Bull. Catal. Soc. India*, **5**, 26-32 (2006).

[17] Remacle, F.; Kryachko, E. S. Structure and energetics of two- and three-dimensional neutral, cationic and anionic gold clusters Au$_{5 \leq n \leq 9}{}^Z$(Z=0,±1). *J. Chem. Phys.*, **122**, 044304-044317 (2005); Small gold clusters Au$_{5 \leq n \leq 8}$ and their cationic and anionic cousins. *Adv. Quantum Chem.*, **47**, 423-464 (2004).

[18] Soler, J. M. *et al.* Metallic bonding and crystal structure. *Phys. Rev. B*, **61**, 5771 – 5780 (2000).

[19] Li, X-B.; Wang, H-Y.; Yang, X-D.; Zhu, Z-H.; Tang, Y.-J. Size dependence of the structures and energetic and electronic properties of gold clusters. *J. Chem. Phys.*, **126**, 84505-084512 (2007).

[20] Hohenberg, P.; Kohn, W. Inhomogeneous electron gas. *Phys. Rev.*, **136**, B864-B871 (1964).

[21] Kohn, W.; Sham, L.J. Self-consistent equations including exchange and correlation effects. *Phys Rev*, **140**, A1133-A1138 (1965).

[22] Becke, A. D. Density-functional exchange-energy approximation with correct asymptotic behavior. *Phys. Rev. A*, **38** 3098-3100 (1988).

[23] Lee, C.; Yang, W.; Parr, R. G. Development the Colle-Salvetti correlation-energy formula into a functional of the electron density. *Phys. Rev. B* **37**, 785-789 (1988).

[24] Bonačić-Koutecký,V. *et al.* Density functional study of structural and electronic properties of bimetallic silver-gold clusters: comparison with pure gold and silver clusters. *J. Chem. Phys.*, **117**, 3120-3121 (2002).

[25] Delly, B.; Ellis, D. E. Efficient and accurate expansion methods for molecules in local density models. *J. Chem. Phys.*, **76**, 1949-1960 (1982).

[26] Orita, H.; Itoh N.; Inada, Y. All electron scalar relativistic calculations on adsorption of CO on Pt(111) with full-geometry optimization: a correct estimation for CO site-preference. *Chem. Phys. Lett.*, **384**, 271-276 (2004).

[27] Delly, B. An all-electron numerical method for solving the local density functional for polyatomic molecules. *J. Chem. Phys.*, **92**, 508-517 (1990).

[28] Fukui, K.,Role of frontier orbitals in chemical reactions. *Science*, **218**, 747-754 (1982).

[29] Bishea, G. A.; Morse, M. D. Spectroscopic studies of jet-cooled AgAu and Au_2. *J. Chem. Phys.*, **95**, 5646-5659 (1991).

[30] Morokuma, K. New challenges in quantum chemistry: quests for accurate calculations for large molecular systems. *Phil. Trans. Roy. Soc. London A*, **360**, 1149-1164 (2002).

[31] Morse, M. D. Clusters of transition-metal atoms. *Chem. Rev.*, **86**, 1049-1109 (1986).

[32] Lide, D. R. (Ed.) *CRC Handbook of Chemistry and Physics*, CRC, Boca Raton, 2003.

[33] Wessendrup, R.; Hunt, T.; Schwedtfeger, P. Relativistic coupled cluster calculations for neutral and singly charged Au_3 clusters. *J. Chem. Phys.*, **112** 9356-9362 (2000).

[34] Balasubramanian, K.; Liao, M. Z. CAASCF/CI calculations of low-lying states and potential energy surfaces of Au_3. *J. Chem. Phys.*, **86**, 5587-5590 (1987).

[35] Ray, A. K. On the electronic structures of the gold tetramer clusters. *Comp. Mat. Sci.*,**25**, 279-284 (2002).

[36] V. Bonačić-Koutecký, V; P. Fantucci P.; Koutecký, J. Quantum chemistry of small clusters of elements of groups Ia, Ib and IIa: fundamental concepts, predictions and interpretations of experiments. *Chem. Rev.*, **91**, 1035-1108 (1991).

[37] Gilb, S.; Weis, P.; Furche, F.; Ahlrichs R.; Kappes, M. M. Structures of small gold cluster cations (Au_n^+, n<14): ion mobility measurements versus density functional calculations. *J. Chem. Phys.*, **116**, 4094-4101 (2002).

[38] Fernández, E. M.; Soler, J. M.; Garzón, I. L.; Balbas, L. C. Trends in the structure and bonding of neutral and charged noble metal metal clusters, *Int. J. Quantum Chem.*, **101**, 740-745 (2005).

[39] Li, J.; Li, X.; Zhai H. J.; Wang, L. S. Au_{20}: a chip off the old block. *Science*, **299**, 864-867 (2003).

[40] Wang, J.; Wang G.; Zhou, J. Structure and electronic structures of Ge$_n$ (n = 2-25) clusters from density-functional theory. *Phys. Rev. B*, **64** 205411-205415 (2001).

[41] Zhao, J.; Luo, Y.; Wang, G. Tight-binding study of structural and electronic properties of silver clusters. *Eur. Phys. J. D*, 14, 309-316 (2001).

[42] Grunwaldt, J.-D.; Baiker, A. Gold/titania interfaces and their role in carbon monoxide oxidation. *J. Phys. Chem. B*, **103** 1002-1012 (1999).

[43] Taylor, K. J.; Pettiette-Hall, C. L.; Cheshnovsky O.; Smalley, R. E. Ultraviolet photoelectron spectra of coinage metal clusters. *J. Chem. Phys.*, **96**, 3319-3329 (1992).

[44] Jackschath, C.; Rabin, I.; Schulze, W. Electron impact ionisation potentials of gold and silver clusters Me$_n$, n $\leq$ 22. *Ber. Bunsenges Phys. Chem.*, 86 1200-1204 (1992).

[45] Pyykkö, P. Theoretical chemistry of gold. *Angew. Chem. Int. Ed.* **43**, 4412-4456 (2004).

CHAPTER   4

Reactivity of Gold Nanoclusters from Conceptual Density Functional Studies

As determined from electronic structure studies in the previous chapter, the planar triangular Au_6 cluster is found to be highly stable. Reactivity studies are carried out on various isomers of this cluster in the neutral and singly charged cationic and anionic forms using DFT based local reactivity descriptors, viz, Fukui function for nucleophilic attack, f^+ Fukui function for electrophilic attack f^-, relative nucleophilicity f^-/f^+ and relative electrophilicity f^+/f^-. Based on these parameters we are able to identify unique atoms in these clusters and predict the probability of electrophilic and nucleophilic attacks at various sites. From these studies it is predicted that in case of the triangular Au_6 cluster the CO molecule is most likely to be adsorbed at the apex site, while O_2 prefers the mid site. In addition, reactivity parameters at various sites of the minimum energy cationic, neutral and anionic Au_n clusters (n = 2-13) are also determined.

4.1 Introduction

Due to the wide application of gold nanoclusters as catalysts in several industrially important reactions, a lot of studies, both theoretical[1-3] and experimental,[4-8] have been undertaken to determine the structural and electronic properties of clusters in the gas phase as well as on support and to examine their interaction with adsorbates.[9-15] While most of the studies on the catalytic properties of gold clusters focus on the structure and energetics of the adsorption complexes, the mechanism of interaction and prediction of reaction pathways, very less attention

has been given to probe the reactivity of various active sites within a cluster and to predict the most reactive site. Such studies are important because the activity of clusters has been found to depend upon the type of sites exposed to the reactants and their ability to absorb and donate electrons. It is here that density functional theory based reactivity descriptors come in handy. Local reactivity descriptors like Fukui function for nucleophilic attack f^+, Fukui function for electrophilic attack f^-, relative nucleophilicity f^-/f^+ and relative electrophilicity f^+/f^- are used to describe relative reactivity within a molecule which aids in determining the site selectivity in chemical reactions. Pal and co-workers have used density functional theory based local reactivity descriptors to determine the reactivity of gold nanoclusters.[16,17] Recently a DFT based reactivity study of $^1Au_6Pt$ clusters have been undertaken by David et al.[18]

In this work we investigate the reactivity at different sites of several low energy isomers of the highly stable planar triangular Au_6 cluster in the neutral, cationic and anionic forms. Our investigation also includes the minimum energy $Au_n^{0,\pm}$ (n=2-13) clusters. To the best of our knowledge, this is the first study on the reactivity of charged species.

4.2   Computational Details

Fukui function $f(\vec{r})$, as defined by Parr and Yang,[19,20] is a mixed second derivative of energy of the system with respect to the number of electrons N and constant potential $v(\vec{r})$:

$$f(\vec{r}) = \left(\frac{\partial^2 E}{\partial N \partial v(\vec{r})} \right) = \left[\frac{\delta \mu}{\delta v(\vec{r})} \right]_N = \left(\frac{\partial \rho(\vec{r})}{\partial N} \right)_{v(\vec{r})} \tag{4.1}$$

where $\rho(\vec{r})$ represents the electron density at position $\vec{r}$ of the chemical species. Fukui function expresses the sensitivity of the chemical potential of a system to an external perturbation. Higher the value of Fukui function at a particular site, more is its reactivity. In order to describe the reactivity of an atom in a molecule, it is necessary to condense the values of Fukui function, $f(\vec{r})$ around each atomic site into a single value. The condensed Fukui function for an atom k in a molecule having N electrons can be obtained from the finite difference approximation as

$$f_k^+ = [q_k(N+1) - q_k(N)] \tag{4.2}$$

for nucleophilic attack, and

$$f_k^- = [q_k(N) - q_k(N-1)] \qquad (4.3)$$

for electrophilic attack

where $q_k(N)$, $q_k(N+1)$ and $q_k(N-1)$ are electronic populations on the particular atom k of the molecule with N, $N + 1$ and $N - 1$ electrons, respectively. The 'relative electrophilicity' and 'relative nucleophilicity' values for the particular atom can be obtained from the ratio of Fukui functions f^+/f^- and f^-/f^+, respectively.

Full geometry optimizations are performed at the DFT level without imposing any symmetry constraint. The program package used is DMol^3. Scalar relativistic effects have been incorporated into our all electron calculations in order to account for gold, which is a heavy atom. Self consistent field procedures are performed with convergence criteria of 1×10^{-5} a.u. on the total energy and 1×10^{-6} a.u. on the electron density. The basis set used is of double numeric quality with polarization functions (DNP). The exchange–correlation functional used is BLYP. The Fukui functions have been calculated on the basis of Hirshfeld population analysis.

4.3 Results and Discussion

4.3.1 Reactivity of cationic, neutral and anionic clusters

We have obtained three optimized geometries for neutral, four for cationic and six for anionic Au$_6$ clusters within the considered energy range of 1 eV from the minimum energy structure. They are shown in Figure 4.1.

The cluster isomers have been arranged in the order of increasing energy. It may be noted that more structures were obtained which were devoid of any negative frequency. But they have not been included here as they lie 1.28-1.38 eV higher in energy compared to the minimum energy planar triangular structure. Based on symmetry and Fukui function values we have identified unique atoms for each cluster. The minimum energy structure of the neutral Au$_6$ cluster is planar triangular with three atoms forming an outer triangular structure and the remaining three forming an inner triangle. Both inner and outer triangles are equilateral with Au-Au
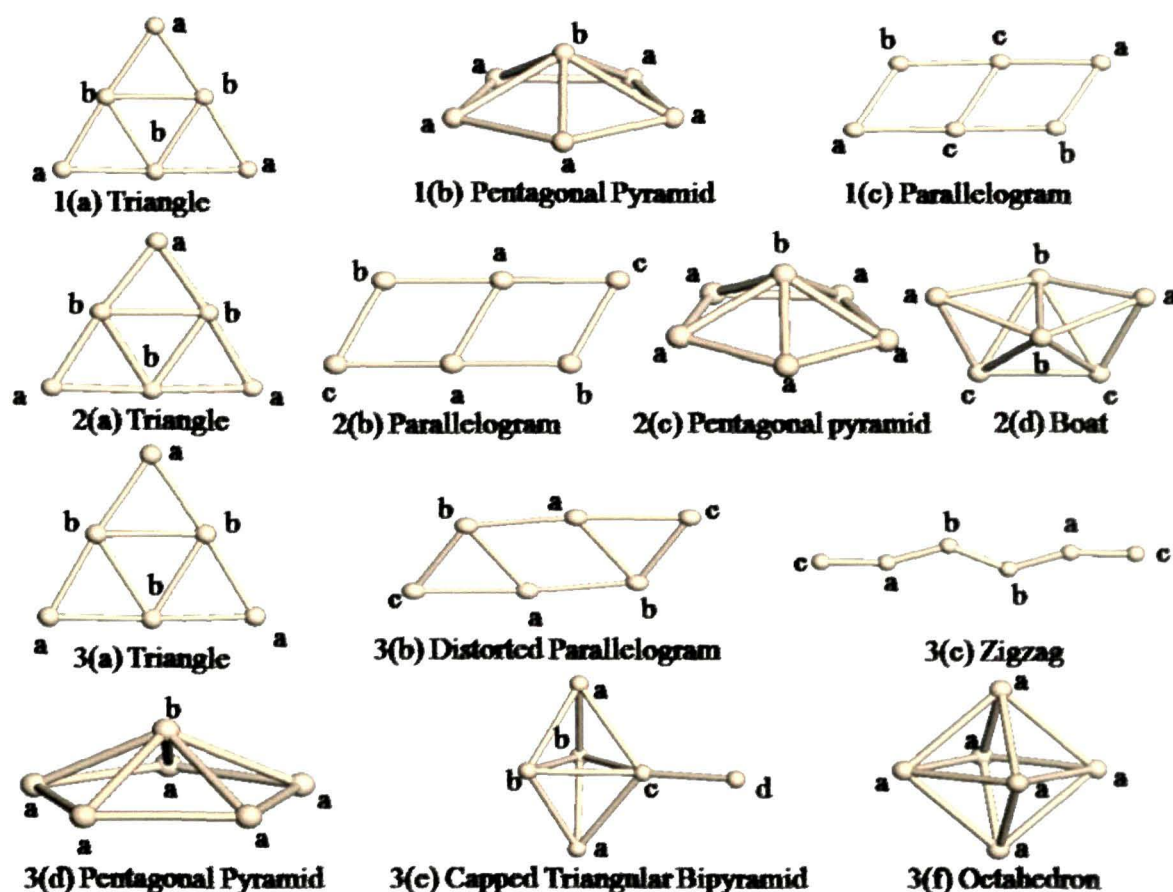
Figure 4.1. Optimized geometries of neutral [1(a),(b),(c)], cationic [2(a),(b),(c),(d)] and anionic [3(a),(b),(c),(d),(e),(f)] Au_6 clusters.

bond distances for the outer triangle being 5.26Å(2×2.63Å) while that of the inner triangle being 2.79Å The edges of the outer triangle are slightly bent at the mid portion where the gold atom of the inner triangle is located with the Au-Au-Au angle having a value of 175.9°. This structure is retained in case of the cationic cluster with the bond lengths and bond angles changing only slightly. Table 4.1 presents the Hirshfeld charges along with the Fukui functions for each unique atom of all the isomers of the neutral and cationic clusters. For the minimum energy triangular structure, no charge is assigned to the unique atoms, thus making it impossible to predict the reactivity of the cluster from the point of view of atomic charges. The value of relative electrophilicity f^+/f^- for the unique atom 'a' for the neutral triangular Au_6 cluster is 1.17 while that of relative nucleophilicity f^-/f^+ is 0.85. The higher value of f^+/f^- compared to f^-/f^+ for this site indicates that it has a

Table 4.1. Hirshfeld charges, Fukui functions, relative electrophilicity and relative nucleophilicity values for unique atoms of neutral and cationic Au_6 clusters.

Structure	ΔE (eV)	Atom type	Charges	f^+	f^-	f^+/f^-	f^-/f^+
neutral							
Triangle	0.00	a	0.00	0.23	0.20	1.17	0.85
		b	0.00	0.10	0.14	0.74	1.34
Pentagonal pyramid	0.92	a	-0.01	0.17	0.18	0.96	1.04
		b	0.07	0.14	0.10	1.36	0.74
Parallelogram	1.00	a	0.00	0.23	0.23	1.00	1.00
		b	0.01	0.16	0.16	1.00	1.00
		c	-0.01	0.11	0.11	1.00	1.00
cationic							
Triangle	0.00	a	0.20	0.21	0.20	1.06	0.94
		b	0.14	0.12	0.14	0.92	1.09
Parallelogram	0.63	a	0.11	0.12	0.12	1.00	1.00
		b	0.17	0.17	0.17	1.00	1.00
		c	0.22	0.22	0.21	1.00	1.00
Pentagonal pyramid	0.80	a	0.17	0.17	0.18	0.97	1.03
		b	0.17	0.13	0.10	1.28	0.78
Boat	0.90	a	0.17	0.18	0.18	1.00	1.00
		b	0.19	0.15	0.14	1.03	0.97
		c	0.15	0.17	0.17	1.00	1.00

high probability of being attacked by nucleophiles like CO, H_2O etc. Similarly the site 'b' is prone to attack by an electrophile. In case of the cationic cluster too, the apex atom 'a' is more likely to be attacked by a nucleophile while the mid atom 'b' prefers an electrophilic molecule like O_2. The other isomers are a pentagonal pyramid and a parallelogram for the neutral cluster and a parallelogram, a pentagonal pyramid and a boat structure for the cationic cluster, respectively. For the neutral cluster, the pentagonal pyramid lies 0.92 eV higher in energy than the

triangular structure. This structure consists of two types of unique atoms, five 'a' type atoms lying at the corners of a regular pentagon and the sixth atom of type 'b' lying above the plane. An analysis of the Fukui functions reveals that site 'a' is prone to attack by an electrophile, while site 'b' has more affinity towards a nucleophile. Hirshfeld charges also support these observations. For the parallelogram, all the atoms are favorable for both electrophilic and nucleophilic attacks. In case of cationic clusters, all the atoms carry positive charge. Thus it is impossible to predict the possibility of electrophilic and nucleophilic attacks from the point of view of charge alone. However, the relative reactivity values presented in Table 4.1 reveal that atom 'b' of the pentagonal pyramid is more likely to be attacked by a nucleophile while 'a' favors an electrophilic attack. For the boat structure site 'b' is favorable for an electrophilic attack, while 'a' and 'c' are prone to both electrophilic and nucleophilic attacks.

We present six structures for the anionic Au_6^- cluster. The minimum energy structure is again planar triangular. The other structures include a distorted parallelogram, a zigzag structure, a pentagonal pyramid, a capped triangular bipyramid and an octahedron. Just as in case of cationic clusters, all atoms of the anionic cluster carry charges of the same sign, negative in this case, thus rendering it impossible to predict the nature of the reactive sites. An analysis based on Fukui function (Table 4.2) shows that for the triangular structure, atom 'a' is a good electrophilic site and atom 'b' is a good nucleophilic site. For the distorted parallelogram atoms 'a' and 'c' are favorable for attack by an electrophilic guest molecule while atom 'b' favors a nucleophile. Site 'b' of the pentagonal pyramid also favors a nucleophilic attack. The high value of f^+ / f^- for site 'c' of the capped triangular bipyramid indicates that this site prefers a nucleophilic attack. This cluster contains two 'b' type atoms favorable for electrophilic attack and two atoms 'c' and 'd' favorable for nucleophilic attack. Thus relative reactivity parameters enable us to predict and compare the reactivities of various sites within a cluster, which may not be possible from the values of atomic charges alone.

Table 4.2. Hirshfeld charges, Fukui functions, relative electrophilicity and relative nucleophilicity values for unique atoms of anionic Au_6 clusters.

Structure	ΔE (eV)	Atom type	Charges	f^+	f^-	f^+/f^-	f^-/f^+
Triangle	0.00	a	-0.24	0.23	0.21	1.06	0.94
		b	-0.10	0.11	0.12	0.88	1.13
Distorted parallelogram	0.18	a	-0.11	0.11	0.12	0.96	1.05
		b	-0.15	0.18	0.16	1.09	0.92
		c	-0.24	0.21	0.22	0.96	1.05
Zigzag	0.63	a	-0.14	0.13	0.12	1.02	0.98
		b	-0.12	0.12	0.12	1.00	1.00
		c	-0.25	0.25	0.26	0.99	1.01
Pentagonal pyramid	0.86	a	-0.18	0.17	0.17	1.00	1.00
		b	-0.09	0.14	0.13	1.09	0.91
Capped triangular bipyramid	0.88	a	-0.18	0.18	0.18	1.00	1.00
		b	-0.14	0.18	0.19	0.97	1.03
		c	-0.06	0.07	0.06	1.10	0.91
		d	-0.31	0.22	0.21	1.05	0.95
Octahedron	0.98	a	-0.17	0.17	0.17	1.00	1.00

4.3.2 Reactivity of minimum energy Au_n (n = 2-13) clusters

This study is extended to include all the minimum energy structures of cationic, neutral and anionic Au_n clusters (n = 2-13). The optimized geometries of minimum energy neutral clusters are shown in Figure 4.2 while their reactivities are presented in Table 4.3. The neutral trimer Au_3 is linear with two kinds of unique atoms. The atoms at the ends of the linear chain are of one kind while that in the middle is the second unique atom. The Hirshfeld charge on the inner atom is negative, while those on the outer atoms are positive. For atom 'a', the relative nucleophilicity value is 1.02 and relative electrophilicity value is 0.98 indicating that
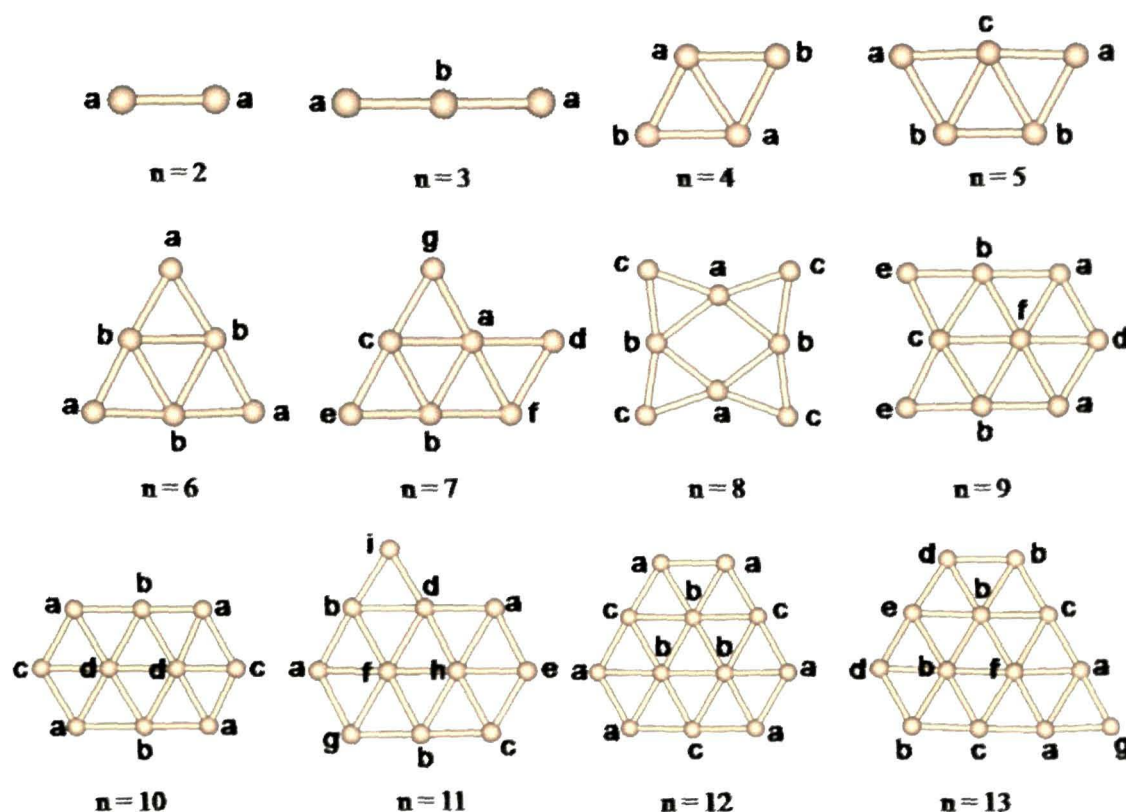
Figure 4.2. Optimized geometries of minimum energy neutral Au_n clusters (n = 2-13).

atom 'a' has the probability of being attacked both by a nucleophile and an electrophile. The unique atom 'b' on the other hand strongly favours a nucleophile. The minimum energy Au_4 cluster is a rhombus with two unique atoms. The atom 'a' of this structure having a higher value of f^-/f^+ favours an electrophile. Atom 'b' prefers a nucleophile. In case of the W-shaped Au_5 cluster, atoms 'a' and 'c' prefer nucleophilic attacks, while 'b' prefers an electrophilic attack. In case of the triangular Au_6 cluster, the outer atoms 'a' favour nucleophilic attack while the atoms of the inner triangle favour electrophilic attack.

Thus on adsorption of a CO molecule onto the triangular Au_6 structure it is most likely that the CO molecule will prefer to sit at the apex 'a' site. Adding an extra atom at the bridge position between an apex and a mid atom of the triangular Au_6 cluster gives the minimum energy Au_7 cluster. The shape is a capped triangle. All the atoms of this structure are unique atoms. The 'd' and 'e' atoms carry negative charge, while all the other atoms carry positive charges. The atoms a, b and f have higher values of f^+/f^- compared to f^-/f^+ and hence are more favourable

for nucleophilic attacks. The remaining atoms 'c', 'd', 'e' and 'g' prefer electrophilic attacks. As discussed in the previous chapter, the Au_8 cluster features the tetra edge capped rhombus as the next higher energy structure. This structure consists of three kinds of unique atoms. The rhombus consists of two kinds of unique atoms, while the outer atoms forming the edge cappings form the third kind. From the relative electrophilicity and relative nucleophilicity values given in Table 4.3 it is observed that the atoms constituting the rhombus have higher values of f^-/f^+ and hence have more affinity towards electrophiles like O_2. The atoms forming the cappings prefer electrophiles.

Table 4.3. Hirshfeld charges, Fukui functions, relative electrophilicity and relative nucleophilicity values for unique atoms of minimum energy neutral Au_n clusters (n = 2-13).

n	Structure	Atom type	Charges	f^+	f^-	f^+/f^-	f^-/f^+
2	Linear	a	0.00	0.50	0.50	1.00	1.00
3	Linear	a	0.01	0.40	0.41	0.98	1.02
		b	-0.02	0.20	0.18	1.10	0.91
4	Rhombus	a	-0.06	0.25	0.28	0.90	1.11
		b	0.06	0.25	0.22	1.12	0.90
5	W	a	-0.01	0.25	0.23	1.07	0.93
		b	0.00	0.18	0.21	0.89	1.12
		c	0.03	0.14	0.13	1.05	0.95
6	Triangle	a	0.00	0.23	0.20	1.18	0.85
		b	0.00	0.10	0.14	0.74	1.34
7	Capped triangle	a	0.02	0.16	0.15	1.07	0.94
		b	0.01	0.19	0.17	1.14	0.88
		c	0.01	0.09	0.09	0.97	1.03
		d	-0.04	0.20	0.22	0.90	1.11
		e	-0.01	0.19	0.20	0.98	1.02
		f	0.03	0.07	0.06	1.03	0.97
		g	-0.03	0.10	0.11	0.94	1.07
8	Tetra edge capped rhombus	a	-0.01	0.07	0.08	0.87	1.15
		b	0.00	0.07	0.08	0.94	1.07
		c	0.00	0.18	0.17	1.04	0.96
9	Bi edge-capped hexagon	a	-0.01	0.13	0.13	1.01	0.99
		b	0.01	0.08	0.08	1.03	0.97
		c	0.01	0.06	0.06	1.02	0.98
		d	-0.02	0.15	0.15	0.98	1.02
		e	-0.02	0.16	0.17	0.99	1.01
		f	0.05	0.05	0.04	1.02	0.98

Table 4.3 continued

n	Structure	Atom type	Charges	f^+	f^-	f^+/f^-	f^-/f^+
10	Tri capped hexagon	a	-0.02	0.13	0.13	0.98	1.02
		b	0.00	0.09	0.08	1.16	0.86
		c	0.11	0.11	0.12	0.91	1.10
		d	0.04	0.04	0.04	1.13	0.89
11	Tetra capped hexagon	a	0.00	0.12	0.11	1.03	0.97
		b	0.00	0.08	0.07	1.03	0.97
		c	-0.02	0.11	0.11	1.01	0.99
		d	0.00	0.04	0.04	0.98	1.02
		e	-0.01	0.12	0.12	1.05	0.95
		f	0.03	0.04	0.04	0.97	1.03
		g	-0.02	0.13	0.14	0.94	1.07
		h	-0.02	0.14	0.15	0.95	1.05
		i	0.04	0.03	0.03	0.97	1.03
12	Penta capped hexagon	a	-0.02	0.12	0.12	1.00	1.00
		b	0.03	0.03	0.03	1.00	1.00
		c	0.00	0.07	0.07	1.01	0.99
13	Hexa capped hexagon	a	-0.01	0.07	0.07	0.99	1.01
		b	0.01	0.03	0.03	1.03	0.97
		c	0.01	0.07	0.07	1.00	1.00
		d	-0.01	0.10	0.10	0.99	1.01
		e	-0.01	0.11	0.11	1.01	0.99
		f	0.03	0.03	0.03	1.00	1.00
		g	-0.02	0.15	0.15	1.01	0.99

The minimum energy Au_9 cluster is a bi edge-capped hexagon formed by cappings two edges of the hexagonal Au_6 cluster. This structure consists of six kinds of unique atoms. As observed from the relative reactivity indices presented in Table 4.3, each unique atom of this cluster is amphiphilic, i.e, they bear the possibility of both electrophilic and nucleophilic attacks. The tri-capped hexagon is the minimum energy structure of the Au_{10} cluster. This structure is formed by capping an atom of the hexagon of the bi edge-capped hexagonal Au_9 cluster. This structure has a higher D_{2h} symmetry. Consequently the number of unique atoms is reduced to four. This structure may also be assumed to be consisting of two hexagons joined side by side, with a small region of overlap between them. The four corner atoms 'a' of this structure are amphiphilic. The edge atoms 'b' and the inner atoms 'd' favour nucleophilic attacks. On the other hand, the corner atoms 'c' prefer electrophilic attacks. For the next cluster size, Au_{11}, features a tetra capped

hexagon as the minimum energy structure. This structure is formed by capping over two atoms of the tri-capped hexagonal Au_{10} cluster. This structure has C_s symmetry and has nine unique atoms. Unique atoms 'c' and 'd' are amphiphilic. Of the other unique atoms, 'a', 'b' and 'e' are more favourable for nucleophilic attacks, while the remaining atoms 'f', 'g', 'h' and 'i' prefer electrophilic attacks. The minimum energy Au_{12} cluster is formed by capping over two edge atoms of the minimum energy Au_{11} cluster. The structure is a pentacapped hexagon having D_{3h} symmetry. This structure has three kinds of unique atoms, six corner atoms of 'a' type, three inner atoms of 'b' type and three edge atoms of 'c' type which lie at the centre of the three longer edges of the structure. The reactivity indices are indicative of the fact that all the atoms exhibit probabilities of electrophilic and nucleophilic attacks. Thus this structure may prove as a host molecule for reactions involving both oxidation and reduction reactions, for example, CO oxidation which requires the reduction of O_2 and oxidation of the CO molecule. Au_{13} features a hexacapped hexagon as the minimum energy structure. This structure is built from the Au_{12} pentacapped hexagonal structure by capping a gold atom at the bridge position between two 'a' kind of atoms. This structure with C_s symmetry has seven unique atoms. All the unique atoms except 'b' are amphiphilic. The unique atom 'b' exhibits slight preference for nucleophilic attacks as can be observed from the values of the relative reactivity indices. Thus this Au_{13} cluster may also serve as a good host molecule for CO oxidation.

The geometries of the minimum energy cationic and anionic Au_n clusters (n = 2-13) depicting unique atoms alongwith the tables containing Hirshfeld charges and Fukui functions are given in appendix A.

4.4. Conclusions

In summary, we have determined the reactivity of several isomers of cationic, neutral and anionic gold hexamers and minimum energy neutral Au_n (n = 2-13) clusters using density functional theory based reactivity descriptors. The response of various sites of the clusters towards electrophilic and nucleophilic attacks has been predicted. It is found that for the highly stable planar triangular Au_6 cluster the CO molecule is most likely to be adsorbed at the apex site in case of both neutral and charged clusters.

References

[1] Pyykkö, P. Theoretical chemistry of gold. *Angew. Chem. Int. Ed.*, **43**, 4412-4456, (2004) and references therein.

[2] Walker, A. V. Structure of small gold nanoclusters and their positive ions. *J. Chem. Phys.*, **122**, 094310-1-194310-12 (2005).

[3] Häberlen, O. D.; Chung, S-C.; Stener, M.; Rösch, N. From Clusters to Bulk: A relativistic density functional investigation on a series of gold clusters Au_n, n=6,...,147. *J. Chem. Phys.*, **106**, 5189-5201 (1996).

[4] Haruta, M. Size- and support-dependency in the catalysis of gold. *Catal. Today*, **36**, 153-166 (1997).

[5] Taylor, K.J.; Pettiette-Hall, C. L.; Cheshnovsky, O.; Smalley, R. E. Ultraviolet photoelectron spectra of coinage metal clusters. *J. Chem. Phys.*, **96**, 3319-3329 (1992).

[6] Gilb, S.; Weis, P.; Furche, P.; Alrichs, R., Kappes, M. M. Structure of small gold cluster cations (Au_n^+, n<14): ion mobility measurements versus density functional calculations. *J. Chem. Phys.*, **116**, 4094-4101 (2002).

[7] Aguilar-Guerrero, V.; Gates, B. C. Kinetics of CO oxidation catalyzed by supported gold: a tabular study of the literature. Catal. Lett. **130**, 108-120 (2009).

[8] Huang, W.; Pal, R.; Wang, L-M.; Zeng, X. C.; Wang, L-S. Isomer identification and resolution in small gold clusters. *J. Chem. Phys.*, **132**, 054305-1-034505-5 (2010).

[9] Coquet, R.; Howard, K. L.; Willock, D. J. Theory and simulation in heterogeneous gold catalysis. *Chem. Soc. Rev.*, **37**, 2046-2076 (2008).

[10] Yoon, B.; Hakkinen, H.; Landman, U. Interaction of O_2 with gold clusters: molecular and dissociative adsorption. *J. Phys Chem.*, *A*, **107**, 4066-4071 (2003).

[11] Ferullo, R. M.; Fuente, S. A.; Belelli, P. G.; Castellani, N. J. CO interaction with gold atoms adsorbed on terrace, edge and corner sites of the MgO(100) surface. Electronic structure and vibrational analysis from DFT. *Surf. Science*, **603**, 1262-1269 (2009).

[12] Davran-Candan, T.; Aksoylu, A. E.; Yildirim, R. Reaction pathway analysis for CO oxidation over anionic gold hexamers using DFT. *J. Mol. Catal. A: Chemical*, **306**, 118-122 (2009).

[13] Lyalin, A.; Taketsugu, T. Adsorption of ethulene on neutral, cationic and anionic gold clusters. *J. Phys. Chem. C.*, **114**, 2484-2493 (2010)

[14] Wallace, W. T.; Wyrwas, R. B.; Leavitt, A. J.; Whetten, R. L. Adsorption of carbon monoxide on smaller gold-cluster anions in an atmospheric-pressure flow-reactor: room temperatre and humidity dependence. *Phys. Chem. Chem. Phys.* **7**, 930-937 (2005).

[15] Deka, A.; Deka, R. C.; Choudhury, A. Adsorption of CO on gas phase and zeolite supported gold monomers: A computational study. *Chem. Phys. Lett.*, **490**, 184-188 (2010).

[16] De, H. S.; Krishnamurthy S.; Pal, S. Understanding the reactivity properties of Au_n clusters $(6 \leq n \leq 13)$ using density functional theory based reactivity descriptors. *J. Phys Chem. C*, **114**, 6690-6703 (2010).

[17] De, H. S.; Krishnamurthy S.; Pal, S. Density functional investigation of relativistic effects on the structure and reactivity of tetrahedral gold clusters. *J. Phys. Chem. C*, **113**, 7101-7106 (2009).

[18] David, J.; Guerra, D.; Hadad C. Z.; Restrepo, A. Structure and reactivity of [1]Au_6Pt clusters. *J. Phys. Chem. A*, **114**, 10726-10731 (2010).

[19] Parr, R. G.; Yang G. Density functional approach to the frontier-electron theory of chemical reactivity. *J. Am. Chem. Soc.*, **106**, 4049-4050 (1984).

[20] Yang, W.; Parr, R. G.; Pucci, R. Electron density, Kohn-Sham frontier orbitals, and Fukui functions. *J. Chem. Phys.*, **81**, 2862-2863 (1984).

CHAPTER 5

Adsorption of CO and O_2 on Gas Phase and Zeolite Supported Gold Clusters

Having determined the Fukui functions of some low energy isomers of gold clusters, we attempt to verify the predictions regarding electrophilic and nucleophilic attacks by adsorbing CO and O_2 molecules on the minimum energy cationic, neutral and anionic triangular Au_6 cluster. We also investigate the interaction of carbon monoxide on the gold monomer in three oxidation states 0, +1 and +3 in the gas phase and on faujasite support of nine tetrahedral (9T) zeolite cluster using density functional theory. The gas phase structures of the gold carbonyls are retained on the zeolite support with only a slight change in the O-C-Au bond angle. For the supported cluster the CO vibrational frequency shows a blue shift on going to higher oxidation states. The CO binding energies on the supported gold monomers are 1.01, 1.15 and 1.12 eV in the oxidation states 0, +1 and +3, respectively. For a more realistic representation of the support, the calculations are repeated by taking a larger model of the zeolite having 60 tetrahedral (60T) atoms by using Quantum Mechanics (QM)/Molecular Mechanics (MM) approach. It is found that increasing the size of the support leads to a significant improvement in the CO adsorption energy in case of Au^+.

5.1. Introduction

Catalysis by gold clusters is an important area of research in chemistry, physics and material science. An oft studied process is the adsorption of CO by metal clusters and its subsequent oxidation. Among the transition metals gold plays an important part in such investigations mainly due to its ability to promote such

reactions at low temperatures. Other reactions catalysed by gold clusters include the water-gas shift reaction,[1] epoxidation of propylene[2] and vinyl chloride synthesis.[3] Having determined the triangular Au_6 cluster to be highly stable, we now investigate adsorption of the CO and O_2 molecules on the minimum energy cationic, neutral and anionic Au_6 clusters. This will serve to verify the predictions regarding electrophilic and nucleophilic attacks on these systems obtained on the basis of Fukui functions which have been presented in the last chapter. The co-adsorption of these two molecules on the gold hexamer shall also be studied.

It has been observed that the catalytic activity of gold clusters improve drastically on providing a metal oxide support. The gold-support interface is believed to act as an active site for catalysis. The factors determining the catalytic activity of the nanocluster are size, structure and charge state of the cluster, nature of the support and the cluster support interaction. Phala *et al.*[4] studied the chemisorption of hydrogen and carbon monoxide onto small gold clusters Au_n (n = 1-13) using density functional theory. Yoon *et al.*[5] determined that the Au_8 cluster bound to an oxygen-vacancy F-centre defect of MgO(001) is the smallest cluster that can catalyse the oxidation of CO to CO_2 at temperatures as low as 140 K. The metal carbonyl bond is attributed to a balance between two processes, namely, electron donation from a filled σ orbital of the CO to an empty symmetry compatible metal orbital and back donation from filled d-type metal orbitals to empty π^* orbitals of the CO. Zeolites with adjustable acidic properties having pores and cavities of molecular dimensions form an important class of support for nanoclusters in catalysis. The charged state of the cluster depends upon the concentration of acidic centres in the zeolite which can be modified. This renders it possible to study the effect of varying charge of the cluster on catalytic properties. Fierro-Gonzalez and Gates[6] have synthesized and characterized mononuclear Au^I and Au^{III} complexes in zeolite NaY. They found that under the condition of CO oxidation catalysis at 298 K and 760 Torr the gold remained mononuclear and that the Au^{III} complex is more active as a catalyst compared to the Au^I complex. Simakov *et al.*[7] investigated the influence of Na substitution on oxidation of CO in Y zeolites and found two types of active sites viz, partly charged gold clusters $Au_n^{\delta+}$ for low temperature activity and gold nanoparticles Au_n^0 for high temperature activity. It is thus seen that the oxidation state of the zeolite supported cluster greatly influences its catalytic activity. The gold atom is known to exhibit several oxidation states from -1 to +5

and its $5d^{10}$ shell participates actively in bonding coordination in various compounds.[8,9] To the best of our knowledge there has been no theoretical study on the gold monomer adsorbed on a faujasite zeolite support. In view of the marked influence of the charged state of the gold cluster on its catalytic activity, we investigate the adsorption of the CO molecule on zeolite supported gold monomer in three oxidation states 0, +1 and +3 and compare them with their gas phase counterparts. Further, in order to understand the role of the size of the support on catalytic properties of gold clusters, our study is performed by considering two models of the support, viz, a faujasite zeolite cluster having 9 tetrahedral atoms, which shall be treated quantum mechanically, and a larger faujasite zeolite model having 60 tetrahedral atoms, which shall be treated by the hybrid QM/MM approach as implemented in the program *Gaussian03*.

5.2. Computational Details

For adsorption studies in the gas phase, full geometry optimizations have been performed at the DFT level without imposing any symmetry constraint by incorporating relativistic effects. The program package used is DMol³. The basis set is DNP and exchange–correlation functional used is BLYP in case of CO and O₂ adsorption on the gold hexamer. In case of both gas phase and supported gold monomers, the geometry optimizations were performed by using the VWN functional. Single point calculations were then carried out at the VWN optimized geometry by using the GGA functional BLYP in order to determine energy and other properties. This choice of exchange correlation functional is guided by the fact that LDA functionals give a better description of geometry and GGA functionals are better suited to describe molecular properties in case of zeolite supported metal clusters. Vibrational frequency calculations were carried out at the optimized geometry in order to verify that the obtained structures are global minima on the potential energy surface.

For the first part of the study on zeolite supported gold monomers the framework of zeolite has been modelled with a 9T (T = tetrahedral unit of zeolite) cluster containing the six-member ring and three other Si atoms of the wall of the supercage of faujasite structure which is accessible by metal clusters and adsorbed molecules. Three Si atoms of the six-member ring were isomorphously substituted

by three Al atoms in an alternating sequence according to the Löwenstein rule.[10] The excess negative charges generated due to three Al atoms were compensated by protons forming bridging OH groups with framework oxygen atoms. Three models of the zeolite having different number of compensating protons were used. The neutral atom was adsorbed onto the zeolite cluster having three compensating protons. With two compensating protons the zeolite cluster carried a charge of -1 which was neutralized by adsorbing the gold atom in the +1 state. The third model of the zeolite with no compensating protons bore a charge of -3 which was neutralized by adsorbing Au^{3+}. The free valences of silicon and aluminum atoms were saturated with hydrogen atoms. At first, only Si—H, Al—H and O—H bonds were optimized keeping the position of other atoms fixed at their crystallographic positions.[11] In subsequent calculations, the optimized positions of the terminating hydrogen atoms were held fixed and all other atoms were allowed to relax.

The second part of the study taking the larger faujasite zeolite model with 60T atoms has been undertaken by using the two layer ONIOM (Our-own-N-layered Integrated molecular Orbital + molecular Mechanics) method,[12] as implemented in the *Gaussian03* suite of programs. ONIOM involves a hybrid QM/MM method in which the entire zeolite cluster is divided into two regions, (i) an inner core region which is treated quantum mechanically, and (ii) an outer region which is investigated with the less expensive molecular mechanics. In our case we use DFT to model the QM part and universal force field (UFF) to model the MM part of our system. The inner region consists of 6T sites in which three Si atoms are substituted by Al atoms according to Löwenstein rule.[10] The excess negative charges are compensated by protons. Thus our QM region consists of up to 18 atoms including the compensating protons, the adsorbed Au atom and the CO molecule. The MM region consists of 54 T atoms. For the DFT calculations we use the B3LYP functional[13,14] and the 6-31G(d,p) basis set for on all electrons of H, C, O, Si and Al and the relativistic LANL2DZ pseudopotential[15,16] for the Au atom. It has been found in earlier adsorption studies on FAU and MFI zeolites that ONIOM2 (B3LYP/6-31G(d,p):UFF) gives reasonable values corresponding to experimental results. For structure optimization, we follow the methodology of Joshi et al.[17] All atoms of the outer MM region are kept fixed at the respective crystallographic positions and only the atoms in the core QM region alongwith the adsorbates are allowed to relax during geometry optimization. It is believed that this method leads to proper simulation of the core structure and reduces errors in the force field

parameters. At the boundary of the QM/MM region, link H atoms have been incorporated by replacing the O atoms of the Si–O bonds with H atoms. The Si–H distance has been fixed at 1.47 Å.

In the results to follow, the binding energies are computed as

$$E_B(CO) = - [E_{AuCO} - E_{Au} - E_{CO}]$$ (3.1)

$$E_B(O_2) = -[EAu_{O_2} - E_{Au} - E_{O_2}]$$ (3.2)

in the gas phase

$$E_B(Au^{0,+,3+}) = - [E_{zeolite-Au\ complex} - E_{Au}^{0,+,3+} - E_{zeolite}]$$ (3.3)

for the Au-zeolite complex

$$E_{B-zeo}(CO) = - [E_{zeolite-Au-CO\ complex} - E_{zeolite-Au\ complex} - E_{CO}]$$ (3.4)

for the Au-zeolite-CO complex

In all cases, positive values correspond to exothermic processes.

5.3. Results and Discussion

5.3.1 Adsorption of CO and O₂ on cationic, neutral and anionic Au₆ cluster

We use CO and O₂ as probe molecules in order to study the reactivity at various sites of the minimum energy triangular Au₆ structures. The optimized geometries of the cationic and neutral adsorption complexes are shown in Figure 5.1 while those of the anionic complexes are shown in Figure 5.2. The adsorption complexes have been arranged in the order of increasing energy. This adsorption study on Au₆ clusters is performed at three sites, the apex site, which forms a vertex of the outer triangle, the mid site, which forms a vertex of the inner triangle and a bridge site, which is in between the apex and the mid sites.

It has been found that CO does not adsorb at the bridge site, while O₂ adsorbs at all three sites. For all the three clusters relative reactivity indices predict that the apex atom 'a' is more prone to attack by a nucleophile. We studied the adsorption of the CO molecule at the apex and mid sites of these clusters and found that the adsorption energy at the low coordination apex site is higher than that at the mid site. Thus CO adsorbs more strongly at the apex site. Also the adsorption energy for the cationic cluster is higher than that of the neutral and anionic clusters. These obser-
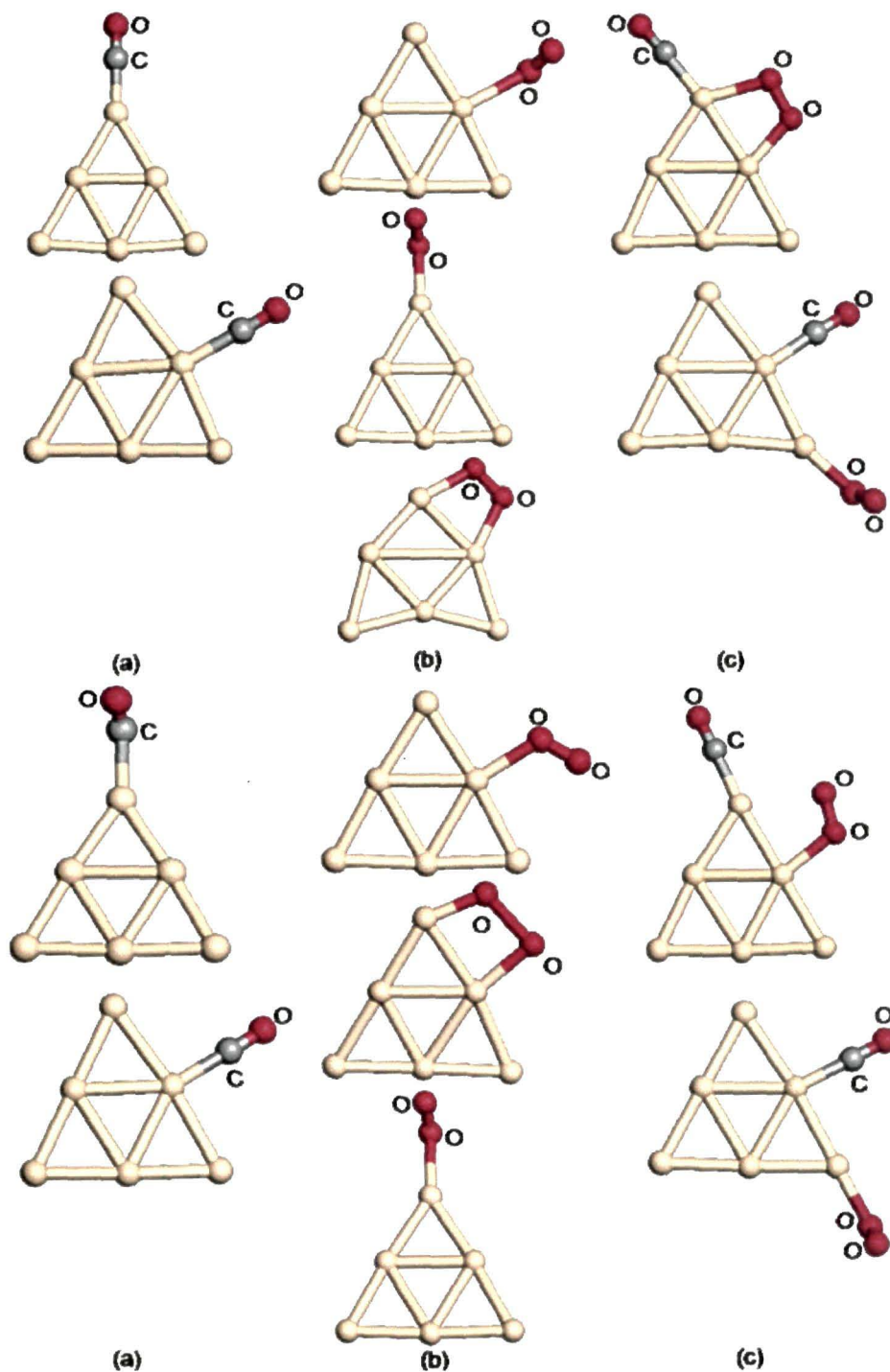
Figure 5.1. Adsorption complexes of the neutral (upper panel) and cationic (lower panel) Au₆ clusters with (a) CO (b) O₂ and (c) CO and O₂ co-adsorbed.

vations are in agreement with previous experimental and theoretical results.[18-20] Then we tried to adsorb O₂ at these sites. As per the predictions obtained from Fukui function analysis, the O₂ atom is more likely to be adsorbed at the mid site for neutral as well as charged clusters. We find that for all the Au₆ clusters adsorption
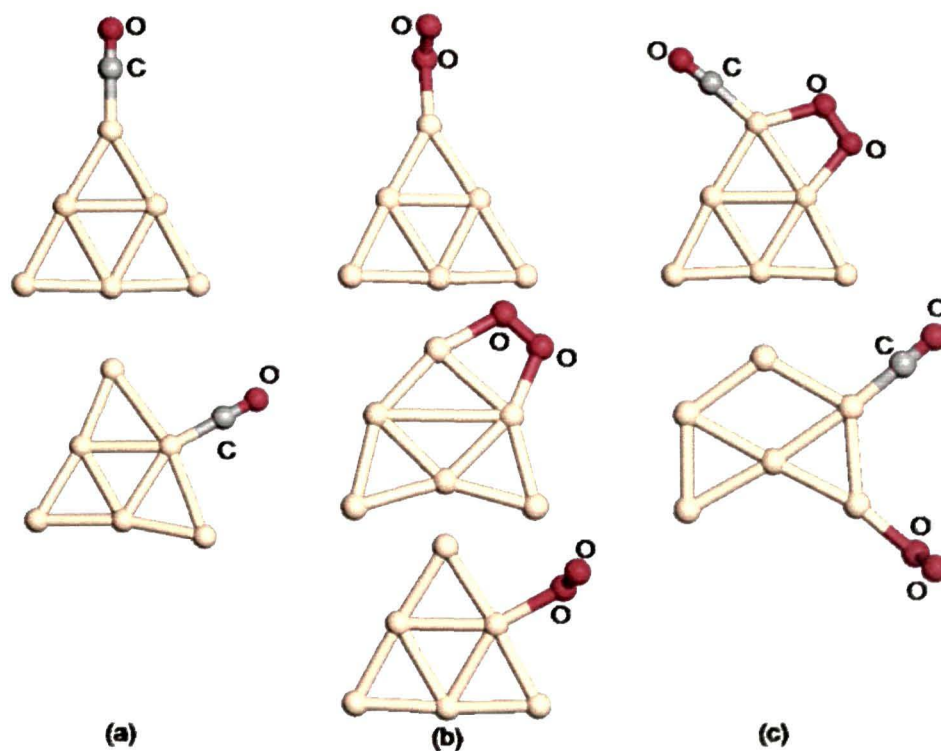
Figure 5.2. Adsorption complexes of anionic Au_6 clusters with (a) CO (b) O_2 and (c) CO and O_2 co-adsorbed.

of O_2 takes place at all three sites. The adsorption energies provided in Table 5.1 indicate that adsorption at the mid site is highly favorable over that at the apex site for neutral and cationic clusters.

Table 5.1. Adsorption energy of CO and O_2 molecules at various sites of the most stable neutral, cationic and anionic Au_6 clusters.

Structure	Adsorption Energy(eV)		
	Neutral	Cationic	Anionic
Au_6CO-apex	1.21	1.37	1.25
Au_6CO-mid	0.69	1.06	0.72
Au_6O_2-apex	0.28	0.26	1.11
Au_6O_2-bridge	0.03	1.01	1.03
Au_6O_2-mid	0.74	1.01	1.06

For the anionic cluster adsorption of O_2 at the apex site is slightly more favourable than that at the mid site. The O_2 adsorption energies at the apex and the

mid sites are 1.11 and 1.06 eV, respectively. The co-adsorption of CO and O_2 is then studied by adsorbing CO at the apex site and O_2 at the mid site and then interchanging their positions. It is found that for both the neutral and charged clusters the adsorption energy of the co-adsorption complex with CO at the apex position and O_2 at the bridge position is higher than that with the adsorbates interchanged (Table 5.2).

Table 5.2. Adsorption energy of CO and (CO+O_2) molecules at various sites of the most stable neutral, cationic and anionic Au_6 clusters when CO and O_2 are adsorbed simultaneously.

Structure	Adsorption Energy CO (eV)		
	Neutral	Cationic	Anionic
$Au_6CO_{apex}O_{2mid}$	1.16	1.49	1.55
$Au_6O_{2apex}CO_{mid}$	0.84	1.21	1.11
	Adsorption Energy (CO+O_2) (eV)		
$Au_6CO_{apex}O_{2mid}$	1.90	2.50	2.61
$Au_6O_{2apex}CO_{mid}$	1.60	2.24	2.98

This observation supports our assignment of electrophilic and nucleophilic sites based on Fukui function which predicts that CO prefers the apex site and O_2 prefers the mid site in Au_6 clusters.

5.3.2 Adsorption of CO on gas phase gold atom

We have performed all electron scalar-relativistic calculations without using any symmetry constraint to study the adsorption of the CO molecule onto the gold monomer in various oxidation states. The optimized structures are given in Figure 5.3. Our optimized geometry of the CO molecule gives a bond length of 1.133 Å, which compares well with the experimental value of 1.128 Å.[21] Our calculations for CO adsorbed on the neutral Au atom reveal a strongly bound molecule (0.88 eV) with a shift of -128.9 cm⁻¹ in the CO vibrational frequency, computed as the difference between the harmonic frequency of AuCO and the free CO molecule. The structure is a bent one with the Au-C-O angle of 149°. The CO bond length elongates to 1.151 Å in keeping with the red shift in the CO vibrational frequency. The Au-C bond length is 1.88 Å. Giordano *et al.*[22] obtained values of the Au-C-O
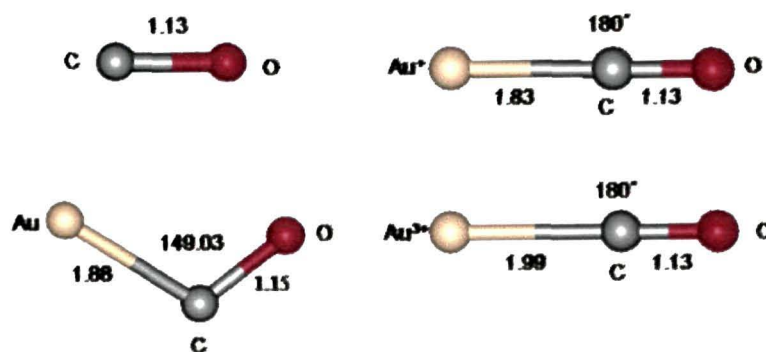
Figure 5.3. Optimized structures of CO and CO adsorbed Au atom in various oxidation states in the gas phase. Bond lengths are in angstroms (Å) and bond angle is in degree.

bond angle between 139^0 and 142^0 and vibrational shift between -125 and -162 cm^{-1} by DFT method using various functionals. Moving over to the cationic gold monomer, the adsorption of CO leads to a linear molecule with the CO binding energy value of 2.54 eV. The properties of the adsorption complexes are listed in Table 5.3.

Table 5.3 Computational results of CO adsorption on gold atom in the gas phase. Bond lengths are in angstroms (Å) and bond angle is in degree.

System	Bond Length (Å)		B. E. (eV)	ω_e(CO) (cm^{-1})	$\Delta\omega$ (cm^{-1})	α (deg)
	C-O	Au-C				
CO	1.133			2179.8		
AuCO	1.15	1.88	0.88	2050.9	-128.9	149.03
Au$^+$CO	1.13	1.83	2.54	2263.5	83.7	180.00
Au^{3+}CO	1.13	1.99	11.11	2129.3	-50.5	180.00

In order to investigate the nature of interaction between the gold atom and carbon monoxide molecule, we have performed Natural Bond Orbital (NBO) analysis by using *Gaussian03* program package.[23] The natural charges and atomic orbital occupancies of the gold carbonyls obtained from this analysis are given in Table 5.4. The values of the partial charges reveal that during formation of AuCO, there is withdrawal of charge density from the gold atom. This leads to an increase in the charge density on the CO molecule. The orbital occupancies for p_x and p_y orbitals show that in case of AuCO, participation of p_x and p_y orbitals of carbon and oxygen

Table 5.4 Partial charges and orbital occupancies of the gas phase complexes based on NPA from NBO analysis.

Complexes	Partial Charge			Orbital Occupancies				
	Au	**C**	**O**	**Au**	**C**	**O**	**C**	**O**
CO		0.194	-0.190		$2s(1.747)2p_x(0.581)$	$2s(1.802)2p_x(1.419)$	p_x+p_y	
					$2p_y(0.581)2p_z(0.897)$	$2p_y(1.419)2p_z(1.554)$	1.162	2.838
AuCO	0.127	0.396	-0.523	$6s(0.522)5d_{xy}(1.926)$	$2s(1.356)2p_x(0.856)$	$2s(1.744)2p_x(1.620)$		
				$5d_{xz}(1.936)5d_{yz}(1.996)$	$2p_y(0.576)2p_z(0.564)$	$2p_y(1.492)2p_z(1.504)$	1.486	3.128
				$5d_{x^2-y^2}(1.846)5dz^2(1.958)$				
Au$^+$CO	0.839	0.416	-0.250	$6s(0.465)5d_{xy}(1.930)$	$2s(1.339)2p_x(0.918)$	$2s(1.738)2p_x(1.608)$		
				$5d_{xz}(1.919)5d_{yz}(1.997)$	$2p_y(0.649)2p_z(0.629)$	$2p_y(1.446)2p_z(0.454)$	1.567	3.054
				$5d_{x^2-y^2}(1.892)d_z^2(1.964)$				
Au^{3+}CO	2.065	0.801	0.134	$6s(0.040)5d_{xy}(1.768)$	$2s(1.013)2p_x(0.785)$	$2s(1.756)2p_x(1.427)$		
				$5dxz(1.963)5d_{yz}(1.999)$	$2p_y(0.679)2p_z(0.670)$	$2p_y(1.338)2p_z(1.336)$	1.464	2.765
				$5d_{x^2-y^2}(1.422)d_z^2(1.748)$				

in the interaction is very high. That is, the occupancy of the antibonding $2\pi^*$ orbital is high, which leads to lower vibrational frequency.

Wu *et al.*[18] found that the binding energy of CO on monomeric gold increases on going from anionic to neutral, and then from neutral to cationic species. They concluded that CO $\rightarrow$ metal electron donation is the dominant mechanism in the formation of the metal-CO bond. In our case too we have found that the binding energy of the CO molecule increases with increasing positive charge on the gold atom (Table 5.3). That is, as the atom becomes more and more deficient in electrons, the interaction with the CO molecule becomes stronger. From Table 5.3 it is observed that the vibrational frequency of the CO molecule in Au^+CO is higher than the frequency of free CO. While there are several factors responsible for this shift in the CO vibrational frequency, one plausible explanation may be given from the electron donation/back-donation mechanism. The molecular orbitals of the CO molecule interacting with the metal are the 5σ (the HOMO), which is weakly antibonding and $2\pi^*$ (the LUMO), which is highly antibonding. While interacting with positively charged metal centers CO acts as a Lewis base. The filled 5σ orbital donates electrons to the empty metal orbitals. This shifts the CO vibrational frequency to higher values. From the partial charges listed in Table 5.4 it is seen that in case of Au^+CO there is donation of electrons from CO to Au resulting in a charge of 0.839 on the cationic metal centre. Analysis of the orbital occupancies indicate that this transfer of charge from the CO to the Au atom takes place mainly from the $2s$ orbital of carbon and $2p_z$ orbitals of carbon and oxygen, which overlap to from the 5σ orbital of CO. In case of Au^{3+} the adsorption complex with CO is again linear. The bond length of the adsorbed CO molecule changes only slightly over that of the gas phase CO. Table 5.3 also shows that there is a shift of -50.5 cm^{-1} in the CO vibrational frequency on going from the free CO molecule to the gold carbonyl in the 3+ oxidation state. The above mentioned mechanism of electron donation from the CO to the metal is not sufficient to explain this red shift in case of $Au^{3+}CO$. Thus, while electron donation/back-donation has a role to play in shifting the CO vibrational frequency, contribution from other factors like electrostatic effect of the charge on the metal interacting with the CO dipole may also be significant.

5.3.3 Adsorption of CO on zeolite supported gold atom

A) cluster model

The optimized structures of the gold monomer in three oxidation states 0, +1 and +3 adsorbed on the six-member ring of faujasite (FAU) zeolite are shown in Figure 5.4. Selected geometric parameters of the CO-Aù-Zeo clusters are summarized in Table 5.5.

(a) Au-FAU   **(b) Au$^+$-FAU**   **(c) Au^{3+}-FAU**

(d) AuCO-FAU   **(e) Au$^+$CO-FAU**   **(f) Au^{3+}CO-FAU**
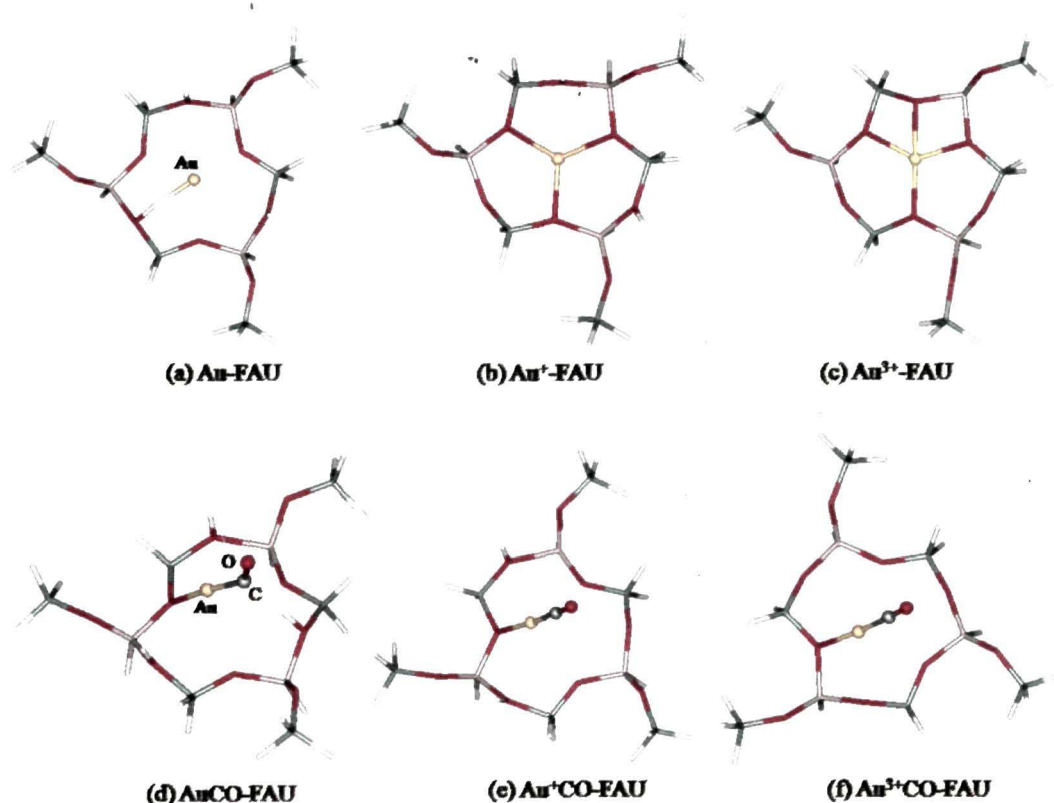
Figure 5.4. Optimized structures of (a-c) gold atom and (d-f) gold carbonyls adsorbed on the six member ring of faujasite zeolite.

An analysis of total energies of the gold atom in the gas phase in the three oxidation states shows that the Au^0 state is the most stable followed by Au$^+$. Au^{3+} is the least stable one. However, when gold is adsorbed on faujasite zeolite Au^{3+} has the highest binding energy of 61.76 eV, followed by the Au$^+$ state with a binding energy of 6.91 eV. The adsorption of Au^0 on faujasite zeolite is endothermic with a binding energy of -0.50 eV. To the best of our knowledge there is no previous theoretical study of a metal atom adsorbed on a faujasite zeolite. In a recent study Sierraalta et al.[24] have performed DFT calculations to investigate the possible active

Table 5.5 Computational results of zeolite (T9 cluster) supported Au atom: bond distances (Å), bond angles (degree), Mulliken charges (q) of selected atoms, vibrational frequency (cm^{-1}) and adsorption energy (eV).

	Au-FAU	Au-CO-FAU	Au$^+$-FAU	Au$^+$CO-FAU	Au^{3+}-FAU	Au^{3+}CO-FAU
Bond distances						
Au-O$_Z$	2.43	2.14	2.12	2.09	2.12	2.01
Au-Al	3.51	3.26	3.20	3.30	3.02	3.08
Au-Si	3.41	3.15	3.07	3.18	2.92	3.09
Au-O$_H$	2.86	3.05	3.18	3.06		
Au-C		1.89		1.83		1.82
C-O		1.18		1.14		1.14
Bond Angle						
Au-C-O		141.63		178.15		176.95
Charges						
q(O$_Z$)	-0.83	-0.84	-0.86	-0.87	-0.85	-0.85
q(Au)	0.80	-0.01	0.32	0.20	0.71	0.34
q(C)		0.02		0.34		0.35
q(O)		-0.18		-0.10		-0.10
q(CO)		-0.16		0.24		0.25
Vibrational Freq						
υ-CO		1911.80		2167.20		2174.10
Binding Energy						
ΔE-Au (eV)	-0.50		6.91		61.76	
ΔE-CO (eV)		1.01		1.15		1.12

sites of Au(I) ion exchanged ZSM-5 zeolite. They obtained binding energy values of Au$^+$ ranging from 6.68 to 8.22 eV at different tetrahedral sites. In our earlier study of Au$_6$ adsorbed on a T9 cluster of faujasite zeolite we have found that the cluster binds to the oxygen atoms of the six member ring with Au-O bond distances lying in the range 2.08 – 2.13 Å.[25] In the present study the Au-O distances show a decreasing trend on going to higher oxidation states having a value of 2.43 Å for the neutral gold monomer and 2.12 Å for the monomer in the oxidation state +3. Thus the neutral gold monomer binds weakly with the zeolite support. The calculated average Au-O distances of supported cationic gold monomer are in good agreement with the experimental EXAFS value of 2.08 Å in NaY zeolite supported cationic gold atoms.[6] Both Au-Al and Au-Si distances decrease on going from oxidation

state 0 to +1 and then to +3. This shows that the interaction of the gold atom with the zeolite support gets stronger on going to higher oxidation states.

The carbonyl complexes were formed by adsorbing a CO molecule on the supported Au monomer. In all the three oxidation states they were found to retain their gas phase structures with only a slight decrease in the Au-C-O bond angle. The C-O bond length of the supported gold carbonyl was found to vary from 1.14 to 1.18 Å which is only slightly higher than the gas phase value of 1.13 Å. A comparison of the structures of the zeolite supported gold monomers with and without CO shows that for all three oxidation states the Au-O bond distances decrease on CO adsorption indicating that CO facilitates stronger interaction of the Au atom with the support. The Au-O bond lengths in the carbonyls are 2.15, 2.05 and 2.01 Å, respectively in the oxidation states 0, +1 and +3. The change in Au-O bond length due to CO adsorption is largest in case of Au^0. It is also observed from Table 5.5 that the Au-O bond distance decreases with increasing oxidation state of the gold atom. Thus the gold carbonyl in the oxidation state +3 is most strongly anchored to the zeolite support. The Au-Al bond distances in the carbonyls are 3.26, 3.23 and 3.07 Å for CO adsorbed on the gold monomer in the oxidation states 0, +1 and +3, respectively. The CO vibrational frequency in the supported AuCO complex is 1911.8 cm^{-1} which is red shifted by 268 cm^{-1} over that of the gas phase carbonyl. Gates and his group, in their experimental study[26] of tricarbonyls of mononuclear gold Au^0 supported on zeolite NaY using X-ray absorption spectroscopy found three υ_{CO} bands at 2070, 2033 and 2000 cm^{-1}. Sterrer *et al.*[27] in their investigation of CO adsorption on Au/MgO involving a single gold atom using EPR and STM found red shifts in the CO vibrational frequency of 290 and 220 cm^{-1} by using perfect MgO(100) and O-deficient MgO samples, respectively. A DFT based theoretical investigation by Castellani and coworkers[28] regarding interaction of CO on gold atoms adsorbed on surface anionic (O^{2-}) and neutral oxygen vacancy (F_s) sites of MgO(100) surface revealed red shifts in the CO vibrational frequency between 232 and 358 cm^{-1} over that of free CO. For the supported gold carbonyl in the neutral state the electron cloud is relatively more polarizable than in the other cases because the nearest neighbor oxygen atoms of the zeolite framework are more distant (Au-O distance is 2.14 Å). As a result there is a substantial charge transfer to CO, thus populating the $2\pi^*$ antibonding orbital, which leads to the large red shift in the CO vibrational frequency. This can be observed from the Mulliken population analysis

given in Table 5.5. The binding energy of the CO molecule to the zeolite supported gold atom has the values 1.01, 1.15 and 1.12 eV in the oxidation states 0, +1 and +3, respectively. Thus the binding of CO is strongest when the gold atom is in the oxidation state +1. This is supported by the low value of Au-C bond distance as seen from Table 5.3.

B) embedded cluster model

For a more realistic representation of the support we extend our study of CO adsorption on the supported gold monomer to a large zeolite cluster having 60T sites. Choosing a six-member ring which forms a wall of the supercage of the faujasite zeolite structure as the core region, we adsorb a gold atom onto it. As in the case of the cluster model study described above, for the embedded cluster too, the gold monomer is adsorbed in three charged states Au^0, Au^+ and Au^{3+}. The optimized geometries are shown in 5.5 and selected geometric parameters of the Au-Zeo-CO complexes are listed in Table 5.6. The binding energies of Au^+ and Au^{3+} onto the zeolite cluster follow the same trend as observed in case of the T9 cluster, i.e, Au^{3+} binds most strongly to faujasite zeolite, followed by Au^+. The adsorption of Au^0 on faujasite zeolite is endothermic with a binding energy of -0.29 eV. As in case of the cluster model, the Au–O distances show a decreasing trend with increasing charge on the gold atom, 2.70, 2.20 and 2.11 Å, in the oxidation states 0, +1 and +3, respectively. The Au–Al and Au–Si distance are minimum for Au^+ followed by Au^{3+}. The Au^0–Zeo complex exhibits the highest Au–Al and Au–Si distances of 3.71 and 3.61 Å, respectively. For the supported carbonyls, the Au–C–O structures are retained in case of Au^+ and Au^{3+}. For Au^0 the Au–C–O bond angle has a value of 132.75°, while the gas phase value is 149.03°. The C–O bond distances for the supported carbonyls vary from 1.13 to 1.15 Å. As found for the cluster model, the Au–O distance decreases with CO adsorption, indicating that the presence of CO enhances the interaction of the gold monomer with the zeolite support. The Au–O bond lengths in the supported carbonyls are 2.11 Å in case of Au^+ and Au^{3+}, while it is 2.50 Å in case of Au^0. It is seen from the values of the bond lengths provided in Table 5.6 that both for the supported carbonyls with and without CO, the Au–O, Au–Al and Au–CO distances are minimum in case of Au^+, followed by Au^{3+}. Thus the gold monomer in the oxidation state +1 is most strongly
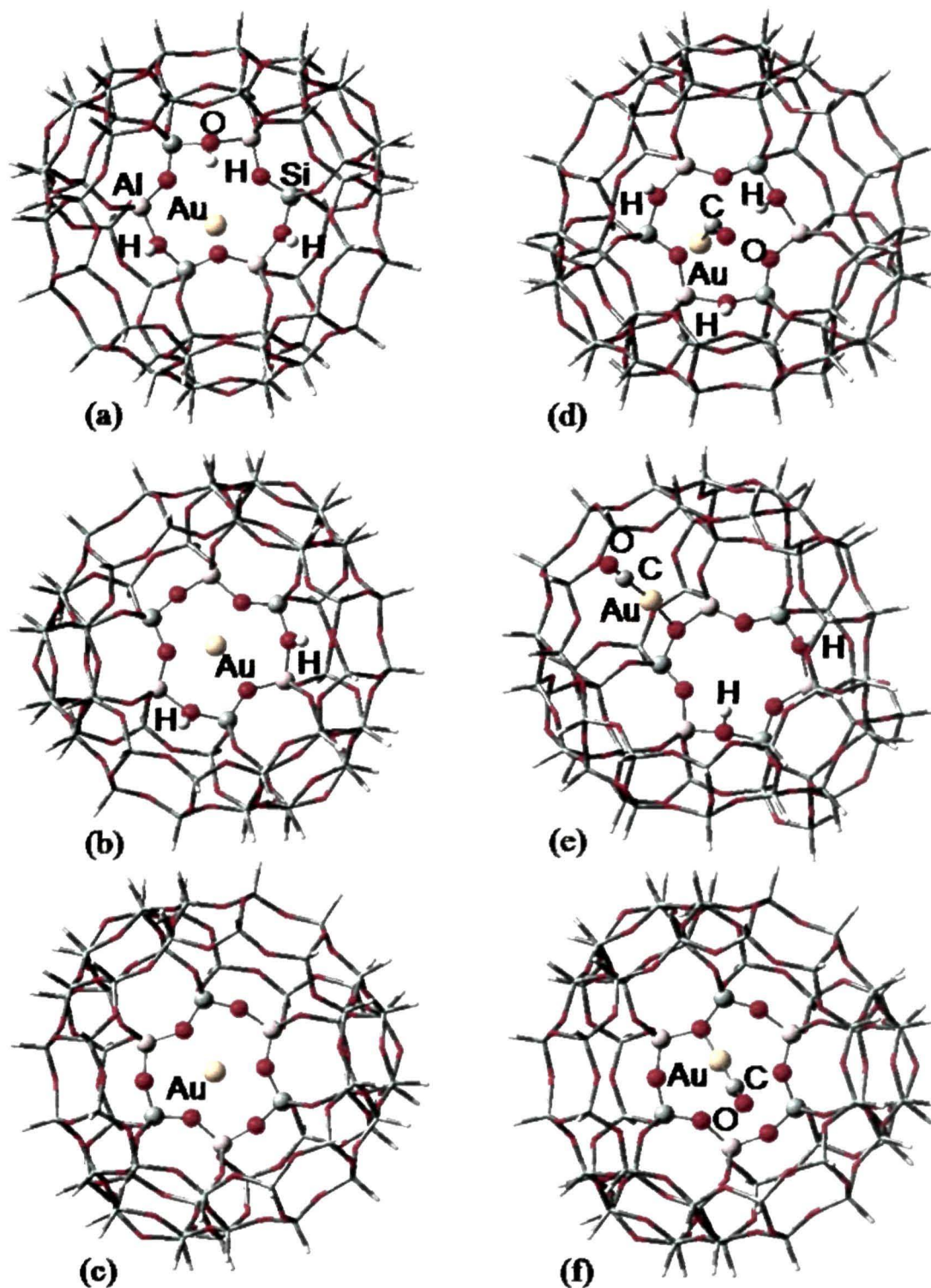
Figure 5.5. Optimized structures of (a-c) gold atom and (d-f) gold carbonyls adsorbed on the T60 cluster of faujasite zeolite.

anchored to the faujasite zeolite support. The CO vibrational frequency for the Au^0-Zeo-CO complex is found to be 1949.99 cm^{-1}, which is red shifted by 230 cm^{-1} over the gas phase value while for the Au^+-Zeo-CO complex there is a red shift of 141

cm^{-1} compared to the gas phase value. Red shifts in the CO vibrational frequencies have also been found for the zeolite supported gold carbonyls for oxidation states 0 and +1 by using the cluster model. The binding energies of the CO molecule to the zeolite supported gold monomer are 0.42, 1.34 and 1.07 eV as found by our embedded cluster model. A comparison with the values obtained by the cluster model reveals that use of the embedded cluster model leads to a significant improvement in the CO binding energy (1.34 eV in the embedded cluster model versus 1.15 eV in the cluster model) for the supported gold monomer in the +1 oxidation state.

Table 5.6 Computational results of zeolite (T60 cluster) supported Au atom: bond distances (Å), bond angles (degree), Mulliken charges (q) of selected atoms, vibrational frequency (cm^{-1}) and adsorption energy (eV).

	Au-FAU	Au-CO-FAU	Au$^+$-FAU	Au$^+$CO-FAU	Au^{3+}-FAU	Au^{3+}CO-FAU
Bond distances						
Au-O$_Z$	2.70	2.50	2.20	2.11	2.24	2.11
Au-Al	3.71	3.46	3.17	3.01	3.25	3.23
Au-Si	3.61	3.44	3.13	3.21	3.33	3.22
Au-O$_H$	3.50	3.51	3.21	6.58		
Au-C		2.06		1.89		1.90
C-O		1.15		1.13		1.13
Bond Angle						
Au-C-O		132.75		178.53		179.17
Charges						
q(O$_Z$)	-0.64	-0.66	-1.17	-1.32	-1.29	-1.22
q(Au)	0.45	0.29	0.77	0.73	0.98	0.73
q(C)		0.33		0.43		0.46
q(O)		-0.16		-0.36		-0.35
Dq		-0.16		-0.07		-0.12
Vibrational Freq						
υ-CO		1949.99		2122.07		2478.72
Binding Energy						
ΔE-Au (eV)	-0.29		6.82		62.93	
ΔE-CO (eV)		0.42		1.34		1.07

5.4. Conclusions

We have tried to verify the predictions regarding the response of various sites of the cationic, neural and anionic triangular Au_6 clusters towards electrophilic and nucleophilic attacks by adsorbing CO and O_2 molecules onto these structures. It has been found that CO adsorbs more strongly on the cationic cluster compared to the neutral and anionic clusters. The CO molecule prefers the apex site for adsorption, while the O_2 molecule prefers the mid site. Also, the co-adsorption of CO and O_2 on these clusters has been investigated. For the most stable co-adsorption complex, CO adsorbs at the apex site and O_2 at the bridge site in agreement with Fukui function values.

We have also investigated the adsorption of the CO molecule on the gold monomer in three oxidation states 0, +1 and +3 in the gas phase and on a zeolite support. The results of our study reveal that in case of the gas phase carbonyls, the adsorption of CO is strongest in the oxidation state +3, while on a faujasite zeolite support having 9T sites CO binds most strongly to Au^+. For the AuCO complex, the vibrational frequency of CO is red shifted over that of free CO ($\Delta\upsilon = -128.9$ cm^{-1}), while in case of Au^+CO it is blue shifted ($\Delta\upsilon = 83.7$ cm^{-1}). $Au^{3+}CO$ shows a red shift of 50.5 cm^{-1}. The binding energy of the gold monomer on the zeolite support increases on going to higher oxidation states. CO facilitates stronger interaction of the gold monomer with the support. For the supported carbonyls, CO vibrational frequencies have the values 1911.8, 2167.2 and 2174.1 cm^{-1} for oxidation states 0, +1 and +3, respectively. Thus the vibrational frequencies increase on going to higher oxidation states. Further, in order to understand the effect of the size of the support on adsorption of CO molecule onto the gold monomer, we have repeated our study on the supported gold monomer by taking a large zeolite cluster having 60T sites. This cluster has been treated by the hybrid QM/MM method. Our results for this larger zeolite model show the same trend in the adsorption energies and vibrational frequencies as observed in case of the cluster model. However, the binding of the CO molecule onto Au^+ becomes stronger on increasing the size of the support.

References

[1] Fu, Q.; Saltsburg, H.; Flytzani-Stephanopoulos, M. Active nonmetallic Au and Pt species on ceria-based water-gas shift catalysts. *Science*, **301**, 935-938 (2003).

[2] Stangland, E. E.; Stavens, K. B.; Andres, R. P.; Deglass, W. N. Characterization of gold-titania catalysts via oxidation of propylene to propylene oxide. *J. Catal.* **191**, 332-347 (2000).

[3] Nkosi, B.; Adams, M. D.; Coville, N. J.; Hutchings, G. J. Hydrochlorination of acetylene using carbon-supported gold catalysts: A study of catalyst reactivation. *J. Catal.*, **128**, 378-386 (1991).

[4] Phala, N. S.; Klatt, G.; Steen, E. van. A DFT study of hydrogen and carbon monoxide chemisorption onto small gold clusters. *Chem. Phys. Lett,.* **395**, 33-37 (2004).

[5] Yoon, B. *et al*. Charging effects on bonding and catalyzed oxidation of CO on Au₈ clusters on MgO. *Science*, **307**, 403-407 (2005).

[6] Fierro-Gonzalez, J. C. ; Gates, B. C. Mononuclear Au^{III} and Au^{I} complexes bonded to zeolite NaY: catalysts for CO oxidation at 298 K. *J. Phys. Chem. B*, **108**, 16999-17002 (2004).

[7] Simakov, A. *et al*. Influence of sodium on activation of gold species in Y-zeolites. *Catal. Comm.*, **9**, 1277-1281 (2008).

[8] Ricci, D., Bongiorno, A.; Pacchioni, G.; Landman, U. Bonding trends and dimensionality crossover of gold nanoclusters on metal-supported MgO thin films. *Phys. Rev. Lett.*, **97**, 036106-036110 (2006).

[9] Giordano, L.; Pacchioni, G. Charge transfers at metal/oxide interfaces: a DFT study of formation of K$^{\delta+}$ and Au$^{\delta-}$ species on MgO/Ag(100) ultra-thin films from deposition of neutral atoms. *Phys. Chem. Chem. Phys.*, **8**, 3335-3341 (2006).

[10] Löwenstein, W. The disribution of aluminium in the tetrahedra of silicates and aluminates. *Am. Mineral.*, **39**, 92-98 (1954).

[11] Olson, D. H. The crystal structure of dehydrated NaX. *Zeolites*, **15**, 439-443 (1995).

[12] Dapprich, S; Komárami, I; Byun, K. S.; Morokuma, K; Frisch, M. J. A new ONIOM in implementation Gaussian98. PartI. The calculation of energies,

vibrational frequencies and electric field derivatives. *J. Mol. Struct.,(THEOCHEM)* **461-462**, 1-21 (1999).

[13] Becke, A. D. Density-functional exchange-energy approximation with correct asymptotic behavior. *Phys. Rev. A*, **38**, 3098-3100 (1988).

[14] Lee, C.; Yang, W.; Parr, R. G. Development the Colle-Salvetti correlation-energy formula into a functional of the electron density. *Phys. Rev. B*, **37**, 785-789 (1988).

[15] Hay, P. J.; Wadt, W. R. *Ab initio* effective core potentials for molecular calculations. Potentials for the transition metal atoms Sc to Hg. *J. Chem. Phys.*, **82**, 270-283 (1985).

[16] Hay, P. J.; Wadt, W. R. Ab initio effective core potentials for molecular calculations. Potentials for K to Au including the outermost core orbitals. *J. Chem. Phys.* **82**, 299-310, (1985).

[17] Joshi, A. M.; Deglass, W. M.; Thomson, K. T. Adsorption of copper clusters in TS-1 pores: Ti versus Si and gold versus copper. *J. Phys. Chem. C.*, **111**, 11888-11896 (2007).

[18] Wu, X.; Senapati, L.; Nayak, S. K.; Selloni, A.; Hajaligol, M. A density functional study of carbon monoxide adsorption on small cationic, neutral and anionic gold clusters. *J. Chem. Phys.*, **117**, 4010-4015 (2002).

[19] Phala, N. S.; Klatt, G.; Steen, E. van. A DFT study of hydrogen and carbon monoxide chemisorption onto small gold clusters. *Chem. Phys. Lett.* **395**, 33-37 (2004).

[20] Zhai, H.-J. ; Kiran, B.; Dai, B.; Li, J; Wang, L.-S. Unique CO chemisorption properties of gold hexamer: $Au_6CO_n^-(n = 0\text{-}3)$. *J. Am. Chem. Soc.* **127**, 12098-12106 (2005).

[21] Huber, H.; Herzberg, G. *Molecular Spectra and Molecular Structure IV. Constants of Diatomic Molecules.* (Van Nostrand Reinhold, New York 1979).

[22] Giordano, L.; Carrasco, J.; Valentin, C. D. ; Illas, F.; Pacchioni, G. Vibrational and electron paramagnetic resonance properties of free and MgO supported AuCO complexes. *J. Chem. Phys.*, **124**, 174709-174716 (2006).

[23] Frisch, M. J. *et al., Gaussian 03, Revision C.02, Gaussian Inc, Wallingford, CT*, 2004.

[24] Sierraalta, A.; Alejos, P. ; Ehrmann, E.; Rodriguez, L. J.; Ferrer, Y. DFT-ONIOM study of Au/ZSM-5 catalyst: active sites, thermodynamic and vibrational frequencies. *J. Mol. Catal. A: Chemical*, **301**, 61-66 (2009).

[25] Deka, R.C.; Deka, A.; Miyamoto, A. Density functional studies on the structure and reverse hydrogen spillover in Au_6 cluster supported on zeolite. *Catal. Lett.*, **131**, 155-159 (2009).

[26] Anderson, B. G. *et al.* Tricarbonyls of low-coordinated Au(0) atoms in zeolite-supported gold nanoparticles: evidence from infrared and x-ray absorption spectroscopies. *Langmuir*, **22**, 4310-4314 (2006).

[27] Sterrer, M. *et al.* When the reporter induces the effect: unusual IR spectra of CO on Au_1/MgO (001)/Mo(001). *Angew. Chem. Int. Ed.*, **45**, 2633-2635 (2006).

[28] Ferullo, R. M.; Fuente, S. A. ; Belelli, P. G. ; Castellani, N. J. CO interaction with Au atoms adsorbed on terrace, edge and corner sites of the MgO(100) surface. Electronic structure and vibrational analysis from DFT. *Surf. Sc.*, **603**, 1262-1269 (2009).

CHAPTER 6

Energetics of Reverse Hydrogen Spillover from Zeolite Support to Gold Nanoclusters

Having determined the structure of mononuclear gold supported on faujasite zeolite, we now investigate the phenomenon of reverse hydrogen spillover of acidic protons from zeolite to the gold monomer in the oxidation states 0 and +1. It is found that in the oxidation state 0, the hydrogenated clusters AuH/(2H)-FAU and AuH_2/H-FAU, generated by stepwise reverse hydrogen spillover from bridging OH groups of zeolite are energetically preferred over the non hydrogenated Au/(3H)-FAU structure. Reverse hydrogen spillover of all three acidic protons onto the gold monomer does not lead to a stable structure. This study is further extended to the highly stable neutral triangular Au_6 cluster. It is found that the hydrogenated cluster Au_6H/(2H)-FAU, Au_6H_2/H-FAU and Au_6H_3/FAU are energetically favourable over the non hydrogenated Au_6/(3H)-FAU structure. The energies of reverse hydrogen spillover per transferred proton are −67.6, −65.6 and −59.1 kJ/mol, respectively for zeolite supported Au_6H, Au_6H_2 and Au_6H_3 clusters.

6.1 Introduction

Oxide supported transition metal clusters form an important class of system for a large number of investigations mainly due to their widespread applications as catalysts. For clusters of nanometer and subnanometer size, direct and comprehensive experimental information is difficult to achieve. Such clusters have been theoretically investigated using various computational methods over the past few years.[1-5] Zeolites with pores and cavities of molecular dimensions form an important class of support for nanoclusters in catalysis. It has been emphasized that

well-dispersed gold clusters inside faujasite and ZSM-5 zeolites exhibit high activity for chemisorption of NO and CO and also in NO + CO and direct NO decomposition reactions.[6] In view of the growing interest in metal cluster catalysis, there have been a large number of experimental studies[7-10] devoted towards understanding the structure and nature of active sites in supported metal clusters. However, it is seen that sometimes experimental investigations yield incomplete or ambiguous results. It is here that theoretical studies[11-13] based on pertinent models and accurate electronic structure techniques contribute significantly.

From their studies on gas phase and zeolite supported Rh_6 clusters with and without impurity atoms, Rösch and co-workers [14] concluded that zeolite supported Rh_6 clusters contain hydrogen impurity atoms. They have also performed extensive studies on the reverse hydrogen spillover of acidic hydrogen atoms of zeolite to a large number of hexanuclear transition metal clusters using density functional theory.[11,15] They found that reverse spillover of acidic hydrogen of zeolite to the metal clusters was favourable for many transition metals with a very low value for gold (18 kJ/mol). However, it should be noted that the isolated cluster models used by them contain 6 tetrahedral atoms of faujasite zeolite which was terminated by OH groups. The OH terminated cluster may not be a good model to represent zeolite. Shor *et al.*[15] improved the energy of reverse hydrogen spillover to some extent by using a novel embedded cluster method. However, they found that in case of gold cluster, unlike the other transition metals studied, the hydrogenated form M_6H_3/FAU (M = transition metal) is not necessarily more stable than the bare zeolite-supported form M_6/(3H)-FAU and that the process of reverse hydrogen spillover from the zeolite to the metal cluster may be exothermic or endothermic depending upon the initial location of the migrating protons in the zeolite substrate. It was found that reverse hydrogen spillover from less acidic hydroxyl groups to the gold cluster was endothermic by a value 29 kJ/mol per transferred proton and that from more acidic hydroxyl groups to the metal cluster was exothermic by 47 kJ/mol per proton. Experimentally also it have been observed that reverse spillover takes place on zeolite supported Ir_6 cluster during catalysis.[16] In the case of zeolite supported Au_6 cluster, to the best of our knowledge, there is no experimental data available yet.

As we have already determined the structure of the gold monomer anchored on a T9 cluster of faujasite zeolite, which has been presented in the last chapter, we now investigate the process of reverse hydrogen spillover from the support onto the

gold atom in the oxidation states 0 and +1. To the best of our knowledge, this is the first study of reverse hydrogen spillover onto a zeolite supported gold monomer. Further, keeping in mind the discrepancies regarding the process of reverse hydrogen spillover in case of zeolite supported gold hexamer, we examine the process in detail by systematically transferring acidic hydrogen of a zeolite cluster containing 9 tetrahedral sites and terminated by hydrogen atoms, one by one.

6.2 Computational Details

In this study we have used the same T9 cluster of the zeolite used in our earlier investigation on CO adsorption on supported gold monomer presented in Chapter 5. The optimization follows the same methodology of optimizing only the Si–H, Al–H and O–H bonds while keeping the other atoms fixed at their crystallographic positions and allowing all atoms other than the terminating hydrogen atoms to relax in the subsequent calculations. All electron relativistic calculations have been performed by using the DMol^3 program with DNP basis set. The calculations for the gold monomer use the VWN exchange-correlation functional for geometry optimization and the BLYP functional for determination of energy and other related properties, while the calculations for the supported gold hexamer involve the VWN functional only.

We calculate the reverse hydrogen spillover energy per transferred acidic hydrogen atom, E_{RS}, to the supported Au monomer using the following equation:

$$E_{RS} = \{E[AuH_n/((3-n)HFAU)] - E[Au/(3HFAU)]\}/n ,\qquad(6.1)$$

where n = 1 and 2, and

$$E_{RS} = \{E[Au^+H/(HFAU)] - E[Au^+/(2HFAU)]\}\qquad(6.2)$$

For the supported Au$_6$ cluster we have

$$E_{RS} = \{E[Au_6H_n/((3-n)HFAU)] - E[Au_6/(3HFAU)]\}/n,\qquad(6.3)$$

where n = 1, 2 and 3.

A negative value of the E_{RS} implies that the hydrogenated metal clusters, $Au^{0,+}H_n$ or Au_6H_n on zeolite support are more stable than their corresponding dehydrogenated counterparts.

1.1　6.3　Results and Discussion

6.3.1 Reverse hydrogen spillover onto zeolite supported Au^0, Au^+

The optimized structures of bare and hydrogenated Au^0 and Au^+ clusters adsorbed on the six-member ring of faujasite zeolite are shown in Figure 6.1. Selected geometric parameters of the adsorbed clusters are summarized in Table 6.1.
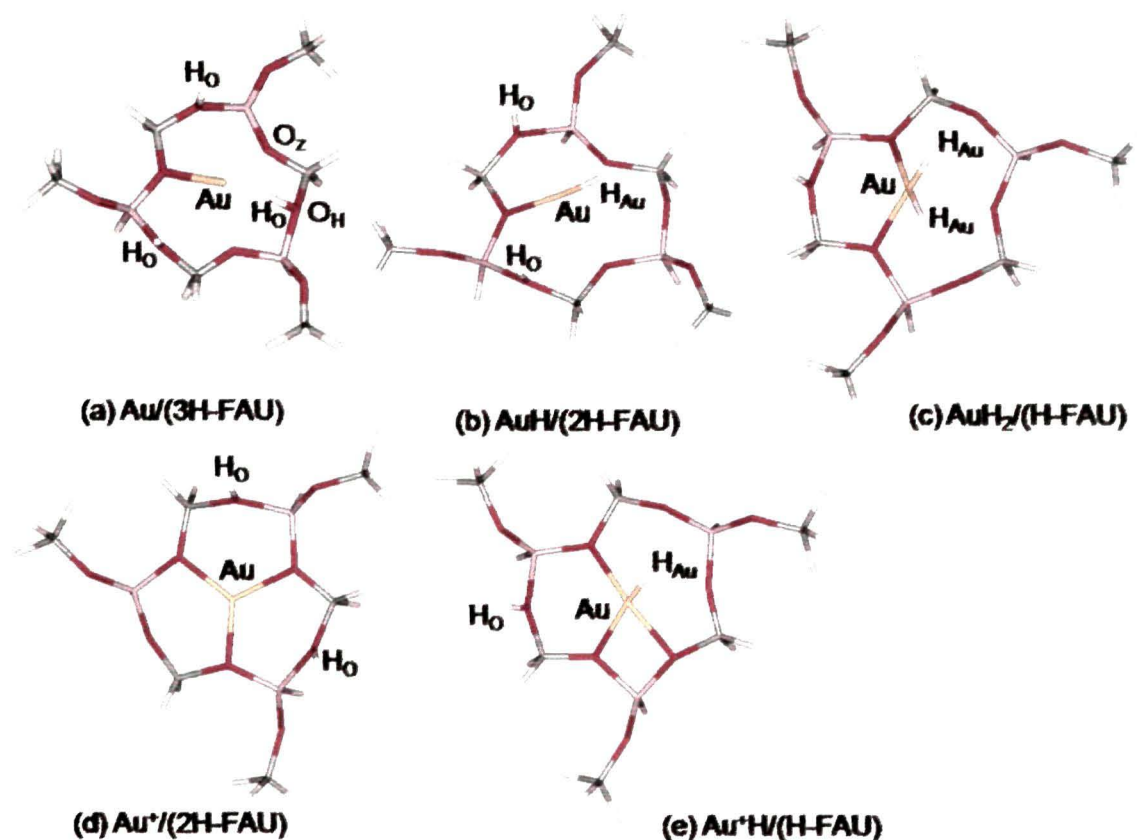
Figure 6.1. Optimized structures of (a, d) bare and (b, c, e) hydrogenated clusters of Au and Au^+ adsorbed on the six member ring of faujasite zeolite.

As seen from Table 6.1, the Au–Oz distance for the Au/3H-FAU cluster is 2.428 Å which is significantly higher than the experimental EXAFS value of 2.08 Å in zeolite supported gold clusters.[9] This shows that the neutral gold monomer is weakly bound to the zeolite support. Moving over to the supported gold monomer in the oxidation state +1, the Au–Oz distance is 2.115 Å, indicating that the bonding with the support is stronger in this case.

The hydrogenated clusters, AuH, AuH_2 and Au^+H were formed by transferring acidic protons in a stepwise manner from the zeolite to the supported

Table 6.1. Computational results of zeolite supported Au and Au$^+$ monomer and complexes formed after stepwise reverse hydrogen spillover: average distances (Å), total charge of the clusters and energy characteristics (kJ/mol) per transfer of hydrogen atoms.

	Au/(3H)-FAU	AuH/(2H)-FAU	AuH$_2$/H-FAU	Au$^+$/(2H)-FAU	Au$^+$H/(H)-FAU
Bond distances					
Au—^{1}O$_Z$	2.429	2.191	2.179	2.115	2.151
Au—^{2}O$_H$	2.863	3.064	3.020	2.904	2.282
Au—Al	3.512	3.372	3.279	3.196	3.134
Au—Si	3.406	3.226	3.242	3.065	3.149
Au—^{3}H$_{Au}$		1.527	1.519		1.530
Charges					
q(Mulliken) Au	-0.174	0.156	0.241	0.324	0.165
q(Mulliken)^{4}H$_O$	0.355	0.333	0.337	0.333	0.338
q(Mulliken)H$_{Au}$		0.020	0.289		0.083
q (Hirshfeld)Au	0.081	0.243	0.381	0.278	0.240
q(Hirshfeld)H$_O$	0.145	0.288	0.205	0.305	0.208
q(Hirshfeld)H$_{Au}$		-0.045	0.293		-0.017
$^5E_{RS}$		-10.164	-5.118		20.938

^{1}O$_Z$ – oxygen atoms of zeolite connected to the gold atom, ^{2}O$_H$ - oxygen atoms where acidic hydrogen atoms are attached, ^{3}H$_{Au}$ – acidic hydrogen of zeolite which has migrated to the gold atom, ^{4}H$_O$ acidic hydrogen of zeolite, $^5E_{RS}$ – reverse spillover energy.

Au$^{0,+}$ atom. Attempts to simulate the transfer of three protons in case of the supported neutral monomer and two protons in case of the monomer in the oxidation state +1 failed. As seen from Table 6.1, the Au–Oz distance gets significantly reduced in presence of hydrogen spilt over from the zeolite to the gold atom. The Au–Oz distance with two spilled over hydrogen atoms is 2.18 Å. Thus with increasing number of protons in the clusters, the Au–O distance decreases. However, in case of the gold monomer in the oxidation state +1 the Au–Oz distance increases due to reverse hydrogen spillover. Thus in this case, the bare monomer is more strongly anchored to the support than that with the spilled over hydrogen. The Au–Al distance is found to decrease from supported Au$^{0,+}$ cluster to supported Au$^{0,+}$H$_n$. The Au–Si distance decreases due to reverse hydrogen spillover in case of

the supported Au^0 while it increases in case of the supported Au^+ monomer. The distance of Au atom to the spilled over hydrogen atom is found to decrease with the increase in the number of hydrogen atoms in the cluster indicating a strong interaction of the metal atom with hydrogen.

The total charges on AuH, AuH_2 and Au^+H clusters are also presented in Table 6.1. The increasing values of the charges reveal oxidation of the gold atom on going from the bare to the hydrogenated cluster in case of the supported gold monomer in the oxidation state 0 while in case of the oxidation state +1 the charges decrease on going from the bare to the hydrogenated cluster indicating reduction of the gold atom. As seen from Table 6.1, in case of the supported gold monomer in the oxidation state 0, reverse hydrogen spillover energy E_{RS} for the first proton is − 10.16 kJ/mol while E_{RS} per atom for transfer of two protons from the zeolite cluster is −5.12 kJ/mol. Thus both these processes are exothermic. In case of the gold monomer in the oxidation state +1, reverse spillover of a single proton takes place from the support to the gold atom. The reverse spillover energy is 20.94 kJ/mol. Thus this process is endothermic and hence is not energetically favoured.

6.3.2 Reverse hydrogen spillover onto zeolite supported Au₆

We first present the structure of Au_6 cluster in the gas phase. As found in Chapter 3, the most stable form of the Au_6 cluster has a triangular structure (Figure 6.2) with a slight deviation of the three edge atoms from linearity ($\angle$Au–Au–Au = 176.3^0). The average Au–Au bond length of the outer triangles is 2.533 Å whereas that of the inner triangle is 2.647 Å. On zeolite support Au_6 is significantly deviated from its planar triangular structure observed in the gas phase (Figure 6.2). This is in contrast with the adsorption of Au_4 on MgO(001) surface where geometry of the adsorbed
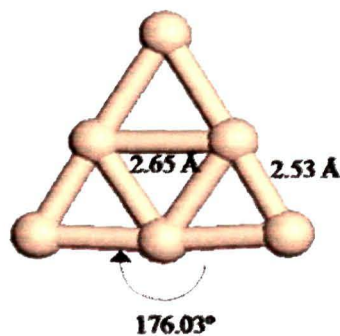
Figure 6.2. Optimized structure of Au_6 cluster in the gas phase. Bond lengths are in angstroms (Å) and bond angle is in degree.

cluster changes very little compared to their gas phase values.[18,19] As shown in Figure 6.3(a), the three apical Au atoms of supported Au_6 cluster move closer to the oxygen atoms of the zeolite and thus it deviates from its original planar structure. For the convenience of discussion, the three atoms in the top triangle are designated as Au_t and the three apical atoms attached to the zeolite framework are designated as Au_z. The average Au_z–Au_t distance (2.559 Å) is very close to the gas phase average bond length of the outer triangles (2.533 Å) and the average Au_t–Au_t (2.650 Å) distance also remains almost same as that of the inner triangle (2.647 Å) of the gas phase structure. However, the Au_z–Au_t–Au_z angle deviates significantly from its gas phase value of 176.3^0 to 104.7^0 in the zeolite supported cluster. Vayssilov and Rösch[11] found an almost planar structure in both gas phase and adsorbed state using a different zeolite cluster model with constraint geometry optimization. The calculated average Au–O (2.135 Å) distance of supported Au_6 cluster is in very good agreement with the experimental EXAFS value of 2.08 Å in zeolite supported gold clusters.[9]

(a) Au_6/(3H)-FAU

(c) Au_6H_2/H-FAU

(b) Au_6H/(2H)-FAU

(d) Au_6H_3/FAU
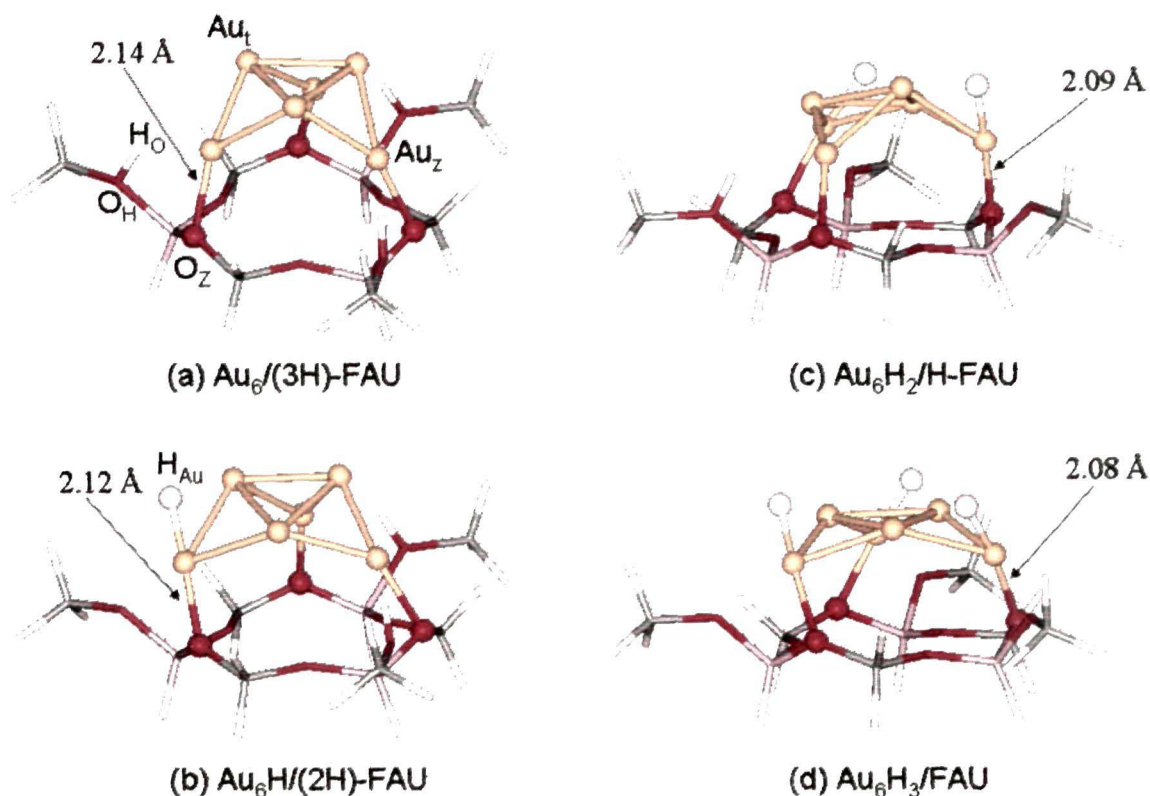
Figure 6.3. Optimized structures of (a) bare and (b-d) hydrogenated clusters of Au_6 adsorbed on the six member ring of faujasite zeolite.

The hydrogenated clusters Au_6H, Au_6H_2 and Au_6H_3 are found to retain the shape of the zeolite supported Au_6 cluster. The average Au_z–Au_t–Au_z angles in $Au_6H/(2H)$-FAU, $Au_6H_2/(1H)$-FAU and Au_6H_3/FAU are 117.0^0, 129.7^0 and 143.3^0, respectively. The average Au–O bond distances of $Au_6H/(2H)$-FAU, $Au_6H_2/(1H)$-FAU and Au_6H_3/FAU clusters are given in Table 6.2. It is seen from Table 6.2 that with the increasing number of protons in the clusters, the average Au–O distance decreases from 2.135 Å in $Au_6/(3H)$-FAU cluster to 2.084 Å in Au_6H_3/FAU cluster. It should be noted that the Au–O distance obtained by EXAFS $(2.08 Å)^9$ for mononuclear gold particles in faujasite zeolite is exactly same with the value obtained in our calculation for zeolite supported Au_6H_3 cluster. For large gold particles supported on alumina, the EXAFS value of Au–O distance $(2.04-2.05 Å)^{19}$ is very close to our results. The average Au–Al distance is found to decrease from supported Au_6 cluster to Au_6H_3 while there is an increase in average Au–Si distance. The distance of Au atom to the spilled over hydrogen atom is found to decrease with the increase in the number of hydrogen atoms in the cluster indicating a strong interaction of the metal cluster with hydrogen atoms. The average Au_z–O_H (oxygen atom where acidic hydrogen atom is attached) distance in the adsorption complex Au_6H_3/FAU is 2.303 Å. Thus, while in the Au_6 cluster supported on zeolite each Au_z atom interacts with only one oxygen atom (average Au_z–O_z=2.135 Å) of zeolite framework, the Au_z atoms of the hydrogenated cluster, Au_6H_3, are coordinated to two oxygen atoms of the zeolite cluster, O_z and O_H with average Au_z–O_z and Au_z–O_H distances of 2.084 Å and 2.303 Å, respectively. Therefore, due to reverse hydrogen spillover there is a stronger interaction of the metal cluster with the zeolite support. This is at variance with the findings of Vayssilov and Rösch.[11] Their study showed that Au_6 is bound to the zeolite cluster via three metal-oxygen bonds unlike the other transition metal clusters of groups 8-11.

The charges of the Au and H atoms calculated using both Mulliken Population Analysis (MPA) and Hirshfeld Population Analysis (HPA) in the zeolite supported bare and hydrogenated clusters are collected in Table 6.2. The MPA derived charges of Au_6 cluster in $Au_6/(3H)$-FAU have negative values for the all the six Au atoms with a total charge of –0.411 e. However, HPA for Au_z atoms in contact with oxygen atoms of zeolite show positive values (0.066 e per atom) in contrast to negative values for the "top" triangle, Au_t atoms (-0.059 e per atom) with a total charge of the cluster close to zero (0.021 e). Both MPA and HPA values for

Table 6.2. Computational results of zeolite supported Au_6 cluster and complexes formed after stepwise reverse hydrogen spillover: average distances (Å), average angles (degree), Mulliken and Hirshfeld charges (q) of selected atoms and energy characteristics (kJ/mol) per transfer of hydrogen atoms.

	$Au_6/(3H)$-FAU	$Au_6H/(2H)$-FAU	Au_6H_2/H-FAU	Au_6H_3/FAU
Bond distances				
^1Au_z—^2Au_t	2.559	2.564	2.563	2.561
Au_t—Au_t	2.650	2.638	2.651	2.681
Au_z—^3O_z	2.135	2.116	2.089	2.084
Au_z—^4O_H		2.374	2.355	2.303
Au_z—Al	2.934	2.899	2.796	2.662
Au_z—Si	3.201	3.219	3.287	3.427
Au_t—$^5H_{Au}$		1.634	1.625	1.607
Bond angle				
Au_z—Au_t—Au_z	104.7	117.0	129.7	143.3
Charges				
q(Mulliken) Au_z	-0.074	0.005	0.090	0.160
q(Mulliken) Au_t	-0.063	-0.028	0.002	0.034
q(Mulliken) Au_6	-0.411	-0.071	0.277	0.583
q(Mulliken) ^6H_O	0.331	0.337	0.343	
q(Mulliken) H_{Au}		0.116	0.126	0.142
q(Mulliken) Au_6H_n		0.045	0.529	1.010
q(Hirshfeld) Au_z	0.066	0.127	0.207	0.292
q (Hirshfeld) Au_t	-0.059	-0.009	0.045	0.094
q (Hirshfeld) Au_6	0.021	0.352	0.757	1.157
q(Hirshfeld)^6H_O	0.098	0.123	0.138	
q(Hirshfeld)H_{Au}		-0.055	-0.051	-0.044
q(Hirshfeld)Au_6H_n		0.297	0.654	1.026
$^7E_{RS}$		-67.6	-65.6	-59.1

^1Au_z – gold atoms bound to the zeolite cluster, ^2Au_t – gold atoms of the "top triangle" of supported Au_6 clusters, ^3O_z – oxygen atoms of zeolite connected to the gold cluster, ^4O_H – oxygen atoms where acidic hydrogen atoms are attached, $^5H_{Au}$ – acidic hydrogen of zeolite which has migrated to the gold cluster, ^6H_O - acidic hydrogen of zeolite, $^7E_{RS}$ – reverse spillover energy.

Au_z and Au_t atoms in $Au_6H_n/((3-n)H)$-FAU, n = 1-3, reveal oxidation of the gold atoms as indicated by the increasing values of the charges on going from the bare to the hydrogenated cluster with a maximum value in Au_6H_3/FAU. This clearly shows

oxidation of both the Au_z and Au_t atoms upon stepwise hydrogen spillover. Our calculations on zeolite supported Au_6 cluster are in agreement with those reported by Vayssilov *et al.*[20] Such an analysis for hydrogen atoms gives an HPA value of 0.098 e in $Au_6/3H$-FAU whereas that in Au_6H_3/FAU complex is –0.044e indicating a formal reduction of H^+ to H^- during reverse hydrogen spillover process. MPA values also support this trend as seen in Table 6.2. The HPA charges of acidic hydrogen of zeolite (H_Z) in $Au_6H/(2H)$-FAU and $Au_6H_2/(1H)$-FAU clusters are 0.123e and 0.138e (MPA values: 0.337, 0.343), respectively whereas that of spilled over hydrogen (H_{Au}) are -0.055e and -0.051e (MPA values: 0.116, 0.126), respectively. Thus, both MPA and HPA values for all the clusters are supportive of the fact that reverse hydrogen spillover from the zeolite to gold cluster leads to reduction of hydrogen atoms.

Finally, we present the reverse spillover energy, E_{RS}, for migration of acidic hydrogen atoms of the zeolite cluster to Au_6 cluster. It is seen from Table 6.2 that the E_{RS} for the first proton is –67.6 kJ/mol. The E_{RS} per atom for transfer of two and three protons from the zeolite cluster are –65.6 and –59.1 kJ/mol, respectively. Our reported reverse hydrogen spillover energy of –59.1 kJ/mol for the Au_6H_3/FAU system is very close to the value (-47.0 kJ/mol) estimated by Shor *et al.*[15] using a hybrid QM/MM approach. Moreover, we have modelled the sequential migration of 1, 2 and 3 protons from the bridging OH groups of faujasite zeolite without any symmetry constraint. Vayssilov and Rösch[14] calculated reverse hydrogen spillover energy for Au_6 supported on zeolites and obtained a value of –18.0 kJ/mol per transfer of hydrogen. This may be due to different position of acidic hydrogen atoms in the cluster model chosen by them.

6.4 Conclusions

We have systematically modeled the sequential migration of protons from the bridging OH groups of faujasite zeolite to the Au monomer in the oxidation states 0 and +1 and to the triangular Au_6 cluster without any symmetry constraint. We have found that the migration of one and two protons are possible in the case of Au^0 atom, while in the case of Au^+, migration of only one proton is possible. For the Au_6 cluster migration of all three hydrogen atoms from bridging OH groups of the zeolite onto the gold cluster are possible. In case of Au^0, the hydrogenated atom is

more stable than the dehydrogenated one, while in the case of Au^+, the dehydrogenated monomer is more stable.

For zeolite supported Au_6 cluster it is found that the hydrogenated clusters are energetically favourable over the bare supported cluster. The calculated Au–O distances for the model clusters are in very good agreement with the available experimental results. We found a decrease in Au–O distances in the hydrogenated Au_6 clusters as compared to the bare supported cluster, approaching a value of ~ 2.08 Å for Au_6H_3/FAU complex which is exactly the same as EXAFS data reported for Au supported on faujasite zeolite. The reverse hydrogen spillover energies for migration of 1, 2 and 3 acidic hydrogen atoms from the zeolite cluster on to the Au_6 cluster are –67.6, -65.6 and –59.1 kJ/mol, respectively. Reverse hydrogen spillover leads to oxidation of the gold atoms and simultaneous reduction of hydrogen atoms. The two types of gold atoms Au_z and Au_t, both in bare and protonated supported Au_6 clusters are seen to carry different charges. This indicates the existence of metal centers with different oxidation states within the same cluster.

References

[1] Häkkinen, H.; Landman, U. Gold clusters Au_n ($2 \leq n \leq 10$) and their anions. *Phys. Rev. B*, **62**, R2287-R2290 (2000).

[2] Walker, A. V. Structure and energetics of small gold nanoclusters and their positive ions. *J. Chem. Phys.*, **122**, 094310-094321 (2005).

[3] Zhao, J.; Yang, J.; Hou, J. G. Theoretical study of small two-dimensional gold clusters. *Phys. Rev. B*, **67**, 085404-085409 (2003).

[4] Sankaran, M.; Viswanathan, B. A DFT study of the electronic property of gold nanoclusters (Au_x, x= 1-12 atoms). *Bull. Catal. Soc. India*, **5**, 26-32 (2006).

[5] Jain, P. K. A DFT-based study of the low-energy electronic structures and properties of small gold clusters. *Struct. Chem.* **16**, 421-426 (2005).

[6] Salama, T.M.; Shido, T.; Ohnishi, R.; Ichikawa, M. Low-temperature catalytic decomposition of NO over excess-loading gold(I) in NaY zeolite. *J. Chem. Soc., Chem. Commun.* 2749-2750 (1994).

[7] Yoon, B. *et al.* Charging effects on bonding and catalyzed oxidation of CO on Au_8 clusters on MgO. *Science* **307**, 403-407 (2005).

[8] Häkkinen, H.; Abbet, S.; Sanchez, A. ; Heiz, U.; Landman, U. Structural, electronic and impurity-doping effects in nanoscale chemistry: supported gold nanoclusters. *Angew. Chem. Int. Ed.* **42**, 1297-1300 (2003).

[9] Fierro-Gonzalez, J. C.; Hao, Y.; Gates, B. C. Gold nanoclusters entrapped in the a-cages of Y zeolite: structural characterization by x-ray absorption spectroscopy. *J. Phys. Chem. C* **111**, 6645-6651 (2007).

[10] Guzman, J.; Gates, B. C. Catalysis by supported gold: correlation between catalytic activity for CO oxidation and oxidation states of gold. *J. Am. Chem. Soc.* **126**, 2672-2673 (2004).

[11] Vayssilov, G.N.; Rösch, N. Reverse hydrogen spillover in supported sub-nanosize clusters of the metals of groups 8 to 11. A computational model study. *Phys. Chem. Chem. Phys.* **7**, 4019-4026 (2005).

[12] Shor, E. A. I. ; Nasluzov, V. A.; Shor, A. M. ; Vayssilov, G. N.; Rösch, N. Reverse hydrogen spillover onto zeolite-supported metal clusters: an embedded cluster density functional study of models M_6 (M = Rd, Ir, or Au) *J. Phys. Chem. C,* **111**, 12340-12351 (2007).

[13] Bromley, S.T.; Sankar, G.; Catlow, C. R. A.; Thomas, J. M.; Maschmeyer, T. Bimetallic clusters supported on mesoporous silica: the effects of support interaction on cluster morphology. *Micro. Meso. Mater.* **44-45**, 395-399 (2001).

[14] Vayssilov, G. N.; Rösch, N. Free and hexa-rhodium clusters with light impurity atoms. *J. Phys. Chem. B*, **108**, 180-192 (2004).

[15] Shor, E. A. I.; Nasluzov, V. A.; Shor, A. M.; G.N. Vayssilov and N. Rösch, Reverse hydrogen spillover onto zeolite-supported metal clusters: An embedded cluster density functional study of models M_6 (M = Rh, Ir, or Au) *J. Phys. Chem. C*, **111** 12340-12351 (2007).

[16] Li, F. *et al.* Zeolite-encaged iridium clusters with hydride ligands: characterization by extended x-ray absorption fine structure, NMR and inelastic neutron scattering vibrational spectroscopies. *Zeitschrift für Physikalische Chemie*, **220**, 1553-1568 (2006).

[17] Inntam, C.; Moskaleva, L. V.; Yudanov, I. V.; Neyman, K. M.; Rösch, N. Adsorption of Cu_4, Ag_4 and Au_4 particles on the regular MgO(001) surface: a density functional study using embedded cluster models. *Chem. Phys. Lett.*, **417**, 515-520 (2006).

[18] Neyman, K. M.; Inntam, C.; Moskaleva, L. V.; Rösch, N. Density functional embedded cluster study of Cu_4, Ag_4 and Au_4 species interacting with oxygen vacancies on the MgO(001) surface. *Chem. Eur. J.*, **13**, 277-286 (2006).

[19] Weiher, N. *et al.* Structure and oxidation state of gold on different supports under various CO oxidation conditions. *J. Catal.* **240**, 100-107 (2006).

[20] Vayssilov, G. N.; Gates, B. C.; Rösch, N. Oxidation of supported rhodium clusters by support hydroxyl groups. *Angew. Chem. Int. Ed.* **42**, 1391- 1394 (2003).

CHAPTER 7

TDDFT Optical Absorption Spectra of Coinage Metal Dimers Supported on MgO(001)

In this chapter we investigate the optical spectra of coinage metal dimers adsorbed on three types of sites on the MgO(001) surface: regular O^{2-} site and oxygen vacancies F_s and F_s^+. This chapter is the result of a collaborative work carried out at Prof. Notker Rösch's group, Technische Universität München, Germany, which has been reported in Reference 19. That work[19] describes the development of the combined Natural Transition Orbital (NTO)-Fragment Molecular Orbital (FMO) method and its implementation into the TDDFT module of the parallel density functional code PARAGAUSS as well as the evaluation of this novel analysis tool by applying it to coinage metal dimers adsorbed on the MgO(001) surface. M. Huix-Rotllant and A. V. Matveev, under guidance of N. Rösch, augmented the TDDFT module of PARAGAUSS, originally developed by Bosko et al.[11] My contribution to this collaborative work was the evaluation of this new methodology by applying it to a system that was already well studied,[11] but not sufficiently understood. The new approach leads to a more quantitative and hence improved description of optical transitions. Each spectral transition is identified in terms of electron-hole excitations characterized by pairs of occupied and unoccupied NTOs. For each of these NTOs the dominant contributing Kohn Sham orbitals are determined which are then subjected to a Fragment Molecular Orbital analysis taking the cluster and the support as fragments. Specific spectral features are found for adsorbed Ag_2 compared to Au_2 and Cu_2, which is attributed to the weaker adsorption of Ag_2 on the MgO(001) surface.

7.1 Introduction

Optical spectroscopy is an essential tool to determine and quantify chemical and physical properties of chemical systems. Recent advances in spectroscopic techniques for such multi-component systems as metal species on oxide support,[1-4] provide rich spectral data at high precision. In spite of this progress with experimental techniques, less attention has been paid to interpreting such spectra in a quantitative way and the assignment of the bands remained a tedious task. With the development of quantum mechanical methods, it became possible to carry out spectroscopic studies theoretically, thus giving out valuable information which would aid in the understanding of the physical phenomenon underlying the experimental results.[5-7] Although these theoretical studies have gone a long way in simplifying the interpretation of spectra, spectroscopic studies of complex systems still remain an arduous task.

Linear response time-dependent density functional theory is one among the state-of-the-art techniques that allows the efficient calculation of vertical electronic transitions of large systems with sufficient accuracy.[8] This method represents each peak as superposition of particle-hole contributions. Excitations of simple systems often are characterized by one leading pair of orbitals, making the assignment straightforward. This method has been applied to study the optical absorption spectra of systems like metal clusters protected by ligands,[9,10] Cu or Au atoms and small aggregates supported on MgO,[20,22] atomic and dimer gold species on SiO_2 and coinage metal dimers supported on MgO(001) surface.[11] Theoretical predictions based on TDDFT are found to have good agreement with experimental values. For larger systems simple interpretations are not valid as many particle-hole pairs with orbitals localized in different parts of the complex system contribute towards a particular transition with comparable amplitudes. An assignment of such spectral bands is not only tedious,[11] but a simplistic approach may also be misleading.

In order to simplify the interpretation of such complex spectra Martin developed an approach[12] whereby the leading contributions to a particular transition can be identified. This method relies on a linear transformation of the ground-state orbitals (leaving invariant each of the subspaces of occupied and virtual orbitals) to form a set of orbital pairs which affords a simpler description of the first-order transition density matrix. Transitions are no longer described as superposition of

pairs of Kohn-Sham (KS) orbitals, but by a smaller number of NTO pairs to which new weights are assigned. The recent popularity of the NTO analysis testifies to the usefulness of this technique, e.g. for characterizing reaction sites of organic chromophores and optical-active metal complexes.[13-15] Efficient algorithms are available to restrict the invariant subspaces for linear combinations even further if the systems exhibit spatial symmetry.[16,17]

For complex systems, neither KS orbitals nor NTOs are sufficiently localized in general to allow a simple characterization of the charge rearrangement associated with an excitation. For this purpose, a Fragment Molecular Orbital (FMO) analysis is required as an additional tool. This method divides the complex system into some parts, called fragments. Having identified the leading NTOs for a particular transition, it is possible to characterize these NTOs in terms of fragments of the system. This approach enables a more detailed description of optical transitions. For example, charge-transfer (CT) excitations between two fragments of a compound system can be easily identified in this way. The FMO approach has been implemented in combination with the NTO analysis in the parallel density functional (DF) program package PARAGAUSS[18] by Rösch and coworkers.[19]

In the present work the benefit of this combined NTO-FMO analysis is demonstrated by applying it to dimers M_2 of coinage metals (M = Cu, Ag, Au) adsorbed at regular oxygen sites as well as on oxygen vacancies F_s and F_s^+ of the MgO(001) surface. Due to their technological importance, numerous computational studies on adsorption and spectral properties have been carried out on these systems.[20-28] A study analogous to the present work has already been carried out by Rösch and coworkers[11] in which the optical absorption spectra of coinage metal dimers supported on MgO(001) has been explored. The attempt here is to put such analysis on a more quantitative footing by making use of the combined NTO-FMO analysis.

7.2 Computational Details

At first we briefly review the formulation of the NTO analysis in a basis set of symmetry-adapted ground-state orbitals in the framework of linear response TDDFT.[17] Then, we describe the FMO analysis. All calculations have been performed by using the program PARAGAUSS developed by Rösch and his group.[18]

7.2.1 Symmetry-Adapted Natural Transition Orbitals

Linear response TDDFT is an approximation where only pair products of occupied and virtual ground-state Kohn-Sham (KS) orbitals contribute to the density response $\delta\rho(\vec{r},\omega)$

$$\delta\rho(\vec{r},\omega) \approx \rho^{(1)}(\vec{r},\omega) = \sum_a^{occ} \sum_s^{unocc} T_{as}(\omega)\varphi_a(\vec{r})\chi_s(\vec{r}) \tag{7.1}$$

Here $\varphi_a(\vec{r})$ and $\chi_s(\vec{r})$ designate occupied and unoccupied ground-state KS orbitals, respectively. The labels a and s shall be used throughout the text to refer to occupied and unoccupied KS orbitals. $T_{as}(\omega)$ is the transition density matrix (TDM), a rectangular matrix representation of the response of the density in the KS basis set. It contains probability amplitudes of particle-hole excitations, each corresponding to a pair of orbitals. The frequencies ω of the external perturbation refer to a discrete spectrum of resonance frequencies, interpreted in TDDFT as electronic excitation energies.

When symmetry-adapted KS orbitals are used, a block structure of the TDM emerges. The symmetrized MOs have been labeled as $\left\{\varphi_a^{\Gamma_a\gamma_a}(\vec{r})\right\}$ and $\left\{\chi_s^{\Gamma_s\gamma_s}(\vec{r})\right\}$, respectively. The labels Γ_a, Γ_s represent irreducible representations (irreps) of a particular point-group; the indices γ_a, γ_s enumerate multiple occurrences of possibly degenerate irreps Γ_a and Γ_s. The response of the density to a perturbation, characterized by row γ of irrep Γ, is described as linear combination of symmetrized orbital products $\rho_{as}^{(\Gamma_a\Gamma_s)\Gamma\gamma}$,

$$\delta\rho^{\Gamma\gamma}(\vec{r},\omega) \approx \sum_{(\Gamma_a\Gamma_s)\to\Gamma} T_{as}^{(\Gamma_a\Gamma_s)\Gamma}(\omega)\rho_{as}^{(\Gamma_a\Gamma_s)\Gamma\gamma}(\vec{r}), \tag{7.2}$$

which in turn are linear combinations of pair products:

$$\rho_{as}^{(\Gamma_a\Gamma_s)\Gamma\gamma}(\vec{r}) := \sum_{\gamma_a=1}^{\dim\Gamma_a} \sum_{\gamma_s=1}^{\dim\Gamma_s} C(\Gamma_a\gamma_a,\Gamma_s\gamma_s,\Gamma\gamma)\varphi_a^{\Gamma_a\gamma_a}(\vec{r})\chi_s^{\Gamma_s\gamma_s}(\vec{r}) \tag{7.3}$$

Here $C(\Gamma_a\gamma_a,\Gamma_s\gamma_s,\Gamma\gamma)$ are Clebsch-Gordan coefficients that originate from reducing the direct product $\Gamma_a \otimes \Gamma_s$. The rare case, where reduction of this direct product leads to multiple instances of the same irrep, is not conceptually different, but can be handled by delineating these instances of an irrep Γ by an independent index τ in the expressions above; this index has been omitted for clarity. Each block of the

transition density matrix, $T_{a_s}^{(\Gamma_a\Gamma_s)\Gamma}(\omega)$, in this representation carries a symmetry label Γ and may be subdivided into subblocks characterized by the parental symmetries of the initial and final states Γ_a and Γ_s, respectively. Index Γ is a "good" quantum number for linear response TDDFT solutions; it corresponds to the electronic term symmetry of traditional electronic structure theory. The corresponding equations for the resonance excitations of each symmetry are solved independently. Each solution is, in general, a superposition of particle-hole excitations from several channels $\Gamma_a \rightarrow \Gamma_s$, where each channel is described by a pair of initial and final state symmetries, Γ_a and Γ_s. A given point group symmetry restricts the channels that may contribute to terms of a specific symmetry Γ, whereas a channel may contribute to the terms of different symmetries Γ. The transition amplitudes $T_{a_s}^{(\Gamma_a\Gamma_s)\Gamma}(\omega)$ are not specific to row γ of irrep Γ: in case of degenerate irreps, multiple solutions of the density response $\delta\rho^{\Gamma\gamma}$, Eq. (7.2), that differ only by the row index γ are equivalent by symmetry. The corresponding resonances are induced by the same type of the periodic perturbation with different polarizations: in the particular case of a nearly axial symmetry of the systems under study we will distinguish between the polarization direction of the electric field normal to the surface plane and two in-plane polarization directions.

The amplitudes of the particle-hole contributions in a selected channel of some resonance term are collected in the $N_a \times N_s$ block $T_{a_s}^{(\Gamma_a\Gamma_s)\Gamma}(\omega)$ of the TDM; N_a and N_s are the dimensions of the occupied and virtual orbital subspaces of irreps Γ_a and Γ_s, respectively. A more concise description of a channel is achieved when electronic transitions are represented in terms of NTOs.[12] NTOs are linear combination of the original occupied or virtual Kohn-Sham orbitals that achieve a singular value decomposition of the corresponding block of the TDM. The coefficients of the linear transformations of the occupied and virtual subspaces from the KS picture have been organized to the NTO picture into square matrices $U^{(\Gamma_a\Gamma_s)\Gamma}$ and $V^{(\Gamma_a\Gamma_s)\Gamma}$:

$$\tilde{\varphi}_{a'}^{\Gamma_a\gamma_a} = \sum_a^{occ} U_{aa'}^{(\Gamma_a\Gamma_s)\Gamma} \varphi_a^{\Gamma_a\gamma_a}$$

$$(7.4a)$$

$$\tilde{\chi}_{\varsigma'}^{\Gamma,\gamma_s} = \sum_{\varsigma}^{unocc} V_{\varsigma'\varsigma}^{(\Gamma_a\Gamma_s)\Gamma*} \chi_{\varsigma}^{\Gamma,\gamma_s}$$

(7.4b)

Here $\tilde{\varphi}_a^{\Gamma_a\gamma_a}$ and $\tilde{\chi}_s^{\Gamma,\gamma_s}$ are occupied and virtual NTOs and one has:

$$t^{(\Gamma_a\Gamma_s)\Gamma}(\omega) = U^{(\Gamma_a\Gamma_s)\Gamma} T^{(\Gamma_a\Gamma_s)\Gamma}(\omega) V^{(\Gamma_a\Gamma_s)\Gamma\dagger}$$

(7.5)

where the (rectangular) so-called Natural Transition Density Matrix (NTDM) $t^{(\Gamma_a\Gamma_s)\Gamma}(\omega)$ has non-zero elements only along its main diagonal.

In the analysis of the spectral lines below, probabilities or weights w_t of the transitions (particle-hole excitations) is used according to

$$w_t = | t_{ll}^{(\Gamma_a\Gamma_s)\Gamma} |^2$$

(7.6)

For each excitation, the sum of these weights is adjusted so that they add up to one. The singular value decomposition, Eq. (7.5), is carried out with a standard library routine.[29]

Just as the original KS orbitals, Eqs. (7.4a, 7.4b), pairs of NTOs, one each from the occupied and the virtual subspaces, are also classified by an irrep Γ (and a row γ). Moreover, as NTOs are defined for specific channels of a given resonance, they carry implicitly the channel labels $(\Gamma_a\Gamma_s)\Gamma$ which have been omitted here for brevity. Thus, the basis of NTOs is optimized for the description of every channel of each resonance.

7.2.2 Fragment Orbital Analysis

MOs can be efficiently represented in a suitable finite (atomic) basis set:

$$\Psi_k(\vec{r}) = \sum_{j=1}^{N} \varphi_j(\vec{r}) c_{jk}$$

(7.7)

where the coefficients c_{jk} are determined in a KS ground-state calculation or come from an NTO analysis of a particular excitation channel. If the system is then broken into F fragments, and a ground state calculation is performed for each fragment f in the subset of the atomic basis functions $\varphi_j(\vec{r})$ that belong to it, the KS eigenfunctions of each fragment will be given by shorter linear combinations:

$$\psi_i^f(\vec{r}) = \sum_{j\in f}^{N_f} \varphi_j(\vec{r}) d_{ji}^f, \quad f = 1,\ldots,F.$$

(7.8)

Here N_f is the size of the basis set of fragment f; for the total number of basis

functions one has: $N = \sum_{f=1}^{F} N_f$. We also assume here that the geometry of the

separate fragments, and thus the location of the basis functions, is the same as in the

compound system. Then the joined set of MOs of all F fragments spans the same

space as the original basis, Eq. (7.7). We obtain the FMO representation of the KS

orbitals (or NTOs) as linear combination of this joined fragments basis set:

$$\Psi_k(\vec{r}) = \sum_{f=1}^{F} \sum_{i \in f}^{N_f} \psi_i^f(\vec{r}) g_{ik}^f \tag{7.9}$$

The expansion coefficients g_{ik}^f can be used to analyze the composition (and

localization) of the KS orbitals in terms of the chemically more appealing FMOs

instead of the computationally more convenient atomic basis set. The coefficients

g_{ik}^f are determined by solving the system of linear equations:

$$c_{jk} = \sum_{f=1}^{F} \sum_{i \in f}^{N_f} d_{ji}^f g_{ik}^f \tag{7.10}$$

Using the coefficients g_{ik}^f and accounting for the overlap of the fragment orbitals,

one can construct the fragment based population analysis.[30]

7.3 Results and Discussion

To demonstrate the efficiency of the procedure in identifying and

systematically quantifying electronic transitions, the NTO-FMO analysis is applied

to TDDFT results on coinage metal dimers M_2 (M = Cu, Ag, Au), adsorbed on ideal

O^{2-} sites as well as at neutral, F_s, and singly-charged oxygen vacancies, F_s^+, of the

MgO(001) surface. These spectra had previously been analyzed by Rösch and co-

workers in a qualitative fashion.[11] Here, a detailed quantitative description of the

physical processes involved in the main transitions of these adsorption systems is

provided.

The same model systems and structures as in the previous TDDFT study

mentioned earlier[11] has been used. The adsorption systems are modeled by a hybrid

QM/MM approach: a quantum mechanical (QM) subsystem is embedded at the

molecular mechanics (MM) level in an Elastic Polarizable Environment (EPE),[31]

that represents the confining and electrostatic effects of the MgO substrate. The

EPE method affords an accurate description of the relaxation of the support, induced by an impurity on the surface such as an oxygen vacancy and/or an adsorbed metal species. For adsorption at the ideal surface, the cluster $Mg_{10}O_{10}(Mg^{PP})_{12}$ has been used as QM partition of the model and the cluster $Mg_9O_8(Mg^{PP})_{12}$ for F_s and F_s^+ sites (Figure 7.1). The geometry of the adsorption complexes had been optimized assuming C_s symmetry.[23] The QM partition was described at the all-electron level using the linear combination of Gaussian-type orbitals fitting-functions density-functional (LCGTO-FF-DF) method[29] and the exchange-correlation functional as suggested by Becke and Perdew (BP86).[32] Further computational details and results on metal species adsorbed at MgO(001) are available in previous works by the group of Rösch.[25-28]

Cu, Au, Ag   Mg   O Mg^{PP*}
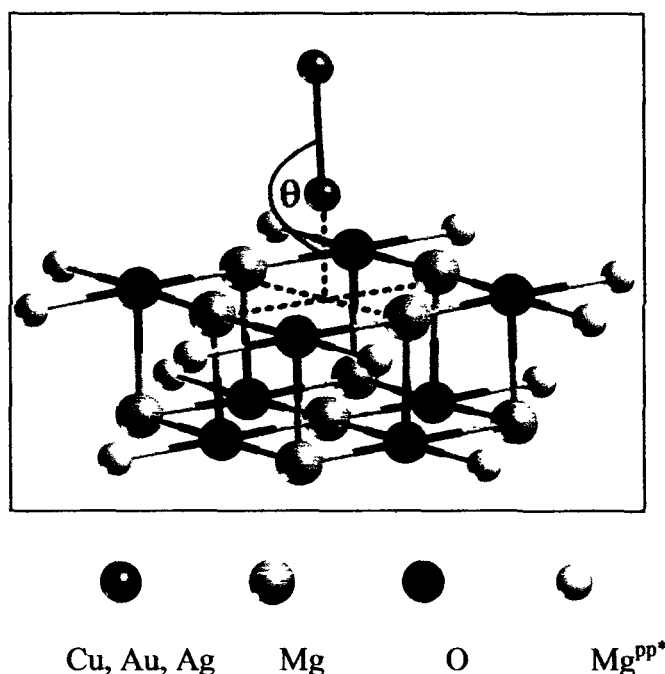
Figure 7.1. Example of the QM part of the embedded cluster model used for the calculations: optimized structure of M_2 (M = Cu, Ag, Au) adsorbed on an F_s^+ site modeled by a substrate of the form $Mg_9O_8(Mg^{PP})_{12}$. The preferred orientation of the dimer axis is almost upright, exhibiting approximate C_{4v} symmetry.

7.3.1. General Remarks

To describe the optical spectra of adsorbed M_2 systems, linear-response TDDFT approach has been applied to the optimized structures and oscillator strengths are calculated for the solutions, corresponding to the dipole allowed transitions.[12] Singlet-triplet transitions are not addressed in the present study,

although spin-orbit interaction may make them accessible in some experimental setups. With the BP exchange-correlation functional and the substrate model used, a band gap of ~4.6 eV is calculated for the MgO(001) surface, as estimated by the differences of KS eigenvalues. This underestimation of the experimental gap, ~7.8 eV,[33] is well known.[34] Therefore, we consider TDDFT solutions for resonances at energies larger than 4 eV as unreliable, as they may be subject to artificial admixtures of MgO valence states. Even at excitation energies below the band gap, transitions are found to comprise contributions both from the adsorbate and the support. To account for these limitations, the present analysis is restricted to transitions below 3.5 eV, but for completeness major spectral peaks are listed up to 4 eV. In Table 7.1 calculated spectra of M_2 (M = Cu, Ag, Au) in the gas phase and adsorbed at ideal O^{2-} sites of the MgO(001) surface are compared and analysed. In Tables 7.2 and 7.3 the NTO-FMO analysis for M_2 at F_s and F_s^+ sites of MgO(001), respectively are presented. Figures 7.2 to 7.4 present the corresponding information in graphical form to convey a qualitative impression of the spectra to be expected. For this purpose, the resulting line spectra, separately for each polarization component, are subject to a Gaussian broadening with $\sigma = 0.05$ eV which implies a full width of 0.12 eV at half-height.

In the tables, each spectral peak is characterized by major particle-hole contributions, represented by pairs of occupied and unoccupied NTOs. Only pairs with weight at least 0.30 are listed. In turn, for each of these NTOs dominant contributing KS eigenstates are listed. Finally, these characteristic KS eigenstates are subjected to an FMO analysis, taking as fragments the corresponding cluster and the support. The tables quantify only the dominant one of these two populations, the other one is determined via the normalization condition.

To illustrate the NTO-FMO analysis in detail, Peak IV of Cu_2 on F_s is considered as an example (Table II). This peak is calculated at an excitation energy of 2.88 eV, with oscillator strengths of 0.095 and 0.018 for light polarized perpendicular and parallel to the surface, respectively. The remaining information in the table characterizes the transition in detail. The weight $w_{NTO} = 0.59$ of the NTO pair under scrutiny implies that, according to Eq. (7.6), about 40 % of the NTO information of Peak IV is not taken into account in the analysis. Specific combinations of each NTO pair are described as linear combinations where initial

and final states are separated by an arrow (occupied – LHS, unoccupied – RHS). The coefficients U and V, Eq. (4a,b), quantify the linear combination of KS orbitals that form the initial and final state, respectively. Next, each KS orbital is characterized by its main FMO, together with the corresponding weight (in square brackets) and a label that indicates the orbital character. The final state is a linear combination of two main contributions: 81 % is due to a KS state that is mainly, 59 %, due to the defect, F_s, and 9 % are due to KS state whose main contribution, 42 %, is the $p\sigma_g$ level of Cu_2. As two NTO contributions each are listed for initial and final states of Peak IV, this implies four contributions to the transition in the KS picture: $0.92 \times 0.90 = 0.83$ ($d\sigma_u^* \rightarrow F_s$),$-0.28$($d\sigma_u^* \rightarrow p\sigma_g$),$0.35$ ($s\sigma_u^* \rightarrow F_s$),$0.12$ ($s\sigma_u^* \rightarrow p\sigma_g$). The squares of these emerging coefficients indicate the relative importance of the transition KS pair for the transition. Next, the assignments of the spectra of the various adsorption systems, at O^{2-}, F_s, and F_s^+ sites, obtained with the NTO-FMO analysis are compared and discussed.

7.3.2 Optical Transitions of M_2 at Regular Sites of MgO(001)

On the ideal MgO(001) surface, coinage metal dimers M_2 were calculated to adsorb in almost upright orientation on top of oxygen anions with M-O distances of 191.7, 224.2, and 213.6 pm for M = Cu, Ag, and Au, respectively.[26] The corresponding adsorption energies were calculated 132, 80, and 164 kJ mol^{-1}. In this energy range, the interaction of the metal species with the oxide support involves mainly polarization and Pauli repulsion.[35]

In a Kohn-Sham description, Ag_2 exhibits a large separation between the s and d valence shells (~1.5 eV), essentially without any hybridization.[11] The s and d valence manifolds of Cu_2 and Au_2 are energetically closer and undergo s-d hybridization.[36-40] Additional mixing occurs via spin-orbit interaction, especially in Au_2, which is neglected in the present treatment. These properties translate into analogous spectral features of the dimers in the gas phase (Figure 7.2), where Ag_2 differs notably from Cu_2 and Au_2. While Cu_2 and Au_2 exhibit two bands, a very weak Peak I of character $d\pi_g^* \rightarrow s\sigma_u^*$ at lower energies and a strong Peak II, $s\sigma_g \rightarrow s\sigma_u^*$, at higher energies (Table 7.1), Ag_2 shows only the latter peak of the σ-channel (Figure 7.2). Also the band intensities differ notably: the transition in the spectrum of Ag_2 in the gas phase is twice as intensive as the correspondent peaks of

Cu_2 and Au_2. An NTO analysis of the TDDFT results for dimers in the gas phase does not yield new insight because these transitions are represented by single particle-hole excitations. The HOMO-LUMO gap of Ag_2 remains almost unaffected by adsorption at regular O^{2-} sites of the ideal MgO(001) surface, but it is enlarged upon adsorption for the other two coinage metal dimers. These features are reflected in the spectra of the adsorbed species (Figure 7.2) which otherwise closely resemble those of the corresponding systems in the gas-phase, concomitant with the weak adsorbate-support interaction. The unaltered HOMO-LUMO gap of Ag_2 anticipates the almost vanishing shift of 0.07 eV, to higher energies of the peaks in the spectrum of Ag_2 at ideal sites (Table 7.1). For Cu_2 Peak I, assigned to the π-channel, shifts upward by 0.76 eV, whereas Peak II, assigned to the σ-channel, appears 1.06 eV higher than the corresponding peak in the gas phase (Table 7.1). Peak I of Au_2 is shifted by the same amount as for Cu_2, but the upward shift of Peak II of Au_2 is much smaller, only 0.24 eV (Table 7.1) because of the relativistic stabilization of the s-type valence levels of Au_2.

The interpretation of the optical spectrum of Ag_2 in the gas phase is relatively simple because in the energy range below 3.5 eV there appears only one peak, $s\sigma_g$ $\rightarrow$ $s\sigma_u^*$ (Table 7.1). In contrast to the other two coinage metal dimers, the excitations from the lower lying $d\pi_g^*$ level do not fall into the energy range under study. As a result of the weak interaction with the support, the optical spectrum of the supported dimer is hardly changed (Figure 7.2). Still, the FMO analysis shows ~20% admixture of the support in the initial state $s\sigma_g$, and significantly more for the final states $s\sigma_u^*$ (Peak II, 59%) and $p\pi_u$ (Peak III, 57%) (Table 7.1). The NTO weights w_{NTO} of the leading particle-hole excitations are at least 0.95, also in the adsorbed system. This permits one to characterize the peaks unambiguously by a single pair of initial and final states. The composition of the NTOs in this case is also simple: there is no admixture of $d\sigma$ levels to the initial state $s\sigma_g$. The large energy separation between the s and d molecular bands, preserved upon adsorption, allows one to rationalize this result.

Finally, there is the low-intensity Peak IIa at 3.86 eV in the spectrum of Ag_2 (Table 7.1, Ag_2/MgO) that previously was left unassigned.[11] According to the present NTO-FMO analysis, it represents a charge transfer (CT) excitation from the adsorbate to the substrate. This transition is considered as an artifact of the computa-
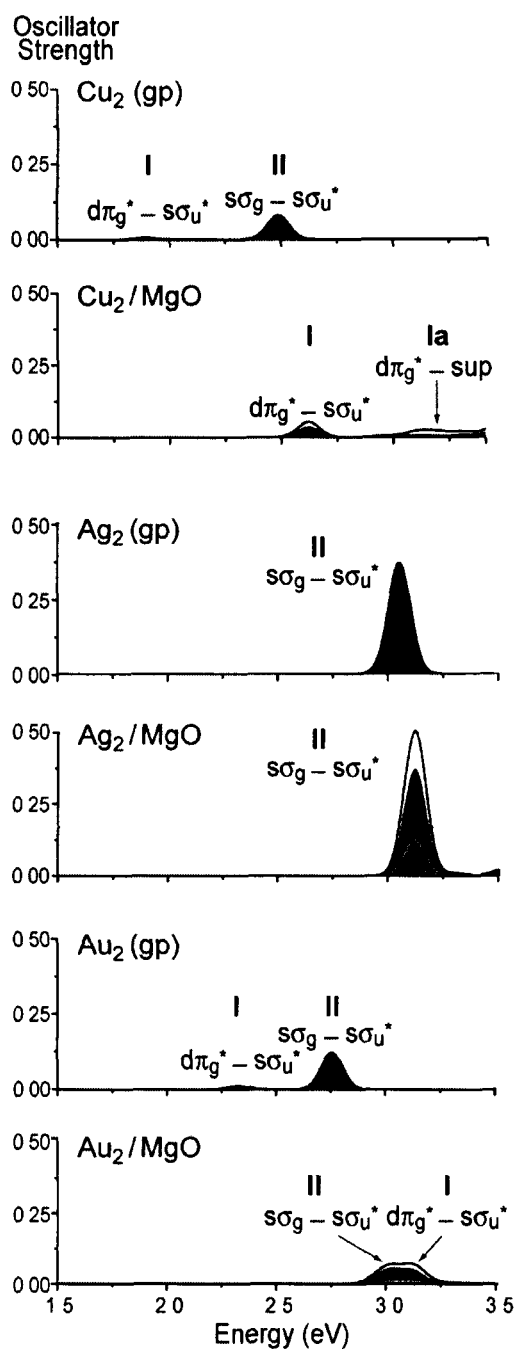
Figure 7.2. Optical spectra of coinage metals dimers Cu_2, Ag_2, and Au_2 in the gas phase (left-hand panels) and adsorbed at O^{2-} regular site of MgO (right-hand panels). Polarization components differentiated by shading: black – normal to the surface; gray – parallel to the surface. Details of the excitations corresponding to the labeled peaks, can be found in the text and Table 7.1.

tional methodology used that will not have a counterpart in that energy range of the experimental spectrum. TDDFT poorly represents CT transitions, mainly due to the lack of long-range interactions in popular exchange-correlation functionals.[41]

Table 7.1. Calculated optical spectrum of coinage metal dimers M_2 in the gas phase (gp) and adsorbed on regular surface oxygen sites of MgO(001) (O^{2-}).

M_2		Peak[a]	ΔE	$f_\perp$	$f_\parallel$	w_{NTO}[b]	U^c Char[d]	FMO[e]		V^c Char[d]	FMO[e]
Cu_2	gp	I	1.91	0.000	0.006	1.00	1.00 $d\pi_g^*$		→	1.00 $s\sigma_u^*$	
		II	2.53	0.080	0.000	0.99	0.91 $s\sigma_g$		→	1.00 $s\sigma_u^*$	
		IV	3.67	0.017	0.000	0.62	1.00 $d\pi_g^*$		→	1.00 $p\pi_u$	
						0.38	0.98 $d\sigma_g$		→	1.00 $s\sigma_u^*$	
	O^{2-}	I	2.67	0.036	0.016	0.98	0.94 $d\pi_g^*$	[1.00]	→	0.99 $s\sigma_u^*$	[0.88]
		Ia	3.16	0.000	0.007	0.95	1.00 $d\pi_g^*$	[1.00]	→	1.00 sup	[0.83]
			3.17	0.006	0.005	0.92	1.00 $d\pi_g^*$	[1.00]	→	1.00 sup	[0.62]
		II	3.59	0.064	0.042	0.78	0.62 $s\sigma_g$	[1.00]	→	1.00 $s\sigma_u^*$	[0.88]
						0.30	$d\sigma_g$	[0.93]			
		IVa	3.97	0.004	0.007	0.54	0.77 $d\pi_g^*$	[0.97]	→	1.00 sup	[0.92]
						0.30	1.00 $d\delta_u^*$	[1.00]	→	1.00 sup	
Ag_2	gp	II	3.05	0.367	0.000	1.00	1.00 $s\sigma_g$		→	1.00 $s\sigma_u^*$	
·	O^{2-}	II	3.12	0.372	0.130	0.98	1.00 $s\sigma_g$	[0.81]	→	1.00 $s\sigma_u^*$	[0.41]
		IIa	3.86	0.022	0.094	0.96	1.00 $s\sigma_g$	[0.81]	→	1.00 sup	[0.80]
		III	3.87	0.000	0.131	0.95	1.00 $s\sigma_g$	[0.81]	→	1.00 $p\pi_u$	[0.43]
Au_2	gp	I	2.35	0.000	0.012	1.00	1.00 $d\pi_g^*$		→	1.00 $s\sigma_u^*$	
		II	2.78	0.244	0.000	0.99	0.99 $s\sigma_g$		→	1.00 $s\sigma_u^*$	
	O^{2-} ·	II	3.02	0.041	0.011	0.99	1.00 $s\sigma_g$	[0.94]	→	1.00 $s\sigma_u^*$	[0.79]
		I	3.12	0.041	0.015	1.00	1.00 $d\pi_g^*$	[0.43]	→	1.00 $s\sigma_u^*$	[0.79]
			3.17	0.000	0.007	1.00	1.00 sup	[0.81]	→	1.00 $s\sigma_u^*$	[0.79]
		IIa	3.63	0.003	0.009	1.00	1.00 sup	[0.81]	→	1.00 $s\sigma_u^*$	[0.79]

Excitation energy ΔE (eV) of each peak and components of the oscillator strength perpendicular, $f_\perp$, and parallel, $f_\parallel$, to the surface, as well as characterization of the excitation: transition probability w_{NTO} of the natural transition particle-hole pairs, NTO expansion coefficients in terms of KS orbitals for the occupied (U) and unoccupied (V) state, corresponding fragment orbital populations (FMO), and assigned character (Char) of the KS orbitals.

[a] The labels of the peaks are chosen as in Ref. 11; Figure 7.2 should also be seen.

[b] Only electron-hole contributions with a weight of at least 0.30 are listed.

[c] Only coefficients of 0.30 and larger are listed.

[d] Assigned character of the KS orbitals in terms of M_2 orbitals. Label "sup" indicates a state that is dominated by the support.

[e] Dominant fragment orbital population of the KS orbital under scrutiny, based on an FMO analysis with M_2 and the support as partitions. For systems in the gas phase, an FMO analysis is not meaningful.

When Cu_2 adsorbs at the regular surface MgO(001), four active bands are predicted (Table 7.1, Figure 7.2). Peak I, at 1.91 eV in Cu_2 in the gas phase and assigned to $d\pi_g^* \rightarrow s\sigma_u^*$, is calculated at 2.67 eV for the MgO supported dimer (Table 7.1). This shift to a higher excitation energy likely is due to a larger Pauli repulsion in the final state. According to the NTO analysis, the leading particle-hole excitation has a weight very close to 1.00, resulting in a rather pure picture with very few side transitions. While the initial states are almost completely located on the metal cluster, final states have some appreciable support contribution in addition to the dominating cluster contribution; this can be seen from the FMO analysis data (Table 7.1). The small support contribution provides an undistorted picture of the KS orbitals, making their correlation with dimer orbitals straightforward.

Peak II of Cu_2 at the regular surface of MgO was calculated at 3.59 eV. The NTO analysis reveals that the initial state is best described as a combination of Cu_2 $s\sigma_g$ and $d\sigma_g$ with coefficients 0.62 and 0.30, respectively (Table 7.1). We should recall that (*i*) some *sd*-hybridization already occurs in the orbitals of the free dimer, and (*ii*) a minor change in orbital composition takes place upon adsorption. Obviously, compared to Ag, the small energy separation favors the hybridization of the *s* and *d* shells of Cu. The final state of Peak II can be unambiguously assigned to $s\sigma_u^*$, with an NTO coefficient of 1.0. The FMO analysis also shows a very small substrate admixture to this level.

The NTO-FMO analysis reveals Peak Ia of Cu_2 (Figure 7.2, Cu_2/MgO), previously left unassigned,[11] as CT artifact. Peak IVa of Cu_2/MgO, at 3.97 eV is left unassigned as it falls right at the edge of the validity interval of 4 eV. In the supported system, Peak IV of Cu_2 in the gas phase, a transition at ~3.7 eV involving σ and π channels (Table 7.1, Cu_2/gp), is masked by spurious excitations within the MgO support. Note that Peak IV of Cu_2 in the gas phase may mistakenly be correlated with Peak IVa of Cu_2/MgO; however, the NTO-FMO analysis reveals such a suggestion as erroneous (Table 7.1).

Although the adsorption interaction of Au_2 is the strongest among the three coinage metal dimers, the KS pictures of the cluster levels are still clear enough to be characterized. For all peaks of Au_2 below 4 eV, the NTO analysis shows that the spectrum comprises rather pure particle-hole excitations between largely unmodified KS eigenstates (Table 7.1). This is in contrast to the analogous Cu_2 systems (see above). All of the Au_2 systems low-energy excitations involve the same $s\sigma_u^*$ final

state, to which this dimer orbital contributes 79% (Table 7.1). The initial $s\sigma_g$ state of Peak II is almost a pure dimer orbital (94%), whereas the initial $d\pi_g{}^*$ state of Peak I exhibits substantial contribution from the support (57%). Thus, also the mixing between support and cluster states of $Au_2/MgO(001)$ differs from the situation found for $Cu_2/MgO(001)$.

The oscillator strengths, calculated for the various orientations of polarized radiation (Table 7.1), reflect the C_{4v} site symmetry of the adsorption complexes, which is essentially preserved although the geometry optimizations were carried out with much weaker (C_s) symmetry constraints.[11] The low-energy transitions in the σ channel have low intensities when the electric field is oriented parallel to the surface (Table 7.1). Both in the gas phase and for adsorbed species, intensities of Ag_2 systems are notably larger than for the other two coinage metal dimers (Figure 7.2). This trend is noticeable already in the spectra of free and adsorbed atoms.[11] From the gas phase to supported dimers, intensities decrease for Cu_2 and Au_2, while the intensity of the main peak of the Ag_2 spectrum slightly increases after adsorption (Figure 7.2). A possible rationalization may be derived from the different strengths of adsorption interaction with the MgO surface. As Cu_2 and Au_2 interact stronger with the support, their oscillator strength is distributed over several lines as a result of orbital mixing with the support states. In contrast, the weaker interacting Ag_2 preserves most of its gas phase electronic structure after adsorption.

7.3.3 Optical Transitions of M_2 at F_s Sites of MgO(001)

Coinage metal dimers M_2 were calculated to adsorb at neutral oxygen vacancy F_s in almost upright orientation, very slightly tilted with respect to the surface normal.[23] They approach the MgO surface up to 160–180 pm; that distance is 20–50 pm shorter than at the regular site O^{2-}; yet, dimers are very far from entering the defect cavity. The stronger bonding of the adsorbate at the defect site entails a weaker, hence longer M-M bond, by ~10 pm. Pauli repulsion between the adsorbate and the surface is smaller at a defect site because the oxygen core of the regular oxygen surface site is missing. The two relatively polarizable electrons located in the cavity permit a stronger interaction (1.6–2.7 times) than at a regular O^{2-} site. The calculated binding energy of dimers at F_s sites are 222, 244, and 382 kJ mol^{-1} for Cu_2, Ag_2 and Au_2, respectively.[23]

With label F_s we refer to the surface state with two electrons in the moderately bound cavity. This cavity state strongly interacts with the orbitals of an adsorbate M_2, primarily with $p\sigma_g$ and less with $s\sigma_u{}^*$, thus formally creating three states of mixed character (Figure 7.3).[23] Thus, naming the resulting states is partly a matter of convention. Labels that reflect the results of our analysis shall be used. Accordingly, the level lowest in energy shall be referred to as $s\sigma_u{}^*$, the two other combinations in increasing order of energy as $p\sigma_g$, and F_s (Figure 7.3).
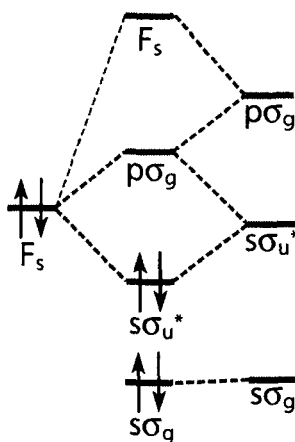
Figure 7.3. Molecular orbital energy diagram showing the interaction between the metal dimer M_2 and an oxygen vacancy site F_s at the surface of MgO(001).

The interaction of a dimer M_2 at a defect F_s is stronger than at a regular site O^{2-} because Pauli repulsion between adsorbate and support is weaker.[23] Therefore, unlike at regular sites, cluster levels undergo a larger mixing which renders a straightforward correlation with gas phase M_2 orbitals difficult (Figure 7.4). The NTO analysis reveals that either the F_s cavity state or another support level is involved in each excitation as leading or next important contribution (Table 7.2).

Both the NTO analysis and the FMO analysis reveal that for all three coinage metal dimers the initial states $s\sigma_u{}^*$ and $d\sigma_u{}^*$ are rather pure and hardly polarized (Table 7.2). The lower-energy part of the optical spectra of all three systems M_2/F_s, Peaks I to III, are dominated by excitations out of a state assigned as $s\sigma_u{}^*$ according to the FMO character; support levels contribute only a small amount. Also, NTO analysis reveals that $d\sigma$ levels hardly mix with the $s\sigma_u{}^*$ initial state as is sometimes the case in adsorption complexes at regular sites. Peaks IV, at 2.88 eV for Cu_2 and

Oscillator
Strength

Cu_2/F_s I   II   III   IV

0.50
0.25
0.00

$s\sigma_u^* - F_s$
$s\sigma_u^* - p\sigma_g$
$s\sigma_u^* - p\sigma_g$
$d\sigma_u^* - F_s$

Ag_2/F_s I   II   III

0.50
0.25
0.00

$s\sigma_u^* - p\sigma_g$ $s\sigma_u^* - F_s$ $s\sigma_u^* - p\sigma_g$

Au_2/F_s I   II   III

0.50
0.25
0.00

$s\sigma_u^* - p\sigma_g$ $s\sigma_u^* - p\sigma_g$
$s\sigma_u^* - F_s$

1.5   2.0   2.5   3.0   3.5

Energy (eV)
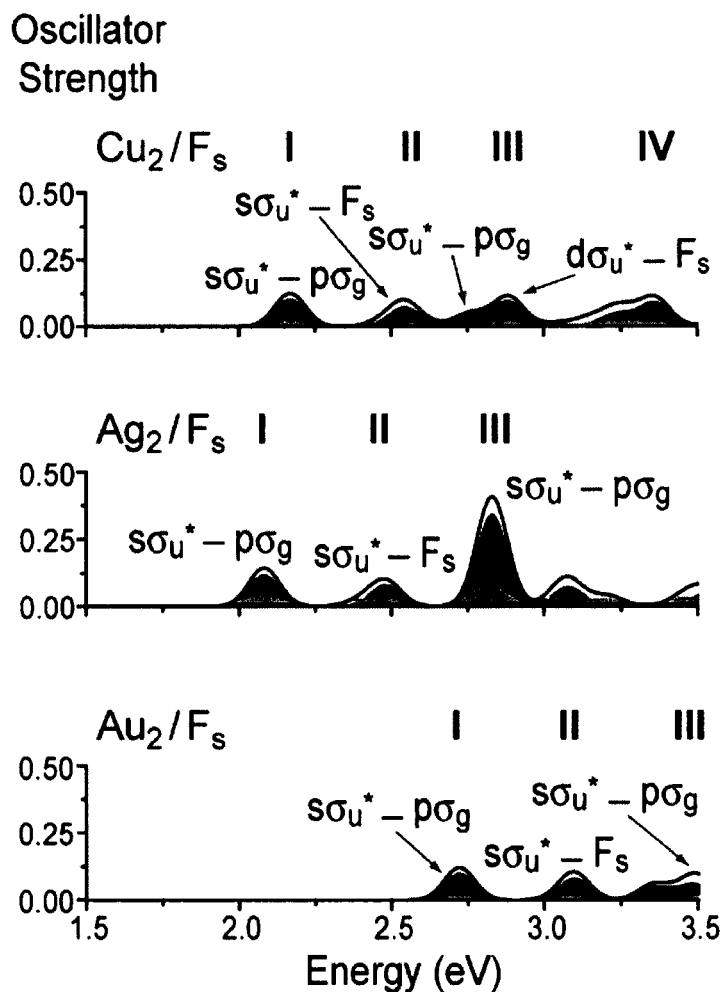
Figure 7.4. Optical spectra of coinage metals dimers Cu_2, Ag_2, and Au_2 adsorbed at an F_s site of MgO(001). Polarization components differentiated by shading: black – normal to the surface; gray – parallel to the surface. Details of the excitations corresponding to the labeled peaks can be found in the text and Table 7.2.

3.98 eV for Au_2 (Table 7.2), represents a transition out of the $d\sigma_u^*$ orbital of the dimer. As a result of the much stronger interaction between Au_2 and the support this band appears at higher energies for Au_2/F_s (Figure 7.4). In fact, inspection of Table 7.2 reveals that the initial NTO of Peak IV of adsorbed Cu_2 is actually a mixture of $d\sigma_u^*$ and $s\sigma_u^*$ orbitals of Cu_2 – in contrast to Au_2 where the initial state of Peak IV exhibits pure $d\sigma$ character. As on the regular surface, mixing of s- and d-shells is more pronounced in Cu_2 than in the other two metal dimers. For Ag_2 no significant d contributions were noted in the initial state of any excitation below 4 eV (Table 7.2).

Table 7.2. Calculated optical spectrum of coinage metal dimers M_2 (M = Cu, Ag, Au) adsorbed at a neutral oxygen vacancy F_s of MgO(001).

M_2	Peak	ΔE	$f_\perp$	$f_\parallel$	w_{NTO}	U	Char	FMO	→	V	Char	FMO
Cu₂	I	2.17	0.103	0.021	0.99	1.00	$s\sigma_u^*$	[0.96]	→	0.89	$p\sigma_g$	[0.42]
										-0.45	F_s	[0.79]
	II	2.54	0.068	0.014	0.91	1.00	$s\sigma_u^*$	[0.96]	→	0.69	F_s	[0.79]
										0.65	$p\sigma_g$	[0.59]
	III	2.76	0.041	0.007	0.69	1.00	$s\sigma_u^*$	[0.96]	→	0.84	$p\sigma_g$	[0.59]
										-0.47	F_s	[0.79]
	IV	2.88	0.095	0.018	0.59	0.92	$d\sigma_u^*$	[0.96]	→	0.90	F_s	[0.79]
						0.39	$s\sigma_u^*$	[0.96]		-0.30	$p\sigma_g$	[0.42]
Ag₂	I	2.08	0.119	0.023	1.00	1.00	$s\sigma_u^*$	[0.92]	→	0.83	sup	[0.74]
										0.55	$p\sigma_g$	[0.34]
	II	2.48	0.081	0.015	1.00	1.00	$s\sigma_u^*$	[0.92]	→	0.79	F_s	[0.79]
										-0.52	$p\sigma_g$	[0.34]
	III	2.82	0.343	0.065	0.98	1.00	$s\sigma_u^*$	[0.92]	→	0.56	$p\sigma_g$	[0.34]
										0.40	$p\sigma_g$	[1.00]
										0.57	F_s	[0.79]
										-0.37	sup	[0.74]
	V	3.74	0.017	0.083	0.84	0.99	$s\sigma_g$	[0.81]	→	0.85	$p\pi_u$	[0.69]
										0.51	sup	[1.00]
Au₂	I	2.71	0.102	0.020	0.99	1.00	$s\sigma_u^*$	[0.95]	→	0.89	$p\sigma_g$	[0.67]
										0.45	sup	[0.66]
	II	3.34	0.047	0.008	0.90	1.00	$s\sigma_u^*$	[0.95]	→	0.74	F_s	[0.72]
										0.48	$p\sigma_g$	[1.00]
	III	3.47	0.048	0.090	0.78	1.00	$s\sigma_u^*$	[0.95]	→	0.71	$p\sigma_g$	[1.00]
										-0.41	$p\pi_u$	[1.00]
										-0.36	F_s	[0.72]
	IV	3.98	0.104	0.020	0.40	1.00	$d\sigma_u^*$	[0.93]	→	0.82	F_s	[0.72]
										-0.50	sup	[0.66]

Lay-out as in Table 7.1.

As Peaks I to III originate from the same level, $s\sigma_u^*$, of M_2 at F_s for all three coinage metal dimers, it is no surprise that the optical spectra at low excitation energies are calculated to be similar (Figure 7.4). The NTO analysis of these transitions reveals that the $M_2\ p\sigma$ orbital dominates the final-state orbitals in various combinations with either the F_s cavity state or another support state. The list of

contributions to the final state of an NTO pair is sometimes rather lengthy; thus, these final-state NTOs may not be optimally represented in terms of KS eigenstates. Nevertheless, from the combined NTO-FMO analysis one deduces that each excitation ends up in a state with major contributions from two of the three spatial regions: dimer, defect cavity, and support close to the adsorption site.

Peaks I to III of Cu_2 and Ag_2 at F_s appear at lower energies than at O^{2-}, in fact at very similar transition energies, as Pauli repulsion at F_s is lower because an oxygen atom has been removed (Figure 7.4).[11,23,42] The lowest lying transitions of Au_2 appear at least 0.5 eV higher, as this dimer interacts stronger with the support, hence exhibits higher lying final-state orbitals. If relativistic effects were included in the model of Ag_2, the bands would be expected to shift to slightly higher transition energies.

The polarization-resolved spectra reflect the fact that local C_{4v} symmetry of the adsoption complex is hardly broken (Figure 7.1). All peaks show strong interactions with the electric field component normal to the surface, whereas a weak interaction is anticipated with the electric field component parallel to the surface. The intensities of the peaks are much larger than in the spectra of the congeners at regular sites (Figure 7.4). As in Section 7.3.1, Ag_2 features stronger peaks than the other coinage metal dimers. The strongest transitions with polarization parallel to the surface, Peak V of Ag_2 and Peak III of Au_2 (Table 7.2), are due to significant M_2 $p\pi_u$ admixtures to the final state. For Peak V of Ag_2, both the oscillator strength and the π–character of the final state are more pronounced than for Peak III of Au_2.

7.3.4 Optical Transitions of M_2 at F_s^+ Sites of MgO(001)

On F_s^+ sites of MgO(001), Cu_2 and Au_2 were calculated to be oriented essentially perpendicular to the surface, while the molecular axis of Ag_2 was found to be titled ~30 ° with respect to the surface normal.[23] As there is only one electron left in the cavity of the charged vacancy F_s^+, adsorption complexes of M_2 are less stabilized by (partial) transfer to the $s\sigma_u^*$ dimer orbital (Figure 7.3) than complexes M_2/F_s at neutral defects. Consequently, binding energies are notably smaller: 132, 128, and 232 kJ mol^{-1} for Cu_2, Ag_2 and Au_2, respectively. Consistently with the overall weaker interaction with the substrate, M-Mg distances are 4–6 pm larger at F_s^+ than at F_s sites and M-M bonds are 1–3 pm shorter.

The optical spectra predicted for coinage metal dimers at F_s^+ sites do not show the regularities of the previous two series (Figure 7.5). As the binding is significantly weaker for M_2 adsorbed at F_s^+, the dimer states are less polarized than in the analogous complexes at a neutral vacancy. The FMO results (Table 7.3) confirm this analysis: initial and final states of NTO pairs are either M_2 states with
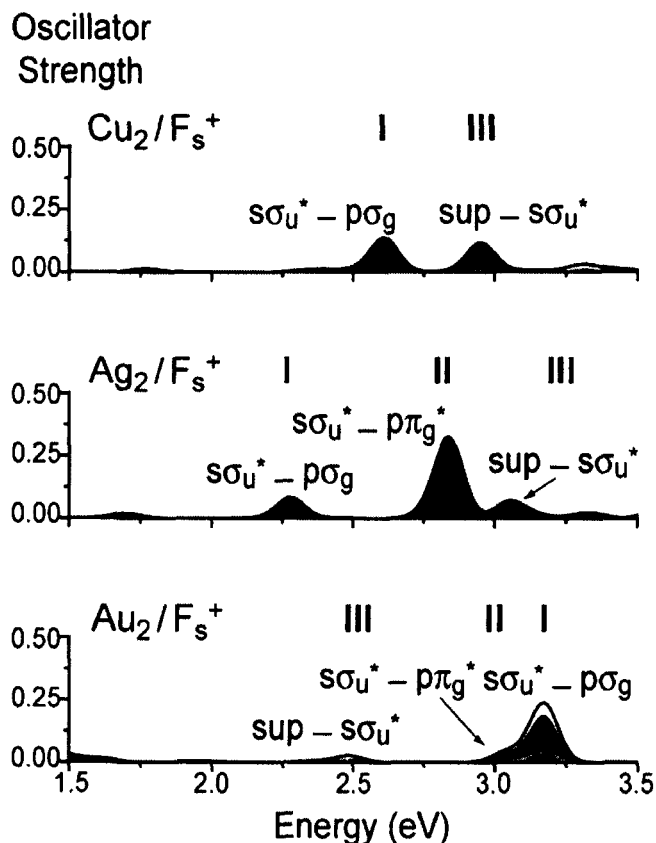
Figure 7.5. Optical spectra of coinage metals dimers Cu_2, Ag_2, and Au_2 adsorbed at an F_s^+ site of MgO(001). Polarization components differentiated by shading: black – normal to the surface; gray – parallel to the surface. Details of the excitations that correspond to the labeled peaks can be found in the text and Table 7.3.

support contributions of at most 28% or pure support states. This renders the orbital characterization notably simpler than in the complexes M_2/F_s. Also at variance with the latter complexes (Table 7.2), the F_s^+ cavity state is involved only in very few transitions, which, in addition, carry essentially no intensity. Peak I, common in all three spectra, appears at energies 2.61 eV, 2.28 eV and 3.26 eV for Cu_2, Ag_2, and Au_2, respectively (Figure 7.5). As for complexes at neutral defect sites, the stronger three-orbital interaction of Au_2 with the support level (Figure 7.3) results in a higher excitation energy. Peak I of Cu_2 involves only adsorbate states: $s\sigma_u^* \rightarrow p\sigma_g^*$ (Table

7.3). For Ag$_2$, the tilting of the dimer axis makes it possible that in addition $p\pi_g^*$ character is mixed into the final state (Table 7.3). This $p\pi_g^*$ state appears also as final state of Peak II, at 2.84 eV for Ag$_2$ and 3.11 eV for Au$_2$ (Table 7.3). Peak III, a support-to-adsorbate transition, is another common feature of all spectra of M$_2$/F$_s^+$ (Table 7.3).

Table 7.3. Calculated optical spectrum of coinage metal dimers M$_2$ (M = Cu, Ag, Au) adsorbed at a charged oxygen vacancy F$_s^+$ of MgO(001).

M$_2$	Peak	ΔE	$f_\perp$	$f_\parallel$	w_{NTO}	U	Char	FMO		V	Char	FMO
Cu$_2$	I	2.61	0.122	0.011	0.83	1.00	sσ_u^*	[0.85]	→	0.98	pσ_g	[1.00]
	III	2.95	0.108	0.008	0.82	0.97	sup	[1.00]	→	1.00	sσ_u^*	[0.85]
	III	3.31	0.000	0.012	0.87	1.00	sup	[1.00]	→	-1.00	sσ_u^*	[0.85]
Ag$_2$	I	2.28	0.083	0.001	0.79	1.00	sσ_u^*	[0.81]	→	0.93	pσ_g	[0.58]
										-0.37	pπ_g^*	[0.72]
	II	2.84	0.311	0.004	0.70	1.00	sσ_u^*	[0.81]	→	-0.94	pπ_g^*	[0.72]
	III	3.11	0.008	0.000	0.84	0.91	sup	[0.85]	→	1.00	sσ_u^*	[0.81]
						-0.32	sup	[0.92]				
	III	3.57	0.035	0.001	0.94	1.00	sup	[0.70]	→	1.00	sσ_u^*	[0.81]
Au$_2$	III	2.86	0.000	0.006	0.97	1.00	sup	[1.00]	→	1.00	sσ_u^*	[0.91]
	II	3.11	0.000	0.004	0.94	1.00	sσ_u^*	[0.91]	→	1.00	pπ_g^*	[1.00]
	I	3.26	0.209	0.042	0.96	0.99	sσ_u^*	[0.91]	→	0.98	pσ_g	[0.80]
	IV	3.87	0.020	0.004	0.95	1.00	sσ_u^*	[0.91]	→	0.98	sup	[0.77]

Lay-out as in Table 7.1.

The minor deviation from local C_{4v} symmetry for Ag$_2$ is also reflected in the distribution of the oscillator strength between the polarizations normal and parallel to the surface (Figure 7.5). Once again, the peak intensities for Ag$_2$ as adsorbate are notably higher than for the other two adsorbates, a trend observed also for free dimers.

7.4 Conclusions

The characterization of optical spectra of interacting systems, obtained with the TDDFT method, can be a tedious task; supported metal clusters are a case in point. A transparent rationalization of the compound system starts with the characterization of the separate partitions.

In this work, the advantages of a method that simplifies this task for optical spectra of interacting systems have been demonstrated. This NTO-FMO procedure combines advantages of two approaches, a Natural Transition Orbital (NTO) analysis and a Fragment Molecular Orbital (FMO) analysis. The NTO analysis identifies important particle-hole pairs, yielding a compact description of the spectral bands. The FMO analysis allows one to characterize the initial- or final-state NTOs in a transparent fashion in terms of Kohn-Sham orbitals of the interacting partitions.

The optical spectra of coinage metal dimers adsorbed on three types of sites on the MgO(001) surface: regular O^{2-} sites as well as neutral and charged oxygen vacancies, F_s and F_s^+ have been investigated with the help of this combined NTO-FMO approach. In this way, a previous analysis of these systems by the group of Rösch[11] has been confirmed and notably enhanced. Compared to that earlier study, the present quantitative results, collected in Tables 7.1, 7.2, and 7.3, convincingly demonstrate the wealth of pertinent information provided by a NTO-FMO procedure. Specific features of adsorption complexes of Ag_2 compared to those of Cu_2 and Au_2, have been identified and these differences have been related to the weaker adsorption interaction.

With the help of the NTO-FMO approach, the identification of dominant interactions in these systems: (*i*) weak electrostatic interaction compensated by Pauli repulsion for M_2 at regular site, (*ii*) strong orbital polarization by the cavity state upon interaction of M_2 with a neutral defect site, and (*iii*) moderately strong polarizations of M_2 in adsorption complexes at singly-charged defects F_s^+ has been possible. For complexes at F_s sites, the NTO analysis shows significant contributions of the cavity F_s state to the orbitals responsible for many peaks in the spectra, while the FMO procedure demonstrates that the metal cluster levels feature strong contributions of support levels. Adsorption complexes of M_2 at F_s^+ defects are shown to exhibit intermediate properties. Identification of charge transfer excitations from the adsorbate to the support has been possible. These have been classified as spurious.

References

[1] Peyser, L. A.; Vinson, A. E.; Bartko, A. P.; Dickson, R. M. Photoactivated flourescence from individual silver nanoclusters. *Science*, **291**, 103-106 (2001).

[2] Luo, M. F. *et al.* Growth and electronic properties of Au nanoclusters on thin-film Al_2O_3/NiAl(100) studied by scanning tunnelling microscopy and photoelectron spectroscopy with synchrotron radiation. *Surf. Sci.*, **602**, 241-248 (2008).

[3] Wahlström, E. *et al.* Bonding of gold nanoclusters to oxygen vacancies on rutile TiO_2 (110). *Phys. Rev. Lett.*, **90**, 026101-1-026101-4 (2003).

[4] Bell, A.T. The impact of nanoscience on heterogeneous catalysis. *Science*, **299**, 1688-1691 (2003).

[5] Pacchioni, G.; Giordano, L.; Baistrocchi, M. Charging of metal atoms on ultrathin MgO/Mo(100) films. *Phys. Rev. Lett.*, **94**, 226104-226107 (2005).

[6] Ricci, D.; Bongiorno, A.; Pacchioni, G.; Landman, U. Bonding trends and dimensionality crossover on metal-supported MgO thin films. *Phys. Rev. Lett.*, **97**, 036106-1 - 036106-4 (2006).

[7] Sterrer, M.; Risse, T.; Heyde, M.; Rust, H.P.; Freund, H.J. Crossover from three-dimensional to two-dimensional geometries of Au nanostructures on thin MgO (001) films: a confirmation of theoretical predictions. *Phys. Rev. Lett.*, **98**, 206103-206106 (2007).

[8] a) Runge, E.; Gross, E. K. U. Density-functional theory for time-dependent systems. *Phys. Rev. Lett.*, **52**, 997-1000 (1984). b) Casida, M. E. In *Recent Developments and Applications of Modern Density Functional Theory; Theoretical and Computational Chemistry Series*, Vol. 4, Elsevier: Amsterdam, p. 391–439 (1996). c) Marques, M. A. L. *et al. Time-Dependent Density Functional Theory*; Springer: Berlin, 2006.

[9] Nobusada, K. Electronic structure and photochemical properties of a monolayer-protected gold cluster. *J. Phys. Chem. B*, **108**, 11904-11908 (2004).

[10] Iwasa, T.; Nobusada, K. Theoretical investigation of optimized structures of thiolated gold clusters $[Au_{25}(SCH_3)_{18}]^+$ *J. Phys. Chem. C*, **111**, 45-49 (2007).

[11] Bosko, S. I.; Moskaleva, L. V.; Matveev, A. V.; Rösch, N. Optical spectra of Cu, Ag and Au monomers and dimers at regular sites and oxygen vacancies of the MgO(001) surface. A systematic time-dependent density functional study using embedded cluster models. *J. Phys. Chem. A*, **111**, 6870-6880 (2007).

[12] Martin, R. L. Natural transition orbitals. *J. Chem. Phys.*, **118**, 4775-4777 (2003).

[13] Dattelbaum, D. M.; Martin, R. L.; Schoonover, J. R.; Meyer, T. J. Molecular and electronic structure in the metal-to-ligand charge transfer excited states of fac-[Re(4,4'-X$_2$bpy)(CO)$_3$(4-Etpy)]$^{+*}$ (X=CH$_3$, H, Co$_2$Et). Application of density functional theory and time-resolved infrared spectroscopy. *J. Phys. Chem. A*, **108**, 3518-3526 (2004).

[14] Batista, E.; Martin, R. L. On the excited states involved in the luminescent probe [Ru(bpy)$_2$dppz]$^{2+}$. *J. Phys. Chem. A*, **109**, 3128-3133 (2005).

[15] Magyar, R. J.; Tretiak, S.; Gao, Y.; Wang H.-L.; Shreve A. P. A joint theoretical and experimental study of phenylene-acetylene molecular wires. *Chem. Phys. Lett.*, **401**, 149-156 (2005).

[16] Matveev, A. V.; Mayer, M; Rösch, N. Efficient symmetry treatment for the nonrelativistic and relativistic molecular Kohn-Sham problem. The symmetry module of the program Paragauss. *Comp. Phys. Comm.*, **160**, 91-119 (2004).

[17] Bosko, S. I. *Dissertation*; Technische Universität München: Munich, 2008.

[18] Belling, T., Grauschopf, T.; Krüger, S.; Nörtemann, F.; Staufer, M.; Mayer, M.; Nasluzov, V. A.; Birkenheuer, U.; Hu, A.; Matveev, A. V.; Shor, A. M.; Fuchs-Rohr, M. S.; Neymann, K. M.; Ganzushin, D. I.; Kerdcharoen, T.; Woiterski, A.; Gordienko, A. B.; Majumder, S.; Rösch, N. PARAGAUSS, version 3.1, Technische Universität München, Munich: 2004.

[19] Huix-Rotllant, M.; Deka, A.; Matveeev, A. V.; Bosko, S. I.; Moskaleva, L. V.; Rösch, N. Characterization of optical spectra of interacting systems: application to oxide supported metal clusters. *Int. J. Quantum Chem.*, **108**, 2978-2990 (2008).

[20] Vitto, A. D.; Sousa, C; Illas, F.; Pacchioni, G. Optical properties of Cu nanoclusters supported on MgO(100). *J. Chem. Phys.*, **121**, 7457-7466 (2004).

[21] Bonačić-Koutecký, V.; Bürgel, C.; Kronik, L.; Kuznetsov, A. E.; Mitrić, R. Optical properties of small silver clusters supported on MgO. *Eur. Phys. J. D*, **45**, 471-476 (2007).

[22] Walter, M.; Häkkinen, H. Optical absorption of magnesia-supported gold clusters and nanoscale catalysts: effects due to the supports, clusters and adsorbants. *Phys. Rev. B*, **72**, 205440 (2005).

[23] Matveev, A. V.; Neyman, K. M.; Yudanov, I. V.; Rösch, N. Adsorption of transition metal atoms on oxygen vacancies and regular sites of the MgO(001) surface. *Surf. Sci.*, **426**, 123-139 (1999).

[24] Neyman, K. M.; Inntam, C.; Nasluzov, V. A.; Kosarev, R.; Rösch, N. Adsorption of d- metal atoms on the regular MgO(001) surface: density functional study of cluster models embedded in an elastic polarizable environment. *Appl. Phys. A*, **78**, 823-828 (2004).

[25] Neyman, K. M.; Inntam, C.; Matveev, A. V.; Nasluzov, V. A.; Rösch, N. Single d-metal atoms on F_s and F_s^+ defects of MgO(001): a theoretical study across the periodic table. *J. Am. Chem. Soc.*, **127**, 11652-11660 (2005).

[26] Inntam, C.; Moskaleva, L. V.; Neyman, K. M.; Nasluzov, V. A.; Rösch, N. Adsorption of dimers and trimers of Cu, Ag and Au on regular sites and oxygen vacancies of the MgO(001) surface: a density functional study using embedded cluster models. *Appl. Phys. A*, **82**, 181-189 (2006).

[27] Inntam, C.; Moskaleva, L. V.; Yudanov, I. V.; Neyman, K. M.; Rösch, N. Adsorption of Cu_4, Ag_4 and Au_4 particles on the regular MgO(001) surface: a density functional study using embedded cluster models. *Chem. Phys. Lett.*, **417**, 515-520 (2006).

[28] Neyman, K. M.; Inntam, C.; Moskaleva, L. V.; Rösch, N. Density functional embedded cluster study of Cu_4, Ag_4 and Au_4 species interacting with oxygen vacancies on the MgO(001) surface. *Chem. Eur. J.*, **13**, 277-286 (2006).

[29] Anderson, E. *et al.* LAPACK User's Guide 3rd edition; SIAM: Philadelphia, 1999; Section 2.4.6.

[30] Staufer, M. Dissertation; Technische Universität München: Munich, 1999; Appendix A.

[31] a) Nasluzov, V. A. *et al.* Cluster embedding in an elastic polarizable environment: Density functional study of Pd atoms adsorbed at oxygen vacancies of MgO(001). *J. Chem. Phys.* **115**, 8157-8171 (2001); b) Nasluzov, V. A. *et al.* Density functional embedded cluster calculations on Lewis acid centres on the α-Al_2O_3 (0001) surface: adsorption of a CO probe. *Int. J. Quant. Chem.*, **90**, 386-402 (2002).

[32] a) Becke, A. D. Denisty-functional exchange-energy approximation with correct asymptotic behaviour, *Phys. Rev. A*, **38**, 3098-31000 (1988). b) Perdew, J. P.

Density-functional approximation for the correlation energy of the inhomogeneous electron gas. *Phys. Rev. B*, **33**, 8822-8824 (1986).

[33] Tjeng, L. H.; Vos, A. R.; Sawatzky, G. A. Electronic structure of MgO studied by angle-resolved ultraviolet photoelectron spectroscopy. *Surf. Sci.*, **235**, 269-279 (1990).

[34] Marques, M. A. L.; Gross, E. K. U. A Primer in: *Density Functional Theory*; Fiolhais, C.; Nogueira, F.; Marques, M. A. L., Eds.; *Lecture Notes in Physics*; Springer: Berlin, 2003, p. 144-184.

[35] Rösch, N.; Nasluzov, V. A.; Neyman, K. M.; Pacchioni, G.; Vayssilov, G. N.; in: *Computational Material Science*, Leszczynski, J., Ed.; *Theoretical and Computational Chemistry Series*, Vol. 15, Elsevier: Amsterdam, 2004, p. 367-450.

[36] Lochet, J. Laser-induced fluorescence of the Cu_2 molecule. *J. Phys. B*, **11**, L55-L57 (1978).

[37] McCaffrey, J. G.; Bennett, R. R.; Morse, M. D.; Breckenridge, W. H., Laser evidence for large electronic isotope shifts. *J. Chem. Phys.*, **91**, 92-103 (1989).

[38] Page, R. H.; Gudeman, C. S. Rotationally resolved dicopper (Cu_2) laser-induced fluorescence spectra. *J. Chem. Phys.*, **94**, 39-51 (1991).

[39] Ames, L. L.; Barrow, R. F. Rotational analysis of bands of the gaseous Au_2 molecule. *Trans. Faraday Soc.*, **63**, 39-44 (1967).

[40] Simard, B.; Hackett, P. A. High resolution study of the (0.0) and (1,1) bands of the $A^0_u{}^+$-$X^0_g{}^+$ system of Au_2 .*J. Mol. Spectros.*, **142**, 310-318 (1990).

[41] Magyar, R. J.; Tretiak, S. Dependence of spurious charge-transfer excited states on orbital exchange in TDDFT: large molecules and clusters. *J. Chem. Theor. Comput.*, **3**, 976-987 (2007).

[42] Pacchioni, G. Oxygen vacancy: the invisible agent on oxide surfaces. *Chem. Phys. Chem.*, **4**, 1041-1047 (2003).

CHAPTER 8

Conclusions and Future Scope

Conclusions

In this thesis we have explored the structures, electronic properties and reactivity of a large number of gold clusters Au_n in the size range n = 2-13, both in the neutral and singly charged cationic and anionic states and studied their interaction with metal-oxide supports. While there have been a number of studies in this field in the past, this work is unique in the sense that a large number of structures have been considered for detailed study. This was deemed necessary because of the ongoing controversy regarding the 2D-to-3D (two-dimensional to three-dimensional) crossover in case of gold nanoclusters. The highlight of our work is an unconstrained geometry optimization by the use of all-electron relativistic method, which is computationally expensive, but provides accurate results due to the fewer number of approximations involved. Fukui function based reactivity descriptors have been used to study the reactivity of charged species for the first time in this work. In addition, ours is the first theoretical exposition of the adsorption of a gold monomer on a faujasite zeolite support. Though the emphasis has been on the electronic and structural properties of the potentially catalytic systems rather than the actual reactions, a necessary first step towards catalysis has been taken by modelling CO and O_2 adsorption on $Au_6^{0,\pm}$ cluster in the gas phase and CO adsorption on the gold monomer in three oxidation states both in the gas phase and on a zeolite support.

Our work is based on density functional theory which is one of the most frequently used electronic structure methods. Most of the work has been performed by using the program package *DMol³*. For NBO analysis and adsorption studies on a large faujasite model by the hybrid Quantum Mechanics (QM)/Molecular

Mechanics (MM) method we have used the *GaussionO3* program, while the interpretation of optical spectra of coinage metal dimers adsorbed on the MgO(001) surface have been performed by using the program *ParaGauss*. At the beginning of the thesis we present a general introduction into the field of nanoparticles stressing on the uniqueness of gold and it applications in various fields including the burgeoning area of heterogeneous catalysis. An overview of computational methods used for modelling of nanoclusters, molecules, surfaces etc. is provided. These methods are broadly classified into those belonging to Molecular Mechanics and Quantum Mechanics. We have emphasized on the latter as our calculations mostly involve Quantum Mechanics. Density functional theory has been discussed in detail along with its time-dependent counterpart (TDDFT). The hybrid QM/MM method which has been used by us for the treatment of the large zeolite cluster having 60T sites has also been included within electronic structure methods.

Full geometry optimizations of Au_n clusters (n = 2-13) have been performed by using all electron scalar relativistic method without imposing any symmetry constraint. Different initial structures have been considered as candidates for geometry optimization. We have obtained optimized geometries for fifty eight neutral structures within the considered size range. Twelve of these are novel structures. All these structures have been confirmed to be minima on the potential energy surface by carrying out vibrational frequency calculations. Properties of each of these structures have been fully explored by calculating ionization potential, electron affinity, average bond length, binding energy, second difference of binding energy, HOMO-LUMO gap and chemical hardness. These properties were also calculated for the singly charged cationic and anionic counterparts. All minimum energy structures for cationic, neutral and anionic clusters have been found to be planar, i.e, no 2D-3D crossover could be identified within the considered size range for either neutral or charged clusters. The neutral Au_6 triangular structure has been found to be exceptionally stable.

DFT based local reactivity descriptors have been used to identify unique atoms in isomers of $Au_6^{0,\pm}$ clusters within an energy range of 1 eV from the minimum energy planar triangular structure. By using parameters like Fukui function for nucleophilic attack, Fukui function for electrophilic attack, relative nucleophilicity and relative electrophilicity, we have been able to predict the probabilities of electrophilic and nucleophilic attacks at different sites within these

clusters. Further, this study is extended to include all the minimum energy neutral $Au_n(n = 2\text{-}13)$ clusters. Based on this study it is predicted that the CO molecule prefers the apex site for adsorption on the triangular Au_6 cluster irrespective of the charge state of the cluster.

In order to verify the predictions for electrophilic and nucleophilic attacks obtained on the basis of DFT based local reactivity descriptors, we have adsorbed the CO and O_2 molecules on the minimum energy cationic, neutral and anionic triangular Au_6 clusters at various sites. It has been found that CO adsorbs at the apex and mid sites, with the adsorption at the apex site being stronger in agreement with our prediction. O_2 is found to be adsorbed at three sites, the apex site, the mid site and a bridge site, with the adsorption at the mid site being the strongest for neutral and cationic clusters in keeping with our prediction. For the anionic cluster adsorption energies at the apex and mid sites are comparable. The co-adsorption of CO and O_2 on these clusters has also been studied. Further, as catalytic activity of metal clusters depend on their charge states, we have investigated the adsorption of the CO molecule on a gold monomer in three charge states, 0, +1 and +3. This study has been performed in the gas phase and on a metal oxide support, namely, faujasite zeolite, by taking a small zeolite cluster having 9 tetrahedral sites and subjecting it to quantum mechanical treatment. In order to understand the role of the size of the support on adsorption properties, we have repeated our study of CO adsorption on the gold monomer by taking a large zeolite cluster with 60 tetrahedral sites and subjecting it to the hybrid QM/MM treatment implemented within the ONIOM method available in *Gaussian03*. The larger model of the support leads to a significant improvement in the CO binding energy in case of Au^+.

As zeolite supported transition metal clusters are believed to contain hydrogen as impurity atoms, we have investigated the process of revere hydrogen spillover from the bridging OH group of the zeolite support onto the monomers Au^0 and Au^+ and the Au_6 cluster. It is found that migration of one proton is possible in case of Au^+ while for Au^0 migration of one and two protons are possible. The reverse spillover energies are found to be exothermic in case of Au^0 and endothermic in case of Au^+. For the Au_6 cluster reverse spillover of one, two and three protons are found to be exothermic with the reverse spillover energy per transferred proton being highest in case of single proton transfer. Charge analysis reveals that gold

atoms get oxidized due to reverse hydrogen spillover, while the protons migrating from the support to the cluster get reduced.

Next we present the advantages of a methodology for interpreting the optical spectra of complex systems which uses the combined Natural Transition Orbital (NTO)-Fragment Molecular Orbital (FMO) approach by applying it to coinage metal dimers Au_2, Ag_2 and Cu_2 adsorbed on the MgO(001) surface. This adsorption study of coinage metal dimers is performed at three types of sites on the MgO(001) surface: regular O^{2-} site and oxygen vacancies F_s and F_s^+. These being complex systems, analysis of their optical spectra become a tedious task. We demonstrate that this analysis can be simplified by using the combined NTO-FMO approach. Each optical transition is identified in terms of electron-hole excitations characterized by occupied and unoccupied NTOs. For each NTO the Kohn-Sham orbitals having the leading contributions are subjected to a FMO analysis by considering the cluster and support as fragments. Our analysis reveals distinctive features of adsorption complexes of Ag_2 compared to those of Cu_2 and Au_2.

Future Scope

With continuing development in the fields of material science and nanotechnology, theoretical study of nanoclusters has emerged as an important area of research. For proper and complete understanding of a system of interest experimental observations need to be complemented by theoretical study. Detailed understanding of systems has been rendered possible in recent years by the tremendous development in computational resources. Among metal nanoparticles, gold plays centre stage due to innumerable applications in different fields. The importance of gold can be judged from the volume of current literature on the topic. It is hoped that the present study shall open up avenues for further research. We mention some of the emerging areas which may be investigated as a follow-up to the present work.

1) This study can be extended to investigate gold clusters of larger size and also gold surfaces.

2) Having determined the structure of stable gold nanoclusters, one can explore the possibility of application of these clusters for optical data storage, improved sensors and in medicine, for the treatment of cancer.

3) Structure and energetics of bimetallic clusters containing gold can be studied. This will lead to an understanding of the effect of the dopant on the properties of the cluster. Detailed study of doped clusters can be performed by varying the nature as well as the amount of the dopant.

4) CO adsorption studies can be carried out on other stable gold clusters, for example, Au_8, Au_4.

5) The oxidation reaction of CO to form CO_2 may be examined with gold clusters of different size and charge state both in the gas phase and on various metal oxide supports.

Ours has been a comprehensive study on gold clusters using density functional theory. We have explored various aspects like cluster size, isomeric structures, oxidation states, effect of different supports on the properties of gold clusters. The results show good agreement with experimental values. Having successfully investigated clusters of gold, a heavy element having 79 electrons, which requires the inclusion of relativistic effects for a proper description, we feel motivated to use the tremendously powerful DFT technique to carry out analogous studies on clusters of other transition metals, alkali metals, non metals, semiconductors etc. Such studies will enable comparison of clusters of different elements for specific applications. Also the effect of different ligands on cluster properties can be studied. The study can be extended to metal surfaces and heterogeneous clusters. It would be interesting to investigate magnetic properties of homogeneous and heterogeneous clusters and to study how these properties change on altering the cluster composition.

APPENDIX   A

Minimum energy structures of cationic and anionic Au_n clusters (n=2-13) and their Fukui functions
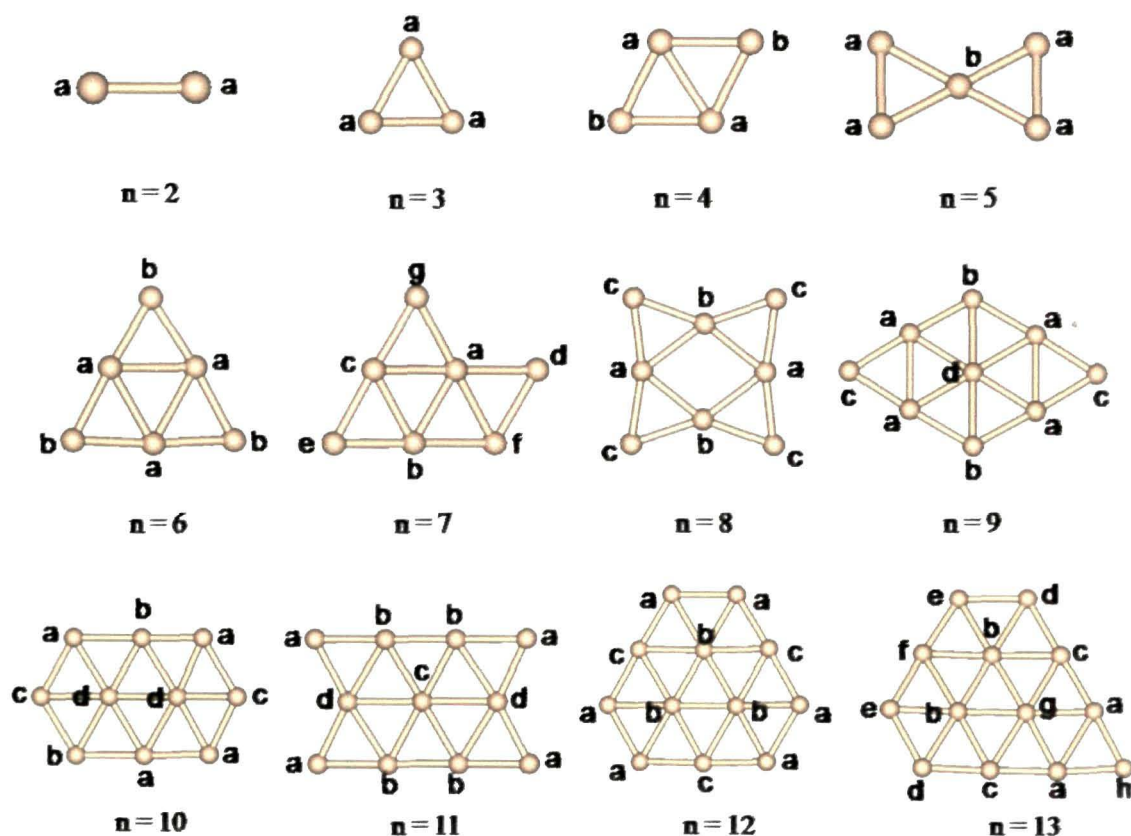

Figure A.1. Optimized geometries of minimum energy cationic Au_n clusters (n = 2-13) showing atom types.

Table A.1. Hirshfeld charges, Fukui functions, relative electrophilicity and relative nucleophilicity values for unique atoms of minimum energy cationic Au_n clusters (n = 2-13).

n	Structure	Atom type	Charges	f^+	f^-	f^+/f^-	f^-/f^+
2	Linear	a	0.50	0.50	0.50	1.00	1.00
3	Triangle	a	0.33	0.33	0.33	1.00	1.00
4	Rhombus	a	0.24	0.27	0.29	0.94	1.06
		b	0.26	0.23	0.21	1.08	0.93
5	X	a	0.23	0.23	0.23	1.03	0.97
		b	0.07	0.08	0.10	0.77	1.29
6	Triangle	a	0.14	0.12	0.14	0.91	1.10
		b	0.20	0.21	0.20	1.06	0.94
7	Capped triangle	a	0.17	0.15	0.15	1.01	0.99
		b	0.16	0.16	0.17	0.95	1.05
		c	0.11	0.10	0.10	0.98	1.02
		d	0.21	0.23	0.21	1.07	0.93
		e	0.19	0.19	0.19	1.02	0.98
		f	0.09	0.06	0.06	1.02	0.98
		g	0.07	0.11	0.13	0.90	1.12
8	Tetra edge capped rhombus	a	0.07	0.06	0.06	0.98	1.02
		b	0.10	0.08	0.08	1.00	1.00
		c	0.17	0.18	0.18	1.01	0.99
9	Bi edge-capped hexagon	a	0.08	0.09	0.09	0.99	1.01
		b	0.13	0.12	0.12	1.01	0.99
		c	0.16	0.17	0.17	1.01	0.99
		d	0.09	0.04	0.04	1.00	1.00
10	Tri capped hexagon	a	0.12	0.13	0.13	0.98	1.02
		b	0.08	0.08	0.08	1.11	0.90
		c	0.11	0.13	0.13	0.95	1.05
		d	0.08	0.04	0.03	1.12	0.89
11	Tetra capped hexagon	a	0.13	0.15	0.15	1.01	0.99
		b	0.07	0.07	0.07	1.00	1.00
		c	0.04	0.03	0.04	0.94	1.06
		d	0.07	0.05	0.05	1.00	1.00
12	Penta capped hexagon	a	0.10	0.12	0.12	1.01	0.99
		b	0.06	0.03	0.03	1.00	1.00
		c	0.07	0.07	0.07	0.96	1.04

Table A.1 continued

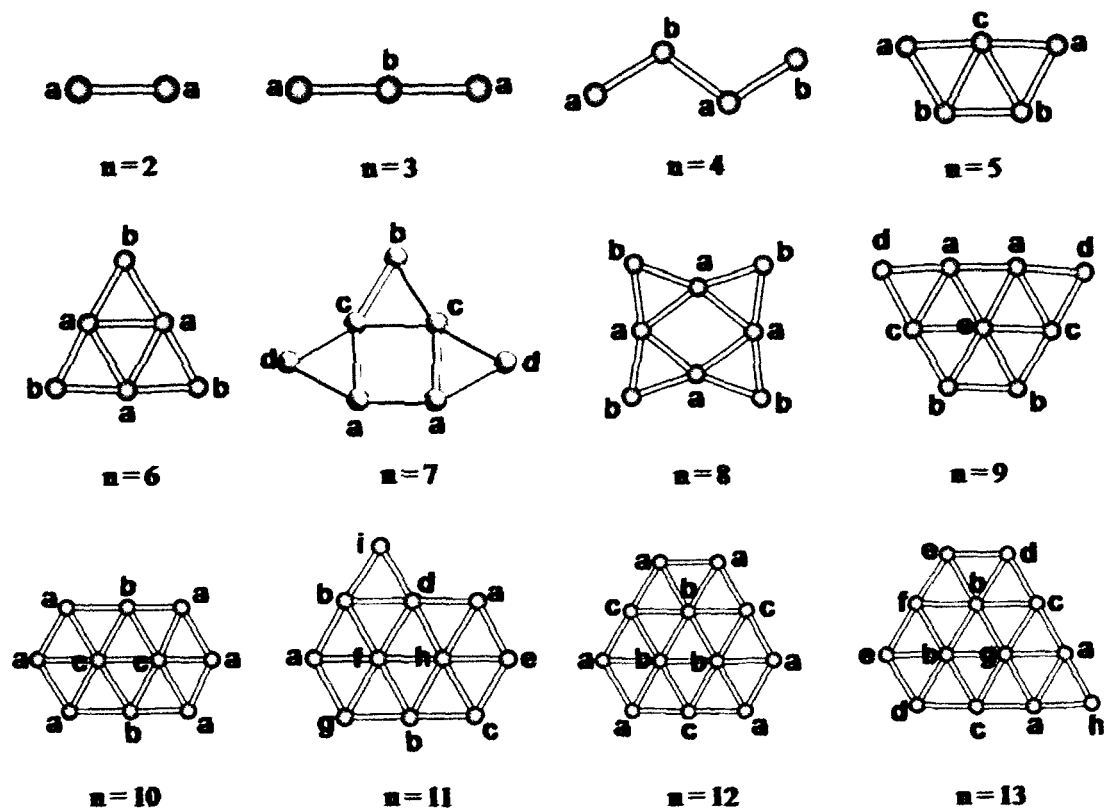| n	Structure	Atom type	Charges	f^+	f^-	f^+/f^-	f^-/f^+
13	Hexa capped hexagon	a	0.06	0.07	0.07	0.96	1.04
		b	0.07	0.03	0.03	1.07	0.93
		c	0.06	0.07	0.07	1.06	0.94
		d	0.09	0.10	0.11	0.94	1.06
		e	0.10	0.11	0.11	0.99	1.01
		f	0.06	0.08	0.08	1.01	0.99
		g	0.06	0.02	0.02	1.00	1.00
		h	0.14	0.15	0.14	1.05	0.95

Figure A.2. Optimized geometries of minimum energy anionic Au_n clusters (n = 2-13) showing atom types.

Table A.1. Hirshfeld charges, Fukui functions, relative electrophilicity and relative nucleophilicity values for unique atoms of minimum energy anionic Au$_n$ clusters (n = 2-13).

n	Structure	Atom type	Charges	f^+	f^-	f^+/f^-	f^-/f^+
2	Linear	a	-0.50	0.50	0.50	1.00	1.00
3	Linear	a	-0.39	0.38	0.37	1.03	0.97
		b	-0.22	0.24	0.26	0.92	1.09
4	Zigzag	a	-0.32	0.32	0.33	0.98	1.02
		b	-0.18	0.18	0.17	1.04	0.96
5	W	a	-0.24	0.25	0.24	1.06	0.94
		b	-0.20	0.16	0.19	0.86	1.16
		c	-0.11	0.17	0.14	1.15	0.87
6	Triangle	a	-0.10	0.11	0.12	0.88	1.13
		b	-0.23	0.23	0.21	1.06	0.94
7	Tri edge capped square	a	-0.13	0.12	0.13	0.98	1.02
		b	-0.14	0.25	0.19	1.32	0.76
		c	-0.06	0.08	0.08	1.08	0.93
		d	-0.24	0.17	0.20	0.83	1.21
8	Tetra Edge Capped Rhombus	a	-0.06	0.07	0.07	1.01	0.99
		b	-0.19	0.18	0.18	0.99	1.01
9	Bi edge-capped hexagon	a	-0.09	0.09	0.09	1.00	1.00
		b	-0.14	0.14	0.14	0.99	1.01
		c	-0.09	0.09	0.09	1.05	0.96
		d	-0.19	0.16	0.16	0.99	1.01
		e	0.01	0.05	0.05	0.96	1.04
10	Tri capped hexagon	a	-0.14	0.13	0.13	0.99	1.01
		b	-0.09	0.08	0.08	1.04	0.96
		c	0.00	0.04	0.04	1.03	0.98
11	Tetra capped hexagon	a	-0.11	0.12	0.11	1.06	0.94
		b	-0.07	0.08	0.08	1.05	0.95
		c	-0.12	0.11	0.10	1.05	0.95
		d	-0.04	0.04	0.04	1.00	1.00
		e	-0.12	0.13	0.12	1.08	0.93
		f	-0.01	0.04	0.04	0.92	1.09
		g	-0.17	0.12	0.14	0.89	1.13
		h	-0.18	0.14	0.15	0.91	1.09
		i	0.01	0.03	0.03	0.91	1.10
12	Penta capped hexagon	a	-0.13	0.11	0.11	1.00	1.00
		b	0.01	0.03	0.03	1.00	1.00
		c	-0.08	0.08	0.08	0.99	1.01

Table A.2 continued

n	Structure	Atom type	Charges	f^+	f^-	f^+/f^-	f^-/f^+
13	Hexa capped hexagon	a	-0.01	0.07	0.07	1.00	1.00
		b	0.04	0.03	0.03	1.03	0.97
		c	-0.01	0.07	0.07	1.00	1.00
		d	-0.01	0.10	0.10	0.99	1.01
		e	-0.01	0.11	0.11	1.01	0.99
		f	-0.01	0.07	0.07	0.99	1.01
		g	0.03	0.03	0.03	1.00	1.00
		h	-0.02	0.15	0.15	1.01	0.99

LIST OF PUBLICATIONS

In Journals

1) **A. Deka**, R. C. Deka and A. Choudhury, Preferential sites for adsorption of CO on Au$_6$ clusters using DFT based reactivity descriptors (communicated).

2) **A. Deka**, R. C. Deka and A. Choudhury, Adsorption of CO on gas phase and zeolite supported gold monomers: a computational study, *Chem. Phys. Lett.* **490**, 184-188 (2010).

3) R. C. Deka, **A. Deka** and A. Miyamoto, Density Functional Studies on the structure and reverse hydrogen spillover in Au$_6$ cluster supported on zeolite, *Catal. Lett.*, **131**, 155-159 (2009).

4) R. C. Deka, P. Mondal, **A. Deka** and A. Miyamoto, DFT based reactivity descriptors to predict the influence of alkali cations on the Brönsted acidity of zeolites, *Bull. Catal. Soc. Ind.*, **8**, 140-155 (2009).

5) **A. Deka** and R. C. Deka, Structural and Electronic Properties of Stable Au$_n$ (n=2-13) Clusters: A Density Functional Study, *J. Mol. Struct.*: THEOCHEM **870**, 83-93 (2008).

6) M. Huix-Rotllant, **A. Deka**, S. I. Bosko, A. V. Matveev, L. V. Moskaleva and N. Rösch, Characterization of Optical Spectra of Interacting Systems: Application to Oxide-Supported Metal Clusters, *Int. J. Quant. Chem.* **108**, 2978-2990 (2008).

7) P. Mondal, K. K. Hazarika, **A. Deka** and R. C. Deka, Density Functional Studies on Lewis Acidity of Alkaline Earth Metal Exchanged Faujasite Zeolite, *Mol. Simul.*, **34**, 1121-1128 (2008).

In Conferences

1) **A. Deka**, R. C. Deka and A. Choudhury, A computational study of CO and O_2 adsorption on cationic, neutral and anionic gold hexamer, 20th National Symposium on Catalysis, NCCR, IIT Madras, Chennai, December 19-22, 2010.

2) **A. Deka**, R. C. Deka and A. Choudhury, A computational study on CO adsorption on zeolite supported gold monomers by ONIOM method, *Recent Developments & Trends in Computational Chemistry*, NEHU, Shillong, March 12-13, 2010.

3) **A. Deka**, R. C. Deka and A. Choudhury, *Structure and Reverse Hydrogen Spillover in Mononuclear Au^0 and Au^I Complexes Bonded to Faujasite Zeolite – A Density Functional Study*, 14th National Workshop on Catalysis, Catalysis for Clean Environment and Sustainable Future, Tezpur University, December21-23, 2009.

4) **A. Deka**, R. C. Deka and A. Choudhury, A density functional study of carbon monoxide adsorption on zeolite supported gold monomers, *International Conference on Advanced Nanomaterials and Nanotechnology, ICAAN – 2009*, IIT Guwahati, December 9-11, 2009.

5) **A. Deka**, R. C. Deka and A. Choudhury, Density functional studies on the structure and reverse hydrogen spillover in zeolite supported gold nanoclusters, *Advances in Theoretical and Physical Chemistry*, University of Calicut, Calicut, Kerala, March 19-20, 2009.

6) **A. Deka**, A. K. Phukan and R. C. Deka, Structure and energetics of small gold nanoclusters: A density functional approach, *9th CRSI National Symposium in Chemistry, Department of Chemistry*, Delhi University, Delhi, February 1-4, 2007.